UNIVERSITÀ DEGLI STUDI DI MILANO

DIPARTIMENTO DI FISICA

CORSO DI DOTTORATO DI RICERCA IN
FISICA, ASTROFISICA E FISICA APPLICATA
CICLO XXVIII

Study of colloidal aggregation with static and dynamic Near Field Scattering techniques

Settore Scientifico disciplinare FIS/01

Tesi di Dottorato di:
Andrea Manca

Coordinatore: Prof. Francesco Ragusa
Supervisore: Dott. Marco A. C. Potenza

A.A. 2014-2015

Contents

Introduction

A colloidal system is composed of two insoluble substances, one dispersed (usually nano/micro sized particles) into the other. These could be gas, liquid or solid, generating different kind of suspensions. Examples are foams (liquid-gas), gels (solid-liquid), emulsions (liquid-liquid) and aerosols (gas-solid) where in bracket are reported the phases of the dispersion-dispersed medium. The stability or instability of these systems is guaranteed by the interaction between the dispersed particles. From now on, systems of solid particles dispersed in a liquid will be considered. In this kind of systems the main interactions between the particles responsible of the behavior of the suspension are the Van der Waals and the electrostatic interactions. If the system is out from equilibrium the particles start to attract and finally they will attach and form colloidal aggregates. These kind of processes may occur in two different limiting regimes: the first when the sticking probability is ~ 1, i.e. when two particles touch they stick together, while the second when the sticking probability lower then 1, i.e. the particles need to touch themselves different times before sticking. These two situations are named diffusion limited aggregation and reaction limited aggregation respectively. In the first the aggregation is so fast that the particles move only for diffusive motion and are not affected by other spurious motions that may occur in the solution, as it happens on the contrary in the second case. However in both these conditions fractal aggregates are formed and general scaling relations for the mass distribution can be found. Because of these scaling properties it is usual to speak about universality in fractal aggregation processes.

In the 1980s a lot of works were performed on these systems, both theoretically and experimentally. Recently an increasing interest in colloidal system arose again in the effort to study how the interactions may change the internal structure of the aggregates. All these works look in the direction of building colloidal aggregates, or colloidal crystals with controlled structures. The principal aim is to build devices with the bottom-up approach instead of traditional top-down, usually represented by lithography. However, changing the interaction strength is not trivial and at the same time other properties of the solution can change. In the last ten years a new way of performing aggregation in colloidal system has been observed: by critical Casimir effect in a solution out of equilibrium. This way of inducing aggregation was already studied but without considering it as critical Casimir effect. It was explained as a wetting transition of particles that because of surface properties stick [1, 2, 3].

Critical Casimir effect is a transposition to a classical system of the Casimir effect, which is typically a quantum effect. It explains how two plane metallic not-charged plane plates in vacuum may attract just for the confinement of vacuum state oscillation between them [4, 5]. The classical system that may exhibit a similar effect is a binary solution that presents a phase separation. Close to the condition of phase separation the order parameter, i.e. the density, shows some fluctuations that in the quantum transpo-

sition take the place of vacuum fluctuations. If in the mixtures a confinement is imposed to these fluctuations, the same situation of the Casimir effect is obtained [6]. This effect was observed at first as the interaction of a colloidal sphere with a wall [7] and subsequently it has been used to perform aggregation [8, 9]. The advantage of this effect is that the interaction strength depends on the fluctuations characteristic length, which is easily tunable by controlling the temperature of the solution. At the same time the interactions can be attractive or repulsive, depending on the boundary conditions imposed to the fluctuations [10]. The boundary conditions can be tuned by a surface treatment of the colloidal particles, for example by imposing hydrophilic or hydrophobic properties.

By the understanding of the interactions between colloidal particles it should be easier to understand the possibility of build structures in a controlled way.

Thesis overview

In the present thesis I show the results obtained with three different classes of experiments. The underlying topic is the colloidal aggregation studied with light scattering measurement. The thesis is divided in two parts: the first in which both theoretical and experimental bases of this work are explained (chapter 1 and 2) and the second part where three different experiments are shown (chapter 3, 4 and 5).

Chapter 1: Colloidal Interactions

Three different kinds of interactions of a colloidal suspension are shown that are relevant in the systems studied in the experiments. The Van der Waals interaction is the first considered. The second is the electrostatic interaction. Both these potentials are well known in literature [11] and are used to stabilize the colloidal suspensions. A perturbation of the equilibrium condition may lead to aggregation. The last interaction is the critical Casimir effect. It is a recently developed way to induce aggregation in a solution close to the phase transition.

Chapter 2: Near Field Scattering

In this section I explain the basis of the scattering methods adopted further: the technique of low angle light scattering (LALS), the dynamic light scattering (DLS) [12, 13, 14], and the near field scattering technique (NFS) [15, 16]. This is a recently introduced technique that allows to study both static and dynamic properties of a colloidal suspension, as LALS and DLS.

Chapter 3: COLLOID Experiment

The COLLOID experiment was an experiment performed aboard the International Space Station as a collaboration of Unimi and UVA (Amsterdam university), founded by ESA (European Space Agency) [17]. It is devoted to the study of colloidal aggregation induced by critical Casimir forces. In this section I focus on the dynamic analysis, and in particular on the possibility of combining information on static (gyration radius and fractal dimension) and dynamic properties (hydrodynamic radius)[18] of the aggregates. These combined measurements are used in the fields of macromolecules to study the internal structure of particles (see for examples [19, 20]). The COLLOID experiment takes advantage of some properties of the NFS techniques in performing combined analysis,

like the possibility of collecting information simultaneously on a wide range of scattering vectors.

Chapter 4: Salt Induced Aggregation

In this section the analysis of aggregation processes induced by adding salt to a colloidal suspension are shown. In particular the data are collected with two different techniques: the NFS and the single particle extinction and scattering (SPES). This technique allows to measure the size distribution of the particles and their fractal dimension. By combining this information with the measurements obtained with NFS, an accurate study of the effect of polidispersity is shown.

Chapter 5: Anisotropic Interactions

After COLLOID, a new experiment is going to be performed on the ISS. It is the Advanced Colloid Experiment (ACE) in which the aggregation is induced by critical Casimir interaction on anisotropic particles. This experiment will be performed with confocal microscopy technique. In this section a characterization of the samples that will be used in the space experiment is shown. These anisotropic particles are studied with different optical techniques to have a better understanding on the particles themselves and on their aggregation processes.

Appendix A: Calibration

A detailed explanation of the calibration procedure for a typical NFS apparatus is shown. In particular the calibration of the magnification of a microscope objective and the spectral response of the CCD camera are explained.

Appendix B: Expression for the Parameter β

In comparing static and dynamic properties the parameter $\beta = R_H/R_g$, ratio between hydrodynamic and gyration radii is introduced [21]. It is directly related to the structure of the aggregates via the density (or correlation) function of a single aggregates. To keep into account for finite size of the aggregate a cutoff function is introduced. The expression of β changes with the cutoff function [22]. In this section I report how to obtain β for three different cutoff shapes: exponential, gaussian and unit-step functions.

Chapter 1

Colloidal Interactions

In every colloidal system there are interactions. Those interactions occur between the same particles and also between the particles and the solvent in which they are in. The first simple kind of interaction is the steric interaction between colloidal particles. It means that each particle can't superimpose to others creating an excluded volume. Obviously this is the shortest range of interaction that can be considered. In fact it is relevant only when particles touch. The other kinds of interactions that will be described have longer range than the hard body. In this section I will describe the electrostatic, the Van der Waals and the critical Casimir interactions. All of these will be described by their potentials, calculated under the assumption of the DLVO (Derjaguin, Landau, Vervey and Overbeeck) theory. The key point of this theory is that the potentials between colloidal particles are assumed to be additive. It allows to calculate the potential for each kind of interaction neglecting the others and then find the total interaction potential just adding the different contributions. Other useful assumptions will be shown along the discussion. Obviously this section doesn't want to be a fully exhaustive explanation of the theory of colloidal interactions. In this section I just want to introduce the players in colloidal interactions and their roles.

1.1 Van Der Waals interaction

The Van der Waals interaction arises because of dipole interaction [11]. The dipoles can be distinguished in three different species: a permanent dipole, a dipole induced by an external electric field or a dipole oscillating in time that arises from the fluctuation around the nucleus of the electron cloud.

1.1.1 Atoms or Molecules

The first kind of dipole interaction that is considered is the dipole−dipole interaction due to permanent dipoles, also called orientational or Keesom interaction. The potential that describes this interaction represents the change in free energy when the two dipoles approach from infinite to a distance r. Because this potential depends on the reciprocal orientation between the two different dipoles, it is weighted by an orientational distribution of the dipole moments m. The final result of these calculations is

$$w_o(r) = -\frac{m_1^2 m_2^2}{3k_B T(4\pi\varepsilon_0)^2}\frac{1}{r^6} = C_o\frac{1}{r^6}. \tag{1.1}$$

It is interesting to notice that this potential decays with $1/r^6$.

In addition to this, a permanent dipole induces a dipole on a second molecule depending on its polarizability. This second interaction is called Debye or induction interaction, and occurs between a permanent dipole and an induced dipole. If both molecules have a permanent dipole moment m_i and are characterized by a polarizability α_i, the Debye potential of interaction is

$$w_i(r) = -\frac{m_1^2\alpha_2 + m_2^2\alpha_1}{(4\pi\varepsilon_0)^2}\frac{1}{r^6} = C_i\frac{1}{r^6}. \tag{1.2}$$

Also the induced dipolar interaction has a $1/r^6$ dependence, like the orientational one.

The third kind of interaction depends on the atomic nature itself and does not need a permanent dipole to take place. It is called London dispersion interaction. A single electron that is spinning around the nucleus describe a circular motion with a mean radius a_0. An instantaneous dipole can be defined as $m_1 = ea_0$. This dipole generates an instantaneous electrostatic field that induces a dipole on a second atom, depending on its polarizability. Considering two different atoms, the potential of interaction between these two dipoles is

$$w_d(r) = -\frac{3}{4}\frac{\alpha_1\alpha_2}{(4\pi\varepsilon_0)^2}\frac{I_1I_2}{I_1+I_2}\frac{1}{r^6} = C_d\frac{1}{r^6}. \tag{1.3}$$

where I_i is the first ionization energy of i-th atom or molecule. Still notice that also this potential decays with $1/r^6$.

The atomic or molecular Van der Waals interaction can be finally summarized in the expression

$$w_{vdW} = -(C_o + C_i + C_d)\frac{1}{r^6} = -\frac{C_{vdW}}{r^6} \tag{1.4}$$

that keeps account for three different contributions. In most of the cases the dominating contribution is the dispersion one, except for when the molecular dipoles are very large and the polarizability very low. A typical feature of the van der Waals interaction is that it is always attractive, independently on which is the main contribution.

1.1.2 Colloidal Spheres

The expressions of the previous section are related to van der Waals interaction between atoms or molecules. Now I want to find the expression for the Van der Waals interaction in a colloidal system. The simplest way to proceed is to make the assumption of pair wise additivity of the potential. Consider a colloidal sphere and a single molecule. The colloidal sphere is composed by N molecules of the same kind, so that the potential can be represented as the sum over all the N molecule-molecule interactions. Introducing the number density ρ, the sum can be replaced by an integral obtaining:

$$W_{MS}(r) = -\rho C_{vdW}\int_{V_S}\frac{1}{r^6}dV \tag{1.5}$$

where the integration is on the volume of the colloidal sphere. The interaction potential between two spheres is obtained with an integration on the volume of the second sphere. The final expression for the potential is

$$\phi_{SS}^{vdW} = -\frac{A_H}{6}\left(\frac{2R_1R_2}{r^2-(R_1+R_2)^2} + \frac{2R_1R_2}{r^2-(R_1-R_2)^2} + ln\left[\frac{r^2-(R_1+R_2)^2}{r^2-(R_1-R_2)^2}\right]\right) \tag{1.6}$$

where $A_H = \pi^2\rho^2 C_{vdW}$ is the Hamaker constant, that tunes the strength of interaction. The assumption of additivity of the molecular potential is a very strong restriction. It neglects the interactions with a third atom, or the orientational interactions with other induced dipoles. This approximation is good for an highly diluted system. For colloidal particles interacting in a solvent this assumption is no more valid. In this kind of system the interaction potential is calculated via the Lifshitz theory, which considers the particle and the suspending medium as a continuum. The result is very similar to the one obtained previously; the only thing that changes is the expression of the Hamaker constant. For particles of the same material with refractive index n_1 the expression for the Hamaker constant is

$$A_H \approx \frac{3}{4}k_BT\left(\frac{\varepsilon_1-\varepsilon_2}{\varepsilon_1+\varepsilon_2}\right)^2 + \frac{3h\nu_e}{16\sqrt{2}}\frac{(n_1^2-n_2^2)^2}{(n_1^2-n_2^2)^{3/2}} \tag{1.7}$$

where *h* is Plank's constant, ν_e is the main electronic absorption frequency of the medium, subscript 1 stay for the particle and 2 for the medium. For many materials the refractive index is approximately the square of the dielectric constant. In this condition if particles and solvent match their refractive indexes, Van der Waals interaction is approximately zero. However for water as a solvent, A_H never becomes smaller than $0.7k_BT$ because of the large value of the water dielectric constant $\varepsilon_{H_2O} = 81$. In fig. 1.1 is represented this kind of potential. Its divergence for surface-surface distance near to zero shows the

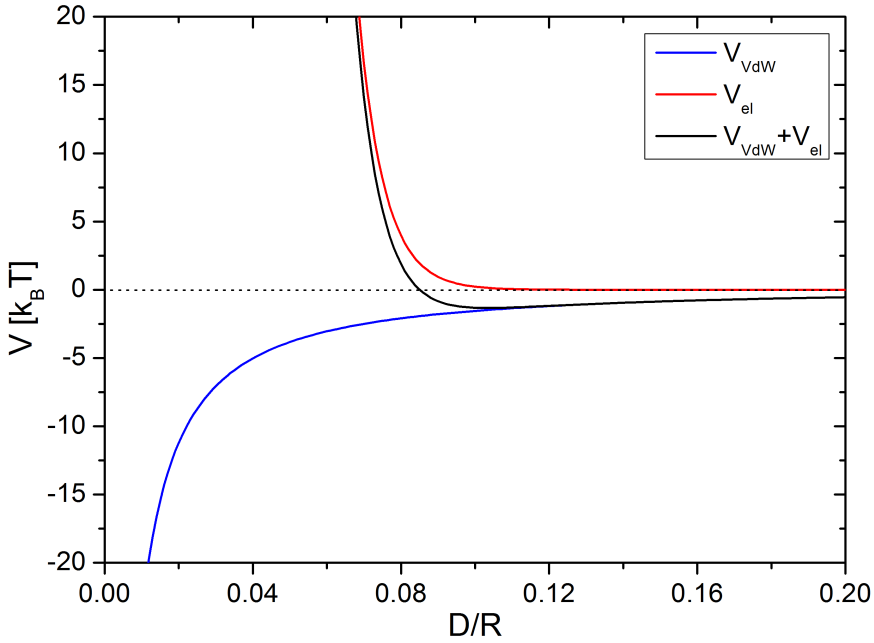

Figure 1.1: Example of van der Waals and electrostatic potentials. It is also represented a combination of them. The parameter used for the potential are: $R = 1\mu m$, $A_H = 3.14k_BT$ (polystyrene in water), $\varepsilon = 17$, $\lambda = 7nm$, $\sigma = 0.0272C/m^2$ and $T = 300K$.

attractive feature of this interaction and the collapsing behavior without the presence of other kind of stabilization.

1.2 Derjaguin approximation

A less rigorous way to find an expression for Van der Waals forces is based on the interaction between two flat surfaces. Considering the shape of the particles, it can be sliced in flat surfaces of different dimensions. The Derjaguin approximation is based on considering all these flat surfaces composing the particles and then the interaction potential is computed as the superposition of all the interaction potentials between the flat surfaces of the two different particles. A simple sketch of this kind of approximation is shown in figure 1.2. Consider a molecule and a flat walls as in fig. 1.2a, the Van der

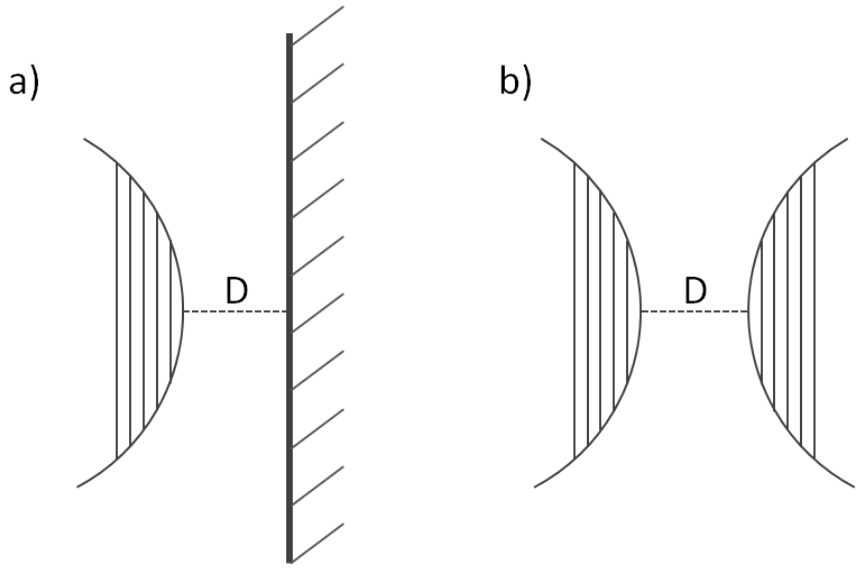

Figure 1.2: Sketch of the Derjaguin approximation.

Waals interaction potential is

$$W_{MW}(D) = -\frac{\pi\rho C_{vdW}}{6D^3} \tag{1.8}$$

where D is the shortest distance between the molecule and the wall. The interaction between two flat walls can be now computed integrating the expression 1.8 over all the positions of the molecule on a wall. The expression is

$$\phi_{WW}^{vdW,a}(D) = -\frac{\pi\rho^2 C_{vdW}}{12D^2} \tag{1.9}$$

where *a* stands for the unit of area to avoid diverging potential values caused by the integration on the infinitely extended wall. With a very similar procedure, the expression for the potential between the sphere and the wall can be computed integrating the expression 1.8 on the volume of the sphere. In the limit of $R \gg D$, the sphere-wall interaction potential become

$$\phi_{SW}^{vdW}(D) = -\frac{\pi^2\rho^2 C_{vdW} R}{6D} \tag{1.10}$$

and the force between the sphere and the wall is

$$F_{SW}(D) = -\frac{\partial \phi_{SW}^{vdW}(D)}{\partial D} = -\frac{\pi^2 \rho^2 C_{vdW} R}{6D^2}. \tag{1.11}$$

A comparison with eq. 1.9, shows that

$$F_{SW}(D) = 2\pi R \phi_{WW}^{a}(D). \tag{1.12}$$

This relation explains the Derjaguin approximation. It creates a relation between the wall-wall potential and the sphere-wall force at the same distance in the limit $D \ll R$. This relation can be generalized for two spheres, see fig.1.2b, as

$$F_{SS}(D) = -2\pi \frac{R_1 R_2}{R_1 + R_2} \phi_{WW}^{a}(D). \tag{1.13}$$

By this expression the potential of interaction is easily calculated to be

$$\phi_{SS}^{vdW}(D) = -\int_D^\infty dD F_{SS}^{vdW}(D) = -\frac{A_H R}{12D}. \tag{1.14}$$

This is the same result obtained via eq. 1.6 in the limit case $r \ll R$.

1.3 Electrostatic interaction

In the previous section Van der Waals interaction was discussed. Its main feature is that the interactions between colloidal particles are always attractive. For the stability of a colloidal solution, there must be something that may balance this effect. The electrostatic repulsion is what stabilizes colloids preventing aggregation [11].

1.3.1 Point-like charge

The electrostatic potential of a charged particle in a solution can't be solved easily via Coulomb interaction, because of the presence of the ions in the solution. These ions have a screening effect on the charged particles. The expression of the electrostatic interaction comes out from the Poisson equation

$$\nabla^2 u_P(\overrightarrow{r}) = \frac{1}{r}\frac{\partial^2}{\partial r^2}(r u_P(r)) = -\frac{\rho(r)}{\varepsilon \varepsilon_0} \tag{1.15}$$

where $u_P(r)$ is the potential of the point-like source, $\rho(r)$ the charge density, ε the dielectric constant of the solvent and ε_0 the vacuum permittivity. The Laplace operator has been expressed in polar coordinates without the angular dependence because of the spherical symmetry of the potential. The charge density can be represented as the sum of the micro-ions density N multiplied by their charge

$$\rho(r) = \sum_j N_j(r) e Z_j \tag{1.16}$$

where e is the elementary charge and Z_j the number of elementary charges for j-th specie. The number density of the different species can be approximated by a Boltzmann distribution

$$N_j(r) = N_j^0 \exp(-\beta Z_j e u_P(r)) \tag{1.17}$$

where N_j^0 is the number density at zero potential. Using this expression in Poisson equation and under the approximation of small potential, the charge density can be Taylor-expanded to the linear term. The linearized Poisson-Boltzmann equation is

$$\frac{1}{r}\frac{\partial^2}{\partial r^2}(ru_P(r)) \approx \frac{\sum_j N_j(r)eZ_j}{\varepsilon\varepsilon_0}(1+\beta Z_j e u_P(r)) \tag{1.18}$$

The first term of the Taylor expansion vanishes because the total system is usually electrically neutral. Defining $\kappa^2 = \beta e^2 \sum_j N_j^0 Z_j^2/\varepsilon\varepsilon_0$, the Poisson-Boltzmann equation becomes

$$\frac{1}{r}\frac{\partial^2}{\partial r^2}(ru_P(r)) = \kappa^2 u_P(r) \tag{1.19}$$

This expression is called Debye-Hückel equation. Solving it and imposing the boundary conditions, the solution of the electrostatic potential of a point-like source of charge $Z_P e$ is

$$u_P(r) = \frac{Z_P e}{4\pi\varepsilon\varepsilon_0}\frac{1}{r}\exp(-\kappa r) \tag{1.20}$$

The decay length κ^{-1} is called Debye screening length, usually indicated with λ_D.

1.3.2 Charged colloidal sphere

For a uniform charged colloidal sphere the electrostatic potential can be computed via the linearized Poisson-Boltzmann equation. Considering a sphere with radius *R*, if the layer of screening charges is large compared to the sphere radius, i.e. for $\kappa R \lesssim 5$, eq. 1.18 becomes

$$\frac{1}{r}\frac{\partial^2}{\partial r^2}(rU_S(r)) = \begin{cases}\kappa U_S(r) & \text{for r>R}\\ 0 & \text{for 0<r<R}\end{cases} \tag{1.21}$$

Solving the differential equation and imposing the contour conditions the expression of the potential for $r > R$ is given by

$$U_S(r) = \frac{Z_S e}{4\pi\varepsilon\varepsilon_0}\frac{\exp(\kappa R)}{1+\kappa R}\frac{\exp(-\kappa r)}{r} \tag{1.22}$$

where Z_S is the number of elementary charges on the sphere. In the limit $R \to 0$ it reduces to eq. 1.20. If the layer of screening charges is small compared to the sphere radius, it is more appropriate another approximation. The limit case $R \to \infty$ means to solve a differential equation for flat wall of charge density σ of the form

$$\frac{\partial^2 U_W(D)}{\partial D^2} = \kappa U_W(D) \tag{1.23}$$

where D is the distance from the wall. The solution has the simple form

$$U_W(D) = \frac{\sigma}{\varepsilon\varepsilon_0\kappa}\exp(-\kappa D) \tag{1.24}$$

Both equations 1.22 and 1.24 express the electrostatic potential around the charged surface. For colloidal interaction it is more interesting and more useful to know the interaction potential between two charged entities. The electrostatic pair potential is

$$\phi_{SS}^{er}(r) = \frac{e^2 Z_S^2}{4\pi\varepsilon\varepsilon_0}\left(\frac{\exp(\kappa R)}{1+\kappa R}\right)^2\frac{1}{r}\exp(-\kappa r) \tag{1.25}$$

in the first limit considered, i.e. $\kappa R \lesssim 5$ and $r > 2R$. For the two parallel walls of surface A the potential is

$$\phi_{WW}^{er,a}(r) = \frac{e^2 Z_W^2}{\varepsilon\varepsilon_0 A\kappa} \exp(-\kappa D) \tag{1.26}$$

where the superscript a stands again for the unit of area. Further, this potential between the two walls can be used to calculate the interaction potential between two spheres of radius R using the Derjaguin approximation. The result of this calculation is

$$\phi_{SS}^{er}(D) \approx \frac{e^2 Z_S^2}{8\pi\varepsilon\varepsilon_0} \frac{1}{R^3\kappa^2} \exp(-\kappa D) \tag{1.27}$$

that holds if the layer of micro-ions is significantly smaller than the spheres radius. An example of electrostatic potential is represented in fig. 1.1. It is also represented a combination of electrostatic and Van der Waals potentials. The presence of the electrostatic potential acts as a stabilization factor for this kind of particles because it creates a potential barrier for zero distance. With this parameter however the aggregation is not totally inhibited because of the presence of the minimum, even if the potential well is small.

1.4 Casimir interaction

The last kind of interaction considered in this section is the critical Casimir effect. It is a transposition on a classical system of a typical quantum effect. They arise when some local constraints are imposed to fluctuations; vacuum state fluctuations for the quantum effect or critical fluctuations for a classical system.

1.4.1 Quantum Casimir effect

The first field in which Casimir effect was predicted is the quantum mechanics. In 1948 Casimir published a paper [4] in which he showed that the fluctuations of the vacuum state of the electromagnetic field induce an attractive strength between two plane plates which are conducting but not charged. Consider a cubic cavity of side L composed by perfect conducting plates. Inside the cavity there are quantum fluctuations of the vacuum state. The frequencies of these fluctuations are the resonance frequencies of the cavity whose wave vectors are

$$k = \frac{\pi}{L} n \tag{1.28}$$

where n is a positive integer (see figure 1.3 for a simplified sketch). If the cavity is sufficiently large those values can be considered as continuum variables. Consider now the same cavity but with a plate close to its opposite one, at a distance a. The wave number of this new cavity has still the expression 1.28, where a takes the place of L. In both cases, the expression $\frac{1}{2}\sum \hbar\omega$, where the sum is over all the resonance frequencies of the cavity and has no physical meaning because of the divergence. But the energy difference δE between the summation of full cavity and reduced cavity assumes a finite value. The expression of δE is

$$\frac{\delta E}{L^2} = -\frac{\pi^2}{720} \frac{\hbar c}{a^3} \tag{1.29}$$

and the resulting force per unit of area A on the plates is

$$\frac{F}{A} = -\frac{\pi^2}{240} \frac{\hbar c}{a^4}. \tag{1.30}$$

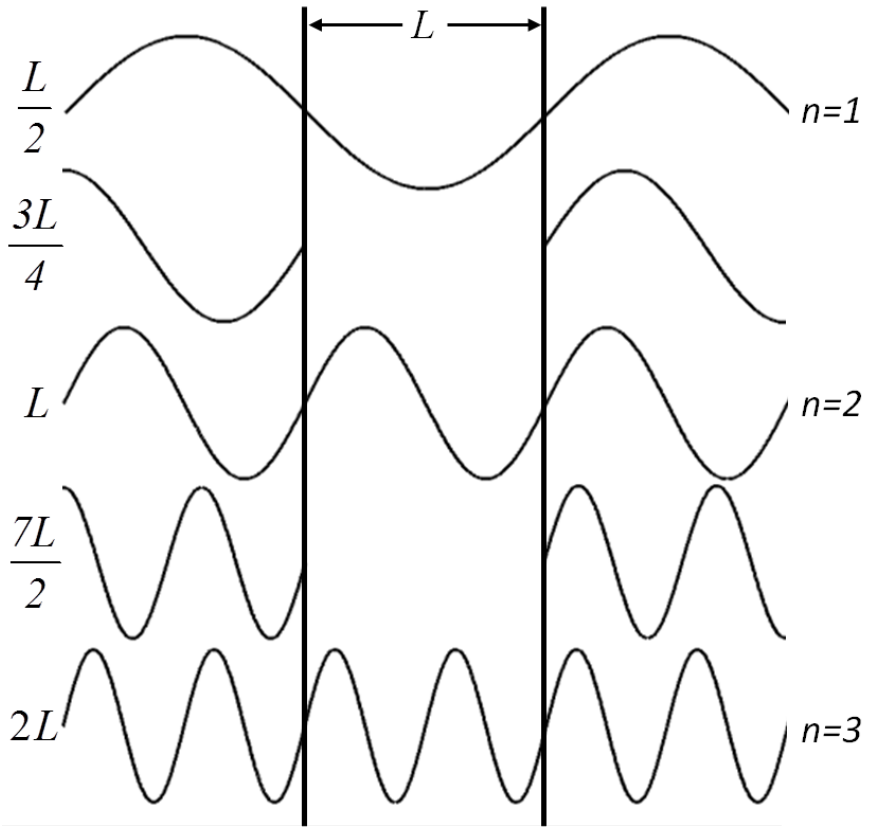

Figure 1.3: Simple sketch for the boundary conditions imposed to fluctuation to have Casimir interaction.

It means that a confinement of the vacuum fluctuation is sufficient to create an attractive strength between two plane plates at a sufficiently close distance. It is very interesting to notice that this interaction force does not depend on the material properties of the plates, but only on the distance and on some universal constants as c and $\hbar$. The first accurate measurement of this effect was made only in 1997 [5] because the force is very weak: for two plates of $1mm^2$ of area at a distance of $1\mu m$, the attractive force is $10^{-9}N$.

1.4.2 Critical Casimir effect

In 1978 Michael Fisher and Pierre-Gilles de Gennes theoretically extended the Casimir effect to a classical system [6]. As is well known by thermodynamic, near a second-order phase transition the order parameter increases and a collective behavior of the molecules comes out. In particular the fluctuations of the order parameter have a correlation length which increases with $T - T_c = \Delta T \to 0$ as a power law. These fluctuations take the role of the vacuum state fluctuations, so the Casimir attraction may also occur in this classical system. The need of the critical point is the reason why the "classical" Casimir effect is called critical Casimir.

Consider now a binary liquid mixture, which phase diagram is sketched in fig. 1.4. This binary mixture has two different states, mixed or separated, depending on the mass

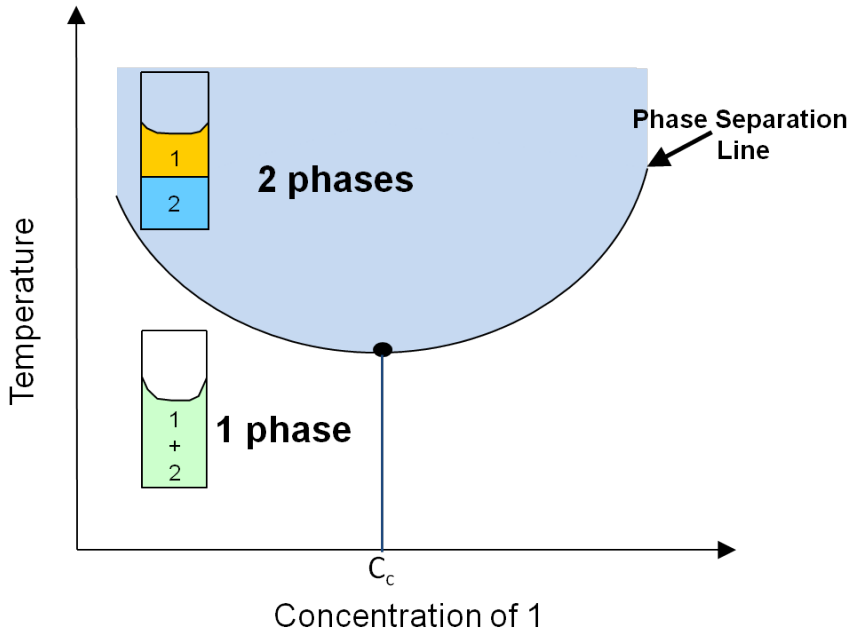

Figure 1.4: Simplified phase diagram of a binary mixtures.

fraction of the two liquids and on the temperature. Near the critical point, and more in general near the phase transition line, the fluctuations of the density, that is the order parameter of this system, increase depending on ΔT. The correlation length of the

fluctuations is related to the temperature via the formula

$$\xi \approx \xi_0 \left(1 - \frac{T}{T_c}\right)^{-\nu} \tag{1.31}$$

where ξ_0 is a typical length scale of the intermolecular potential and $\nu \sim 0.63$ the characteristic exponent at the critical point. If two plates are inserted in the binary mixture at sufficiently close distance, they set some boundary conditions to the fluctuations, as sketched in fig. 1.5. The resulting critical Casimir force on the plates is

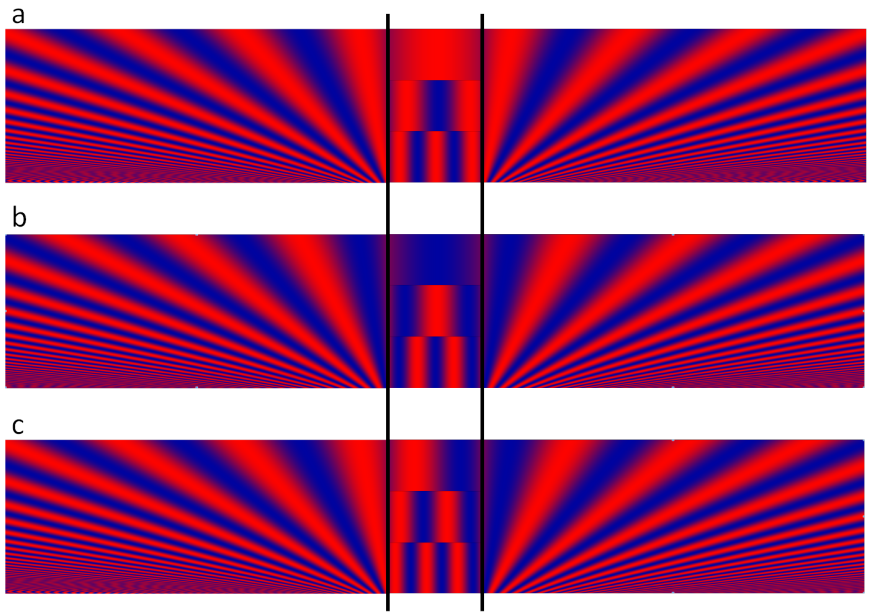

Figure 1.5: Examples of confinement of critical fluctuations between two walls. The red and the blue colors represent the two different liquids. The black line are the plane plates that impose boundary conditions. In *a* they prefer the red liquid; in *b* they prefer the blue liquid. Both these situations have symmetric boundary condition. The *c* condition represents the asymmetric boundary condition: the left wall prefer the red liquid while the right one the blue.

$$\frac{F}{A} = \frac{k_B T}{L^3} \Theta(L/\xi) \tag{1.32}$$

where A and L are respectively the area and the distance of the plates and $\Theta(x)$ a universal scaling function. The range of this force depends on the correlation length ξ of the critical fluctuation, which is a function of T. The shape of the function $\Theta(x)$ can be determined via Monte Carlo simulations imposing boundary conditions. The Casimir forces can be attractive or repulsive depending on the boundary conditions [10]: if those are symmetric, i.e. the plates prefer the same liquid of the binary mixture, the force is attractive otherwise the force is repulsive. Those are the two differences with the quantum Casimir effect: the possibility of changing the range of the force and the choice between the attractive or repulsive behavior.

An easier way to measure the critical Casimir force is to consider not the interaction between two flat walls but the force acting on a spherical particle and a wall [7]. To calculate the interaction potential is natural to use the potential between two flat wall and the Derjaguin approximation. The critical Casimir potential takes the form

$$\frac{\phi_c(z)}{k_B T} = \frac{R}{z}\vartheta(z/\xi) \tag{1.33}$$

where R is the radius of the sphere, z the distance and ϑ a universal function that can be expressed in terms of Θ. As for Casimir forces between two flat walls the shape of the potential depends on the boundary conditions. The critical Casimir forces may occur also between spherical particles [8], [9]. The potential can be computed again via the Derjaguin approximation, leading to an approximate expression

$$\phi_C^{SS}(z) \approx -\frac{2\pi R k_B T}{\xi}\exp(-z/\xi) \tag{1.34}$$

The advantage of using critical Casimir interaction to make particles interact is the possibility of tuning the interaction forces just changing a macroscopic parameter like the temperature. An example of critical Casimir interaction is represented in figure 1.6 and also a combination with electrostatic potential is represented. The presence of the minimum represents again the aggregation of colloidal particles.

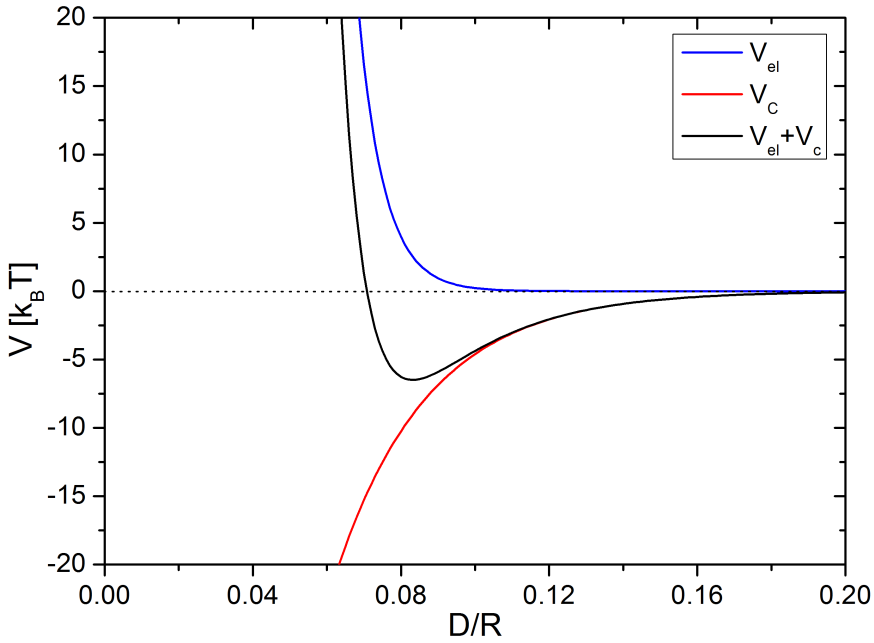

Figure 1.6: Example of electrostatic and critical Casimir potentials. It is also represented a combination of them. The value of ξ is $25nm$. The other parameters are the same of graph 1.1.

Chapter 2

Near Field Scattering

There are two typical ways to study the behavior of colloidal systems, which are the microscopy and the light scattering with all their peculiar set-up that make them suitable for the features that must be studied. In this section I will focus on some scattering techniques devoted to the study of two typical features of those systems: the form factor and the diffusion coefficient. Those quantities are both related to particles but the first is related to some static properties, i.e. how particles diffuse light as a function of the angle, and the second is the diffusion coefficient, i.e. the hydrodynamic properties of the particles themselves.

Traditional scattering experiments are performed in the far field. It means that the scattered light is collected far from the sample at a distance such that the contributions at different angles are all separated. The two main used techniques are the low angle light scattering (LALS) to study the form factor and the dynamic light scattering (DLS) to study the diffusion coefficient.

Recently a novel technique to study colloidal systems in the near field had been introduced with the name of near field scattering (NFS). With this technique the same informations of the two previous techniques can be obtained studying the scattered field near the sample, with some advantages that will be described later on.

2.1 Low Angle Light Scattering

The LALS technique is devoted to measure the scattered light of a sample as a function of the scattering angle. A typical experimental layout is sketched in fig. 2.1. A laser beam, after a spatial filter, is sent on the sample. The light is scattered and the radiation is then collected in the far field or in the focal plane of a lens with a photo-diode or a photomultiplier (PMT). Usually the detector can move on a circle centered in the sample to change the angle. This system has to be aligned very well to collect all the light scattered and to find the correct intensity profile. Another issue that usually affects this system is the presence of stray light. An accurate measurement of the static contribution must be performed before every acquisition to have a reliable measurement of the intensity distribution. The angular range in which the acquisition is performed is usually small, because the interesting features of the sample are in this low angle regime.

With this technique the static form factor of the sample is measured. It is directly related to the shape of the particles in the sample and also on their interaction [12, 13]. It describes the shape of the particles in the Fourier space of spatial frequencies. In more details it is the Fourier transform of the pair correlation function of the sample.

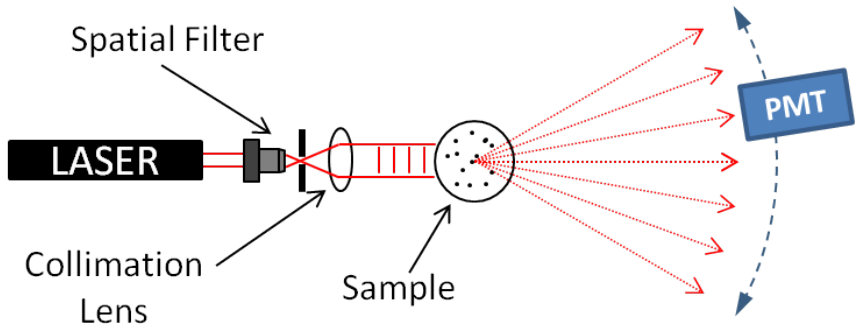

Figure 2.1: Typical apparatus for a low angle light scattering measurement

The pair correlation function of the sample can be related to angular intensity profile in a trivial way. Consider the pair correlation function as a superposition of sinusoidal pattern, i.e. its Fourier decomposition. Every sinusoid of wavelength Λ diffuses light only at two different wavevector, $+q$ and $-q$. The values of those scattering vectors are related to the wavelength via the relation $q = 2\pi/\Lambda$. Also the intensity of the scattered light at q-angles depends on the value of its Fourier component. The superposition of all those sinusoidal patterns with their scattered radiations create an intensity distribution at different q-vectors that is proportional to the Fourier transform of the pair-correlation function of the sample, i.e. the static form factor.

2.2 Dynamic Light Scattering

The DLS technique is used to study dynamic properties of the sample [14]. The experimental set-up is represented in the fig. 2.2. The illumination system is the same one of the LALS scheme, while the way of collecting light and the kind of analysis change. In fact the light is usually acquired at a single angle, usually $90°$, with a PMT. The fluctuations of the signal are the relevant part and via the auto-correlation function of the signal some information about the dynamic of the sample is found. Also for this system is required a strict alignment and also the mechanical stability has to be very good.

The fluctuations of the signal are directly related to the internal motion of the sample. Consider a colloidal solution of particles in water. The function that better describes the motion of the particles is the correlation function of the density in time, expressed by

$$G_\rho(\mathbf{r},\tau) = \frac{\langle \rho(\mathbf{r},t)\rho(\mathbf{r},t+\tau)\rangle_t}{\langle \rho(\mathbf{r},t)\rangle_t^2}. \tag{2.1}$$

Consider just one particle and suppose that at the beginning it is in a certain position. It moves by Brownian motion around the starting position as time increases. The Brownian motion is described by the diffusion equation

$$\frac{\partial G_\rho(\mathbf{r},\tau)}{\partial \tau} = D\nabla^2 G_\rho(\mathbf{r},\tau) \tag{2.2}$$

where D is the diffusion coefficient. Usually it is expressed via the Stokes-Einstein rela-

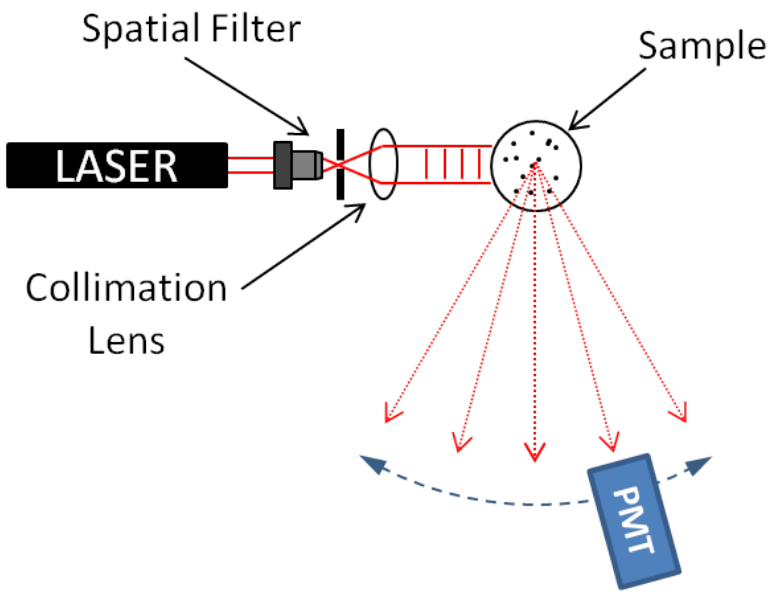

Figure 2.2: Typical apparatus for a dynamic light scattering measurement.

tion

$$D = \frac{k_B T}{6\pi\eta R_H} \tag{2.3}$$

where k_B is the Boltzmann constant, T the absolute temperature, η the viscosity of the liquid and R_H the hydrodynamic radius. The diffusion equation can be easily solved in the Fourier space of spatial frequencies. Using the properties of the Fourier transform the diffusion equation 2.2 becomes

$$\frac{\partial G_\rho(\mathbf{q},\tau)}{\partial \tau} = -D\mathbf{q}^2 G_\rho(\mathbf{q},\tau). \tag{2.4}$$

For sake of simplicity the Fourier transform of the correlation function has the same name as before while the variables change and the function obviously has a different expression. The solution of this equation is now very simple and it is described by a decaying exponential function

$$G_\rho(\mathbf{q},\tau) = \exp(-Dq^2\tau). \tag{2.5}$$

This function can be directly related to the scattered field at the scattering vector $\mathbf{q}$ as in the previous section. Also the auto-correlation function of the scattered field is described by the expression 2.5. But with the PMT what is measured is not the electrical field but the intensity of the scattered radiation. The expression of the intensity auto-correlation function is directly related to the one of the field via the Siegert relation

$$G_I(q,\tau) = 1 + G_E^2(\mathbf{q},\tau). \tag{2.6}$$

Studying the auto-correlation of the scattered signal and fitting it with the expression 2.6 the decaying time $1/2Dq^2$ is found and then the radius of the particles. In figure 2.3 there is an example of the auto-correlation function measured with a DLS apparatus.

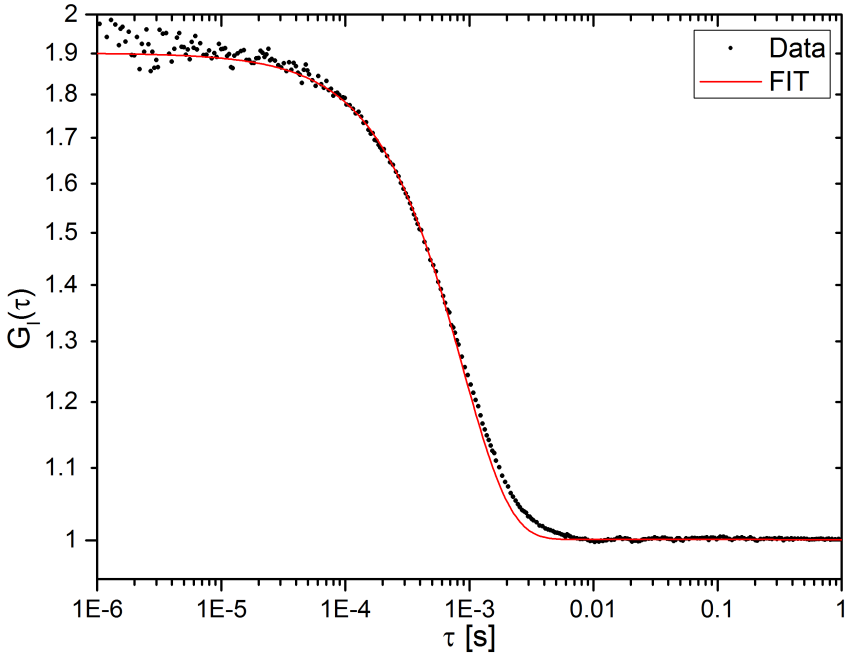

Figure 2.3: Auto-correlation function measured with a DLS apparatus. The sample is composed by cerium oxide suspended in water. The characteristic time is around $7 \cdot 10^{-4} s$ for a hydrodynamic radius of 0.1 μm.

2.3 Near Field Scattering

The NFS is a scattering technique recently introduced that can be used to measure the static form factor and the diffusion coefficient [15, 16] of the particles in a solutions. The experimental apparatus is quite simple, and is showed in fig. 2.4. A laser beam

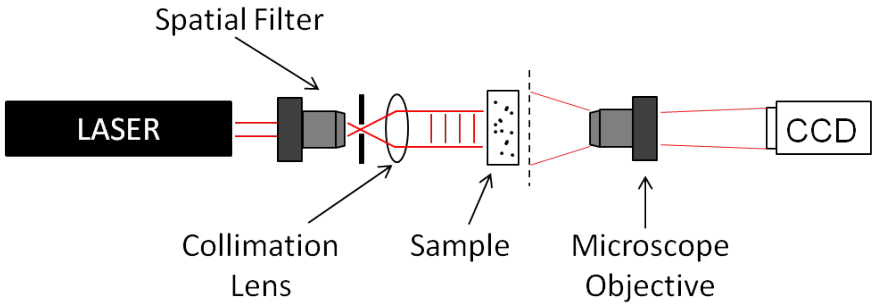

Figure 2.4: Typical apparatus for a near field scattering measurement

after being spatially filtered and collimated is sent on the sample. The scattered light is collected with a microscope objective that couples a plane near the sample with a CCD camera that acquires the images. The images are elaborated via software obtaining the angular distribution of the intensity. In traditional techniques, as LALS and DLS, the far field condition is obtained using optical devices like a lens. In the focal plane of the lens, that is ideally the infinite distance, we have the Fourier transform of the scattered radiation. This procedure in NFS measurements is performed via software. Starting from the acquired images the Fourier transform is computed and then the spectral distribution of the intensity is found. Even if the different kind of measurements have the same result, NFS technique has some advantages. The first is that the requirement about alignment is not so strict as for LALS or DLS. The second is that every single acquisition contains the information on a wide range of scattering angles. This last advantage is directly related to the collection of the light near the sample.

2.3.1 Near field condition

Consider a particle of a certain dimension d. When a monochromatic radiation of wavelength λ is sent on the particle it creates a diffraction pattern whose first minimum is given by

$$\vartheta \approx \frac{\lambda}{d} \tag{2.7}$$

and the scattered radiation is diffused within this first diffraction minimum. In spite of a single particle let's consider a collection of particles and an illuminating laser of diameter D. At a certain distance z from the sample a sensor is placed. It will collect the light diffused from the sample inside an angular region

$$\varphi \approx \frac{D}{z}. \tag{2.8}$$

In the far field condition, i.e. $z \longrightarrow \infty$, this angular region φ is very small and the sensor collects the emitted light from the entire illuminated region only at one angle, depending

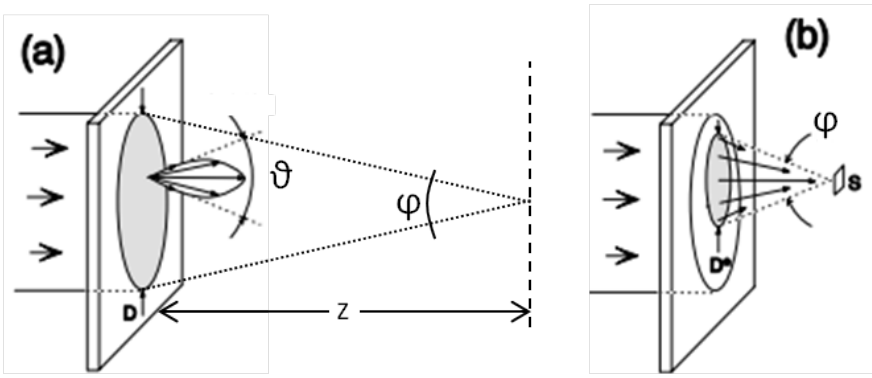

Figure 2.5: Scheme for the near field condition. (a) represent the far field condition and (b) the near field condition.

on the transversal position of the sensor respect to the sample. If instead the sensor is at a distance such that $\varphi > \vartheta$, it will collect the light only from a partial region D^* of the illuminated sample. In addition the collected light is the one diffused not only at one angle but at all the angles within the scattering cone. This is the near field scattering condition, and the relation $\varphi > \vartheta$ can be converted in a more useful condition on the distances

$$z < z^* = \frac{dD}{\lambda}. \tag{2.9}$$

If the particles have $d = 1\mu m$, the laser beam diameter is about of $1cm$ with wavelength $633nm$, z^* is about $15mm$.

2.3.2 Heterodyne NFS

In NFS measurements there are two configurations depending on the properties of the sample. Those two different conditions are named homodyne an heterodyne. The first is obtained when there isn't the transmitted beam and after the sample there is only the scattered field. The second is the opposite condition, so there is the transmitted beam and only a little part of the incoming beam, some percent, is scattered. Here I will focus only on the heterodyne layout.

The resulting field after the scattering process of the sample is

$$e(\mathbf{r}, t) = e_0(\mathbf{r}) + e_S(\mathbf{r}, t) \tag{2.10}$$

where e_0 is the transmitted beam that does not depend on time and e_S is the scattered signal. The intensity measured is now easily calculated as

$$i_S(\mathbf{r}, t) = i_0(\mathbf{r}) + e_0(\mathbf{r})e_S^*(\mathbf{r}, t) + e_0^*(\mathbf{r})e_S(\mathbf{r}, t) \tag{2.11}$$

where the term $|e_S(\mathbf{r}, t)|^2$ is negligible in respect to the others. Before computing the Fourier transform of the field it is useful to subtract the static contribution $i_0(\mathbf{r})$. There are two different ways of doing this. The first is to perform a time average of the signals that deletes the random scattered fields. The result is the static contribution that can be easily subtracted. The second is to subtract two images at a well known time distance: the static contribution is the same in both the images and is well subtracted. This second

procedure if available is the best one, both for the reliability and for the instrumental requirement. In fact if the first requires that the static background doesn't change for the entire measurement, the second requires only that it doesn't change for the temporal distance of the two acquisition.

Consider now this second procedure. The resulting signal is

$$\begin{aligned}\delta i_S(\mathbf{r},t,\tau) &= i_S(\mathbf{r},t+\tau) - i_S(\mathbf{r},t) \\ &= 2Re[e_0^*(\mathbf{r})e_S(\mathbf{r},t+\tau) - e_0^*(\mathbf{r})e_S(\mathbf{r},t)].\end{aligned} \tag{2.12}$$

The power spectrum associated with this signal is

$$\begin{aligned}|I(\mathbf{q},t,\tau)|^2 \sim &|E(\mathbf{q},t)|^2 + |E(-\mathbf{q},t)|^2 + |E(\mathbf{q},t+\tau)|^2 + |E(-\mathbf{q},t+\tau)|^2 \\ &- 2Re[E(\mathbf{q},t)E^*(\mathbf{q},t+\tau) + E(-\mathbf{q},t)E^*(-\mathbf{q},t+\tau)] \\ &+ 2Re[E(\mathbf{q},t)E^*(-\mathbf{q},t) + E(\mathbf{q},t+\tau)E^*(-\mathbf{q},t+\tau)] \\ &- 2Re[E(-\mathbf{q},t)E^*(\mathbf{q},t+\tau) + E(\mathbf{q},t)E^*(-\mathbf{q},t+\tau)]\end{aligned} \tag{2.13}$$

where $E(\mathbf{q},t)$ is the Fourier transform of $e_S(\mathbf{q},t)$. For a stationary sample each term of the first line represent $I_S(q)$ and it is equal to the others. The second line represents the correlation of the signal for a fixed lag-time τ. Notice that in this line both the multiplied terms appear with the same wavevector. On the other hand in the last two lines only opposite wavevectors appear; those latter terms represent the shadowgraph or Talbot oscillation. They are usually relevant in a low-q regime and marginally in the range of mine interest. If we do not consider these terms and we average on time the formula 2.13 becomes

$$\begin{aligned}I(\mathbf{q},\tau) &= 4\langle|E(\mathbf{q},t)|^2\rangle_t - 4Re[\langle E(\mathbf{q},t)E^*(\mathbf{q},t+\tau)\rangle_t] \\ &= 4I(\mathbf{q})(1 - G_E(\mathbf{q},\tau))\end{aligned} \tag{2.14}$$

If the two subtracted signals are sufficiently uncorrelated, i.e. $G_E(\mathbf{q},\tau) \longrightarrow 0$, the power spectrum is reduced to be $I(q)$, i.e. the static form factor of the sample as obtained for LALS. If instead there is correlation by subtracting the static form factor and using the relation 2.5 the formula reduces to

$$I(\mathbf{q},\tau) = I(q)G_E(q,\tau) = I(q)(\exp(-Dq^2\tau) + B(q)) \tag{2.15}$$

where $B(q)$ represents a baseline that may depend on q. For isotropic samples $I(\mathbf{q},\tau)$ can be averaged over anular rings in the q-space with the various function depending only on $q = |\mathbf{q}|$. In figures 2.6 and 2.7 there are examples of typical data acquired with NFS technique.

In figure 2.6 are reported NFS measurements analogue to LALS measurements. Starting from the speckle field obtained as a difference of two uncorrelated images, fig. 2.6a, the power spectrum can be computed, fig. 2.6b. Then with an angular average the radial profile is obtained, fig. 2.6c and is compared with theoretical prediction. The discrepancies between data and theory are due to the fact that the sample, even if is calibrated, is not monodispersed as the theoretical curve is. In figure 2.7 instead is reported NFS measurements analogue to DLS measurement. In fig. 2.7a are reported the angular average of 2D power spectrum obtained by difference of images. The different curves represent different lag time. Starting by these data, a fixed-q slice represents the scattering function. It is not the correlation function because we do not subtract the static $I(q)$. In fig. 2.7b are represented two examples of scattering functions for two different values

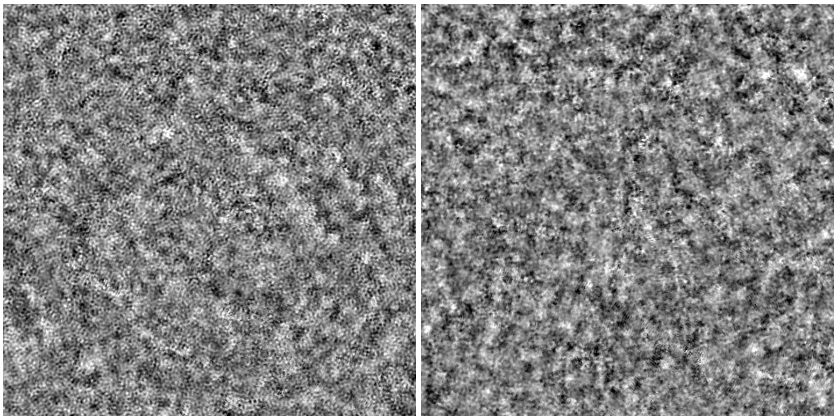

(a) Images of speckle field obtained with the difference of two acquired images.

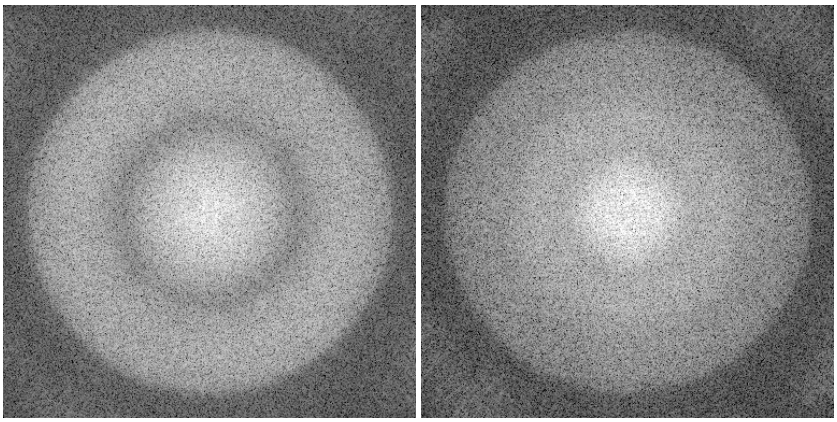

(b) Power spectrum of the speckle field.

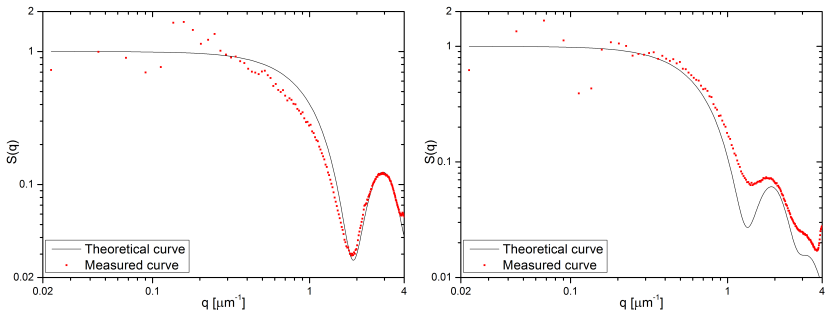

(c) Radial profile of power spectrum compared with theoretical function.

Figure 2.6: Typical measurement of NFS to obtain the static form factor of polystyrene particles suspended in water. On the left are 2.9 μm in diameter, on the right 5 μm in diameter.

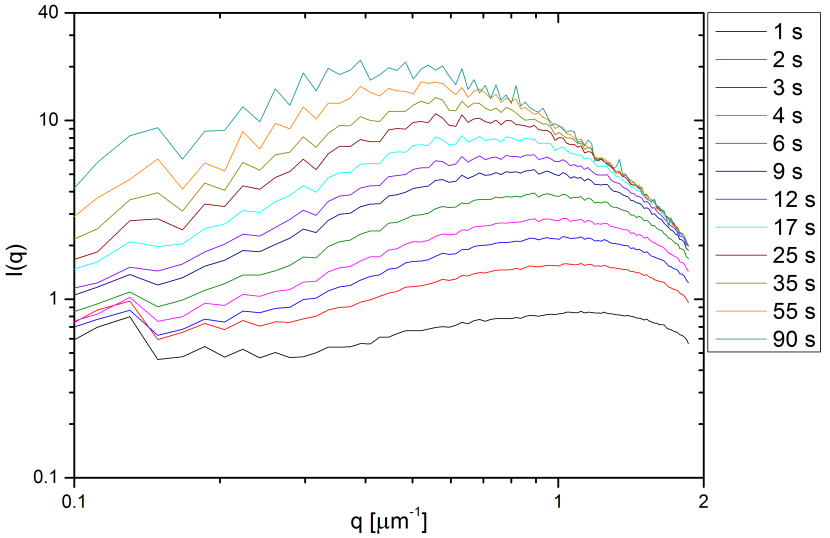

(a) Power spectra of the speckle field obtained with the difference of two acquired images at different lag times.

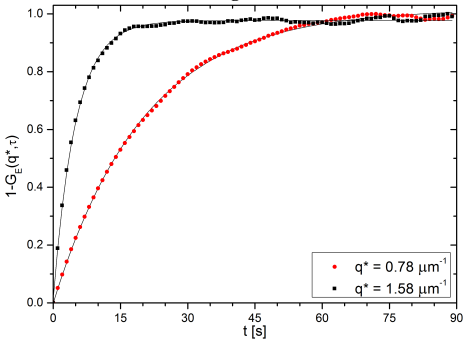

(b) Fit of the correlation function obtained as a slice of the power spectra as function of time at fixed q. The line represent the function $1 - G_E(q, \tau)$

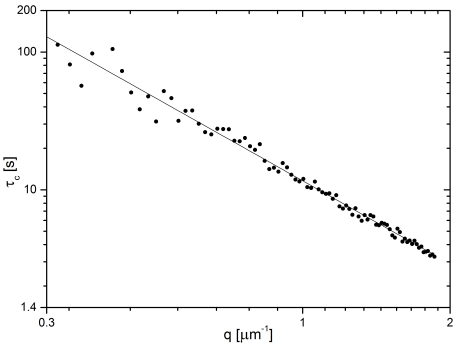

(c) Results of the fitting procedure on all the q-values (dot). The correlation time decay with the law $\tau_c = \frac{1}{Dq^2}$, represented by the black line.

Figure 2.7: Typical measurement of NFS to obtain the dynamic of the sample.

of q. The data are normalized to 1 for the asymptotic value and the fitting function is $1 - G_E(q, \tau)$. Performing this kind of analysis on all the q-vectors the fig. 2.7c is obtained. It represents the behavior of the characteristic times as a function of q, following the predicted relation $\tau_c = \frac{1}{Dq^2}$.

Chapter 3

COLLOID Experiment

In this section I show the results of the SODI-COLLOID experiment performed as a collaboration between our group of the University of Milan and Peter Schall group of UVA (Amsterdam university), founded by ESA (European Space Agency). It operated aboard the Columbus module of the International Space Station in the Microgravity Science Glovebox. This experiment was devoted to the study of colloidal aggregations induced by the critical Casimir effect in microgravity. There are many advantages of being in microgravity condition; first of all the absence of gravity prevents the particles to settle. In addition the convective motions are inhibited so the motion of the colloidal particles is purely diffusive. The absence of gravity and convective motions is very important also for the critical Casimir effect: when near the phase transition fluctuations of density arise they may increase more than what happen on ground.

At first I will briefly describe the experimental setup, the samples, the data acquisition, the procedure of data processing and some results of the static analysis. I will then focus my attention on the dynamic analysis also combined with some of the static results.

3.1 Setup

The experimental setup is shown in figure 3.1 [17], in particular in this description I refer to fig. 3.1c. A pigtailed laser diode (1) emitting at 935nm and coupled to a single mode optical fiber is sent on the collimation lens (2) to build the collimated beam that goes on the samples (4). The diffused light is collected by a long working distance 20x magnification microscope objective (5) with numerical aperture 0.3. It can be moved such that the focal plane is inside or outside the cell. The first configuration is used for imaging measurement while the second for NFS images. The images of the objective are projected onto a 10 bit CCD (7)(sensor 1024 x 1024) with a lens 200mm focal length (6). The final scattering vectors range is approximatively $0.03\mu m^{-1} < q < 1.9\mu m^{-1}$. Because of spatial limitations on the optical path of the beam two mirrors (3) were placed to deflect the light for a more compact setup. The sample cells are optical grade quartz cuvettes $25mm \times 10mm \times 2mm$ in sizes (H x D x W). They are mounted on a moving support (4) such that four different samples (plus 1 as a reference) can be moved on the optical path and studied. They were also thermally controlled with an accuracy of $\pm 0.05°C$ and stabilized within $\pm 0.005°C$.

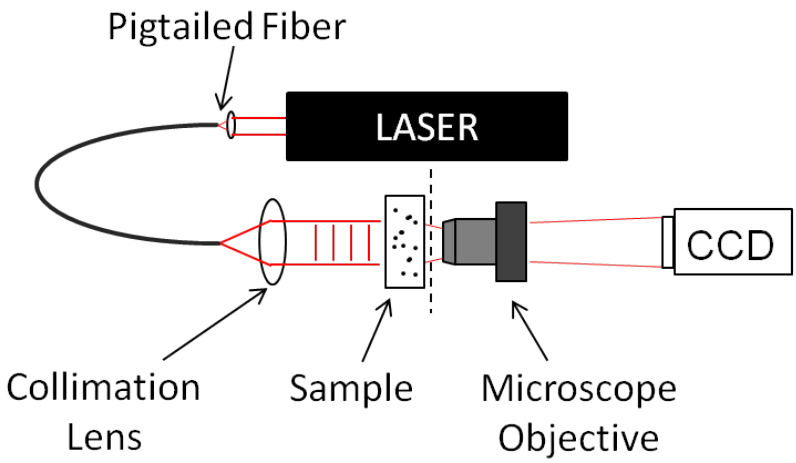

(a) Simple sketch of the setup.

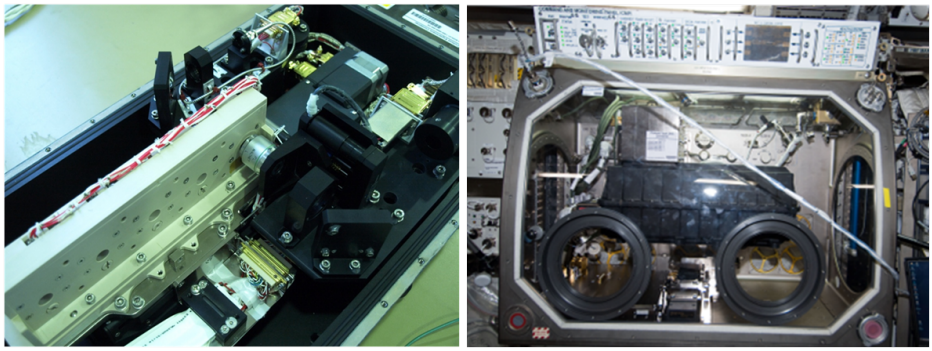

(b) Photos of the setup. The left one is on ground, the right one mounted on ISS.

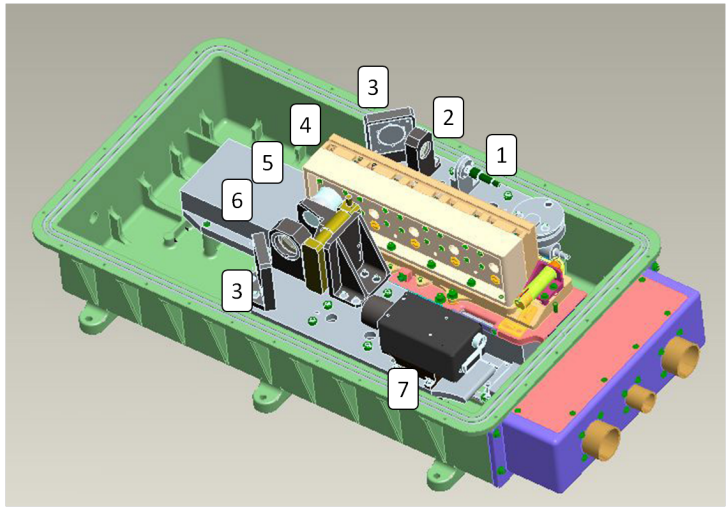

(c) Scheme of the experimental setup and layout.

Figure 3.1: COLLOID experimental setup.

3.1.1 Samples

The samples are colloidal particles dispersed in a solution that exhibits a phase separation. The chosen solvent is a binary mixture of 3-methyl pyridine (3MP) and water. The phase diagram of a similar solution is shown in fig. 3.2. Four different cells were

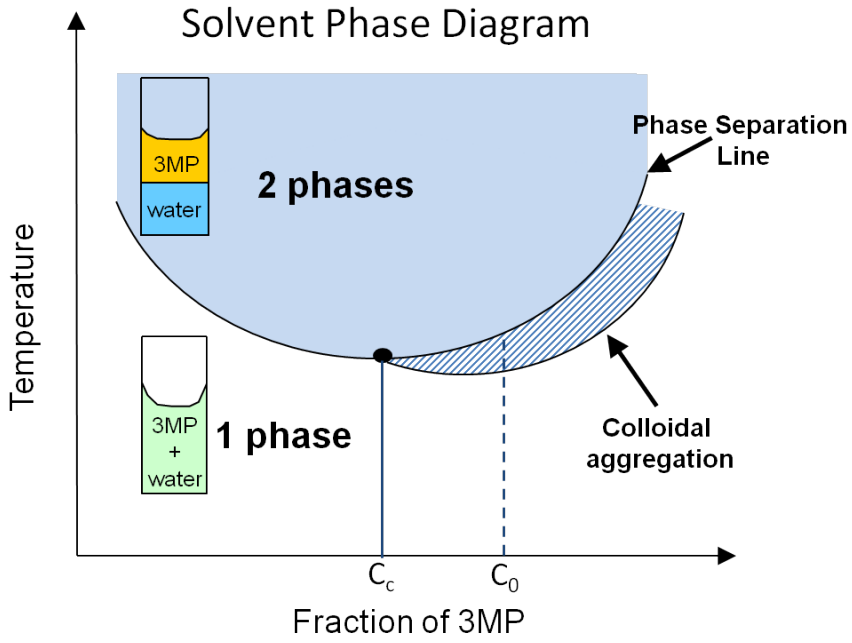

Figure 3.2: Simplified phase diagram of the binary solution of 3MP and water as function of the 3MP concentration. The C_0 dashed line represent the concentration of COLLOID experiment

prepared with mass fraction of 3MP around 0.37 with respect to the mass of the total solution. Some heavy water in spite of water was added to decrease the temperature of the phase separation T_c. The mass fraction of D_2O in respect of H_2O is about 0.62 in all the cells. Also $NaCl$ salt was added to the solutions: it changes the phase separation temperature, the aggregation temperature T_a and the difference between T_c and T_a. In table 3.1 is reported a summary of the features of the different cells. In these different

Cell number	$3MP$ [g]	H_2O [g]	D_2O [g]	$NaCl$ [mmol/L]	T_a (2010) [°C]	T_a (2011) [°C]
1	5.9385	6.1747	3.1134	0.31	46.0	44.0
2	5.8821	6.2566	3.0843	0.79	43.6	41.8
3	5.8614	6.1524	3.0183	1.51	39.6	39.4
4	5.8538	6.1530	3.0520	2.70	35.8	35.4

Table 3.1: Main features of the cell used in the COLLOID experiment. The two different temperature of aggregation are relative to the two different run of data acquisition.

"binary" solutions were suspended charge-stabilized fluorinated latex particles $200nm$ in radius with a volume fraction of $\approx 10^{-4}$. The density of the particles was 1.6 g/mL and their refractive index was $n_p = 1.37$. The refractive index of binary solution is assumed to be 1.40, so because of index matching the Van der Waals interactions are negligible in respect of other forces (electrostatic and Casimir).

3.1.2 Data acquisition

A CCD with a sensor of 1024 x 1024 pixels and a dynamic range of 10 bit registered the images. To reduce the amount of data to store, the images were binned and reduced to a dimension of 512 x 512. Because of the magnification and of the binning procedure the effective dimension of the pixel was $0.33\mu m$. In appendix A there is a description of the calibration procedure. For each of the four cells different runs of acquisition were performed at different temperatures, from the T_a to $T_a + 0.4$ with a step of $0.1°C$. At T_a, $T_a + 0.2$ and $T_a + 0.4$ were performed four different runs of acquisition, while for $T_a + 0.1$ and $T_a + 0.3$ only two runs. From now on I will refer to this different runs as waves. For every wave groups of 100 images were acquired at a frame rate of $1fps$; every group is called set. Between the acquisition of two subsequent sets the microscope objective was moved and one image inside the sample was taken. To allow the system to complete this procedure, there was a time lag of 27 seconds between two subsequent sets. The number of sets acquired is 30, with a global acquisition time of more than 1 hour ($\sim 3800s$). After each measurements the sample was brought down in temperature under the T_a to destroy the aggregates. This is a very useful tool to perform critical Casimir aggregation. In fact it is a reversible process just by controlling the temperature. However to be sure of getting back in the starting conditions for all different measurements, i.e. no aggregates and all monomers resuspended, the sample was stirred for at least three hours before starting a new measurement.

3.1.3 Data processing

The procedure for the images processing has been done with LabVIEW. A couple of images are opened, than each images is normalized at first by its average intensity to avoid as much as possible difference in mean intensity between different images. Then the two images are subtracted and divided by the sum of them, in formula

$$d(x, y; \tau) = \frac{I(x, y; t) - I(x, y; t + \tau)}{I(x, y; t) + I(x, y; t + \tau)} \tag{3.1}$$

where τ represents the time distance between the two images. The subtraction allows to eliminate the static background while the ratio is computed to have the intensity as much homogeneous as possible. Then the 2-Dimension power spectrum of each difference is computed and averaged on all the couples of images with the same lag-time within the same set:

$$J(q_x, q_y; \tau) = \langle |\mathcal{F}(d(x, y; \tau))|^2 \rangle_i. \tag{3.2}$$

The azimuthal average is performed, and then it is normalized for the transfer function $T(q)$ of the system (see appendix A) obtaining

$$J(q; \tau) = \frac{\langle J(q_x, q_y; \tau) \rangle_\theta}{T(q)}. \tag{3.3}$$

This is the very general procedure that may slightly change depending on which kind of analysis is performed. In performing static analysis, i.e. measuring the static form

factor, the microgravity condition and the increasing size of the aggregates make the dynamic, and the decorrelation, very slow. Because for this analysis uncorrelated images are needed but within the same set it is not possible to have this condition. To overcome this problem an initial set where the particles signal is not strong is considered and the average of those images is computed. It corresponds to the measurement of static optical background. Then instead of considering two different images in eq. 3.1 with the double frame approach, the background and an image are considered. Then the procedure of analysis is the same as before. Instead, in performing dynamic measurements the procedure is the double frame analysis and the averaged power spectrum can be computed for all the lag times available inside the same set. Obviously the number of averaged spectra decreases if the lag time increases. To have always a good statistic average at least 20 power spectra are considered for a maximum lag-time of 80 s.

3.2 Variance and Kurtosis

A simple kind of analysis is a first order statistic analysis based on the different momenta of the scattered signal. In particular I focus on the variance of the images (second momentum) and on the kurtosis (linked to fourth momentum). To consider just the scattered signal the variance is calculated on the difference of the images, as defined in eq. 3.1, for a fixed lag time (20 seconds). The presence of the normalization factor allows to be independent on the mean intensity that can change from different images depending on the stray light. Because of this reason instead of the variance it will be considered the normalized variance of the i-th image (NVI).

The typical behavior of the NVI is shown in fig. 3.3 and reflects the growth of the aggregates. At the beginning the particles are just the monomers and the scattered signal is too low to be detected. The NVI assumes a certain value due to other disturbances. During aggregation there are two effects that are relevant for the intensity of the scattering signal: the first is the increase of the scattering cross section. The second is the decrease of the number of particles that diffuse light. When the aggregation starts the signal becomes relevant and the NVI starts to increase. It means that the growth in the scattering cross section is stronger compared to the decrease of the number of aggregates. At a certain point this two effects reach an equilibrium condition such that the NVI doesn't vary too much. The part in which the NVI increases can be approximated as a linear regime and the starting time of aggregation can be found. By a linear extrapolation of this regime, the intercept with the time axis is assumed to be the starting time of the aggregation t_0. A reduced time can be defined as

$$t_r = \frac{t - t_0}{t_s} \tag{3.4}$$

where $t_s = \frac{3\eta}{8k_B T N_0}$, η is the viscosity of the liquid and N_0 is the concentration of particles.

With the same differences of images used to compute the NVI, also the kurtosis is calculated. It depends on the fourth statistical moment and is defined as

$$\kappa = \frac{m_4}{m_2} - 3 \tag{3.5}$$

where m_i is the i-th moment. This index reveals how the considered statistical sample is different from a Gaussian one. If the kurtosis is 0 the sample has a normal distribution and is called mesokurtic or mesokurtotic; if it is greater than 0 the statistical sample has a narrower peak than a Gaussian distribution and is called leptokurtic or leptokurtotic;

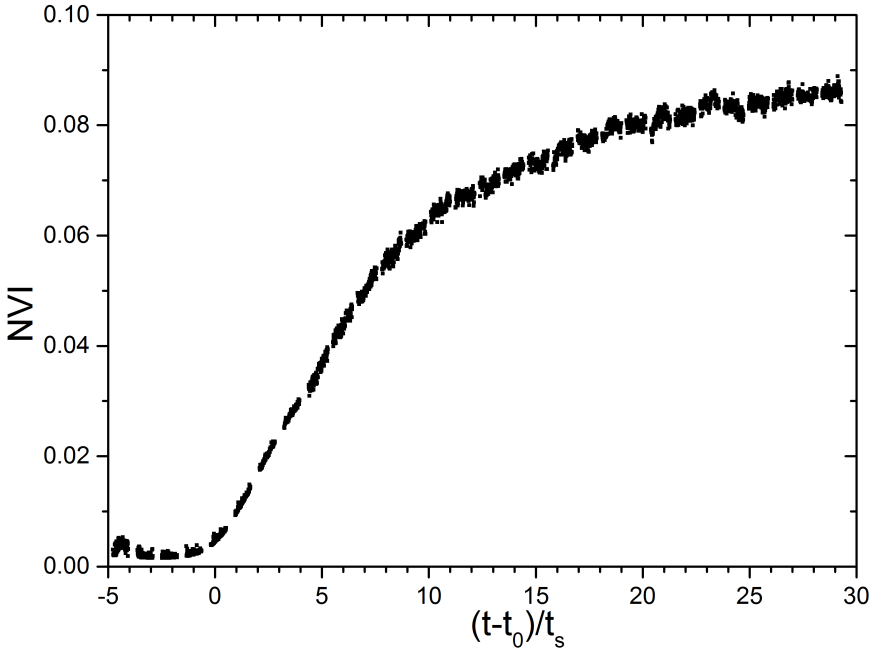

Figure 3.3: NVI data for the sample of Cell 1 at $T_{\rm agg}$.

if lower than 0 the distribution is broader than a Gaussian, and is called platikurtic or platikurtotic. In my analysis I directly use the ratio between the moments without subtracting 3. This previous considerations hold considering 3 as critical value instead of zero.

In fig. 3.4 example data for the kurtosis can be found. Also in this plot three different regions can be found. The first one is for $t_r < 0$ where the kurtosis varies wildly. At these early times, subcritical nuclei may form and evaporate on the time scale of observation generating those large fluctuations. For $0 < t_r \lesssim 8$ the kurtosis value is stable and varies approaching its constant value around 3. In this region the aggregates increase in size as can be noticed also from NVI data. The final region is for $t_r > 8$ where the kurtosis is stable around 3 with little statistical oscillations. In this region the aggregates are well formed and reliable informations on the sample can be found.

The behaviors of both kurtosis and NVI are here shown just for one example of aggregation process but they are almost general and they well describe all the other aggregating process.

3.3 Static results

The results shown in this section refer to some static properties of the aggregates and of the aggregation process [23]. Those properties are found by studying the power spectrum of the images difference, as described previously. The objects that formed with colloidal aggregation are fractal aggregates with some peculiar features.

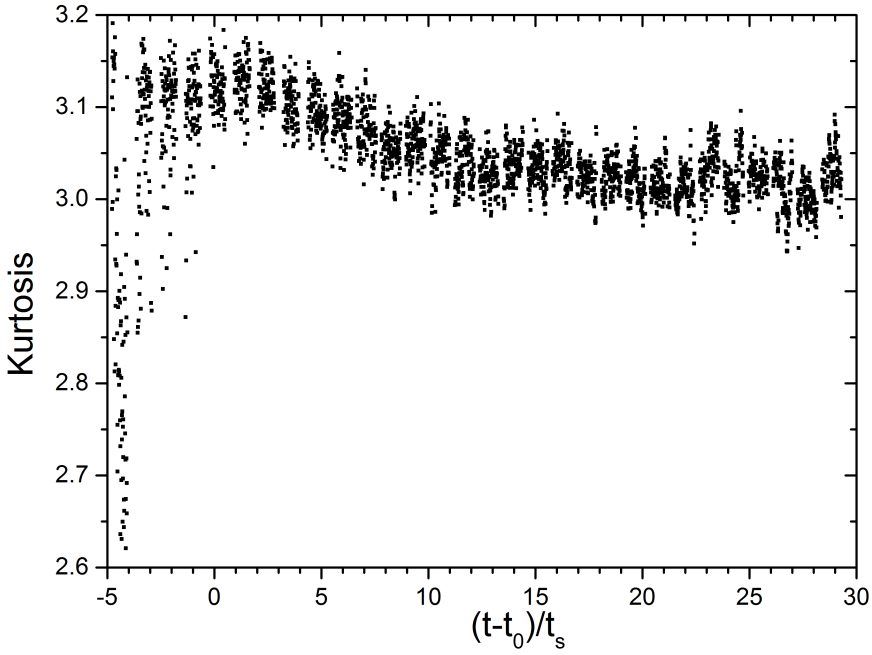

Figure 3.4: Kurtosis data for the sample of Cell 1 at T_{agg}.

3.3.1 Fractal aggregates

A fractal is a geometrical or physical structure having an irregular or fragmented shape that is repeated on different lengthscales. An index of the complexity of the structure is the fractal dimension d. The mathematical definition is connected to the number of spheres that may cover, without superposition, the fractal object. The number of the spheres N_s changes with their diameter d_s with the scaling law $N_s \sim d_s^{-d}$. The fractal dimension is defined as the exponent of the diameter to find the number of spheres to fully cover the object in the limit of $d_s \to 0$. The limiting values of fractal dimension are 1, for a linear structured object, and 3, for a 3-dimensional ordered and compact object.

The formation of fractal aggregates in a colloidal aggregating system can occur in two different limiting regimes:

- **DLCA** (or **DLA**): *Diffusion-Limited Cluster Aggregation*. The aggregation is driven by the diffusive motion of particles and has to be fast compared to the diffusive time in order to avoid other kinds of motions. The sticking probability is 1, if two particles touch they stick. The fractal aggregates that are formed have a fractal dimension of 1.8 and their size grows in time with the power law $R(t) \sim t^{1/d}$.

- **RLCA** (or **RLA**): *Reaction-Limited Cluster Aggregation*. The aggregation is driven by some different kinds of motions, like convection or settling in addition to diffusion. The sticking probability is lower than 1 so the time-scale are higher than the diffusion time. The typical fractal dimension in this regime is 2.1 and the characteristic size grows in time as $e^{\alpha t}$ where α depends on the sticking probability.

The mass of the aggregates is related to the size via the simple relation $M(r) \sim r^d$.

It is easy now to compute the correlation function for the single aggregate as $C(r) \sim r^{d-3} f(r/R_c)$, where $f(x)$ is a cutoff function which keep account for the finite size of the aggregate, represented by R_c. The gyration and the hydrodynamic radii can be found by the correlation function with the relations:

$$R_g^2 = \frac{1}{2} \frac{\int_0^\infty r^2 C(r) r^2 dr}{\int_0^\infty C(r) r^2 dr} \tag{3.6a}$$

$$R_H^{-1} = \frac{\int_0^\infty r^{-1} C(r) r^2 dr}{\int_0^\infty C(r) r^2 dr} \tag{3.6b}$$

Both radii grow with the power law $R_{g,H} \propto t^{1/d_f}$ with the proportional constant depending on the model used for the cutoff function.

Another typical property of the fractal aggregates is described in the Fourier space. In fact the static form factor can be computed as the Fourier transform of the correlation function. Usually the cutoff function is assumed to be exponential; the Fourier transform of this correlation function is approximated with the Fisher-Burford expression

$$S(q, R_g, d) = \left[1 + \frac{2}{3d} (q R_g)^2 \right]^{-d/2} \tag{3.7}$$

where q is the scattering vector, R_g is the gyration radius and d is the fractal dimension. In a scattering experiment the form factor is multiplied by the low-q intensity that is proportional to the mass of the aggregates. So by a single measurement of the power spectrum we can measure the low-q intensity I_0, the dimension of the aggregates R_g and their fractal dimension d, with a three parameters fit. A very interesting thing is that in the static form factor the dependence on the radius and on the scattering wavevector are mixed together by their product. It is possible to create a master curve depending only on the product qR_g.

3.3.2 Universality of fractal aggregates

In the COLLOID experiment thanks to microgravity the motion is perfectly diffusive, so the interesting regime is the *DLCA*. By studying the power spectra we are able to find out the informations on I_0, R_g and d as described in the previous section. The typical kind of data is the one showed in the fig. 3.5. The slope in the high-q region gives the fractal dimension, because of the asymptotic dependence q^{-d}. The low-q region describes the growth of the mass of the clusters with time. The position in which there is the change in the slope is directly related with the gyration radius R_g of the aggregates. By fitting of the data we find that the R_g changes in time with a power law, fig. 3.6, evidence of the fact that we are in the *DLCA* regime, as we expected. A very interesting thing is about the fractal dimension. Even if we are in a pure DLA condition that predicts a fractal dimension of 1.8, we find different values of fractal dimension depending on temperature, which means on the interaction strength. In table 3.2 are reported the different values of the fractal dimension, which remains constant within the experimental errors during the same measurement. They change from 1.8 to 2.5; notice that higher the temperature, i.e. the interaction strength, lower is the fractal dimension.

Even if there are differences in the features of the aggregates, the aggregation processes show some similar behavior at different temperatures. With a model independent procedure, the different form factor can be rescaled with the relation

$$S(q, q_{red}) = q_{red}^{-d} F(q/q_{red}) \tag{3.8}$$

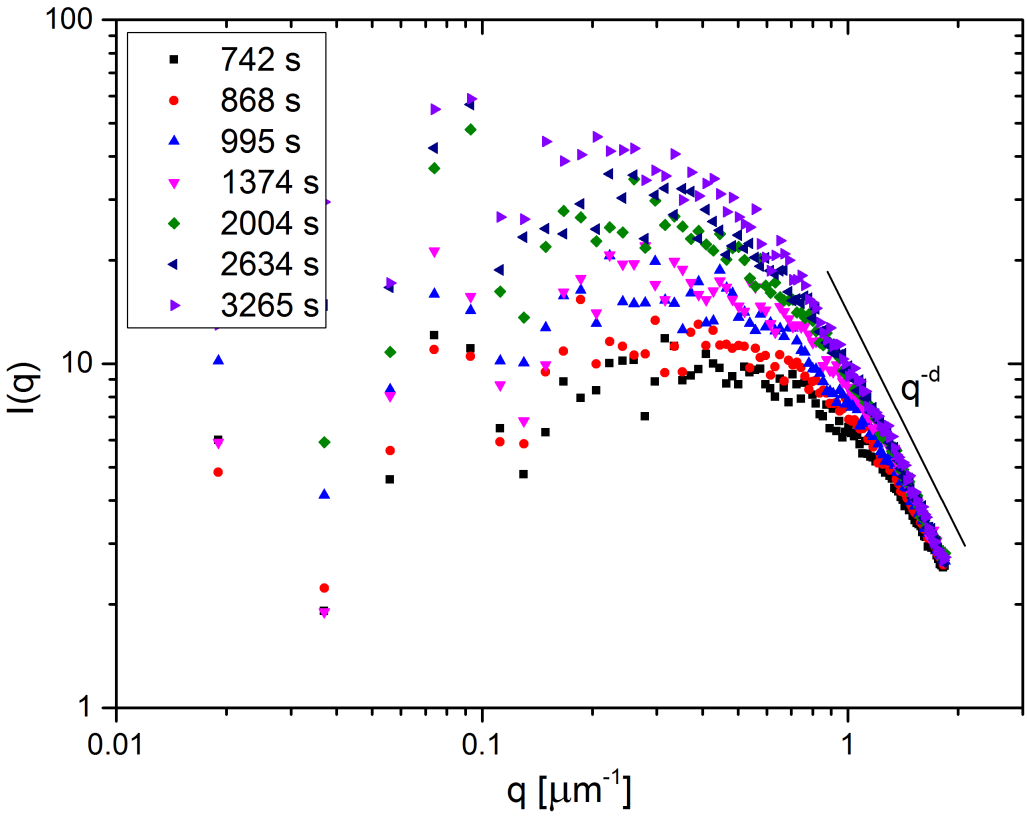

Figure 3.5: Power spectra of the sample in Cell 1 during an aggregation process at T_{agg}. The increase in time means an increase in the size of the aggregates.

Cell number	T_a d	$T_a + 0.1$ d	$T_a + 0.2$ d	$T_a + 0.3$ d	$T_a + 0.4$ d	Ground d
1	2.4	2.0	2.0	1.9	1.8	1.6
2	2.35	2.1	2.1	2.0	1.95	1.7
3	2.3	1.9	1.95	1.8	2.05	1.7
4	2.4	2.1	2.1	1.8	2.0	1.8

Table 3.2: Fractal dimensions measured at different temperatures, i.e. interaction strengths, in microgravity condition for the different cells. The last column refers to the ground measurements on the same samples.

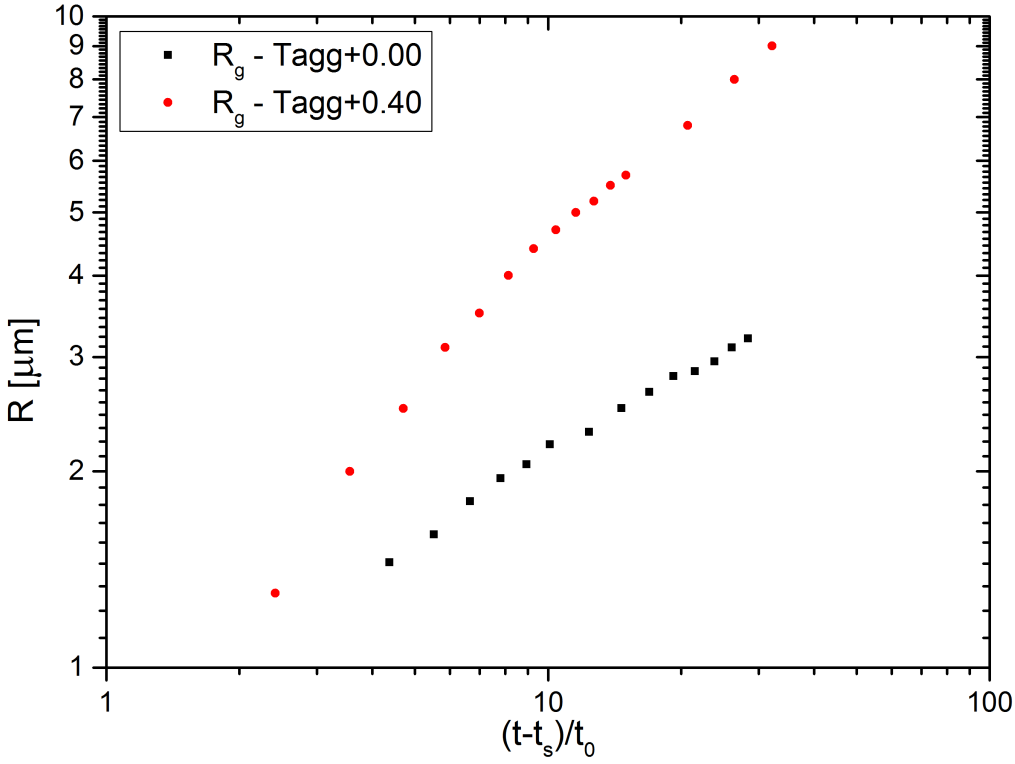

Figure 3.6: Gyration radii as function of the reduced time. The data refer to Cell 1, at T_{agg} and $T_{\text{agg}} + 0.4$.

to collapse on a master curve. This scaling procedure depends on the fractal dimension d and on a reducing scattering wavevector q_{red}. This q_{red} is directly related to the

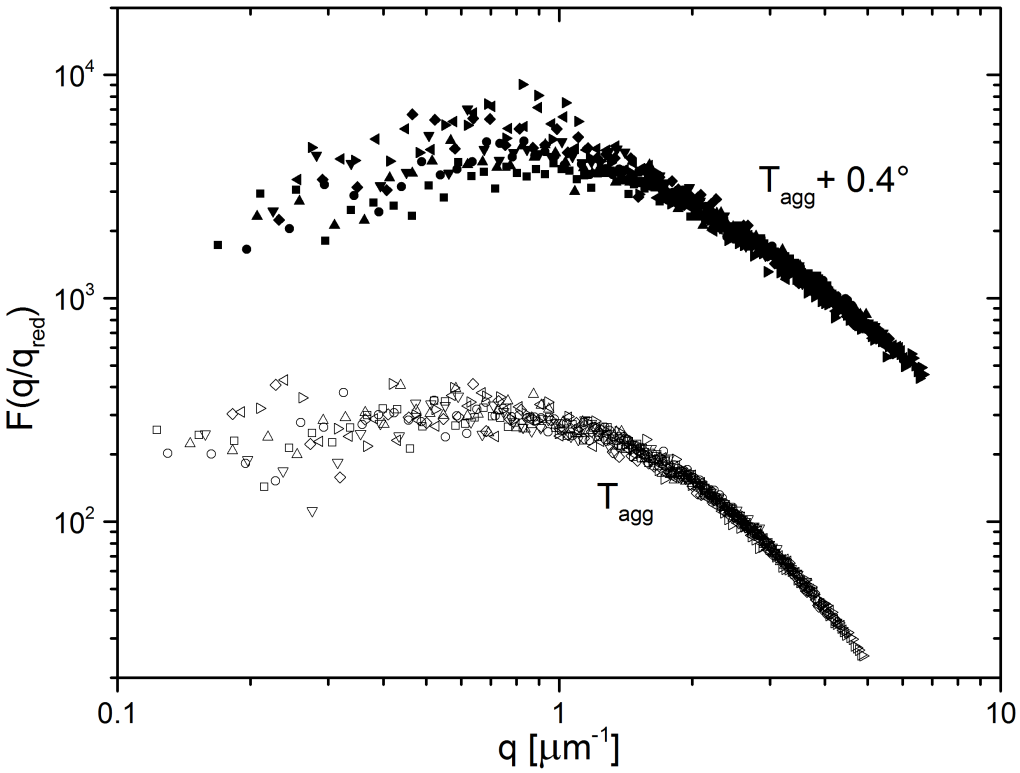

Figure 3.7: Reduced power spectra. Data are related to the acquisition on Cell 1 at T_{agg} and $T_{\text{agg}} + 0.4$. Different symbols codes different times of aggregation.

dimension of the aggregates via the relation $q_{red} = 2\pi/R_g$.

3.4 Dynamic analysis

As mentioned in the previous chapter, the study of the dynamic properties means the study of the correlation function of the signal. In particular for NFS experiment by one set of images we are able to find out the correlation functions for a wide range of q-values. The standard study of the correlation function is an exponential fitting with the formula 2.15 to find the correlation time. Even if the previous formula of the correlation function is expressed for the translational diffusion coefficient it can also be applied for the rotational diffusion changing the expression of the correlation time. For the translational diffusion the decorrelation time τ_T is related to diffusion coefficient via the relation $\tau_T = 1/Dq^2$. For rotational diffusion τ_R is related to the rotational diffusion coefficient θ as $\tau_R = 1/6\Theta$, where $\Theta = \frac{k_B T}{8\pi\eta R_H^3}$. In respect of translational diffusion, the rotational characteristic time does not depend on the scattering wavevector, and it is constant for all the angles. In figure 3.8 are represented the correlation times both for rotational and translational diffusion. In usual experiments, for example a DLS measurement at 90 de-

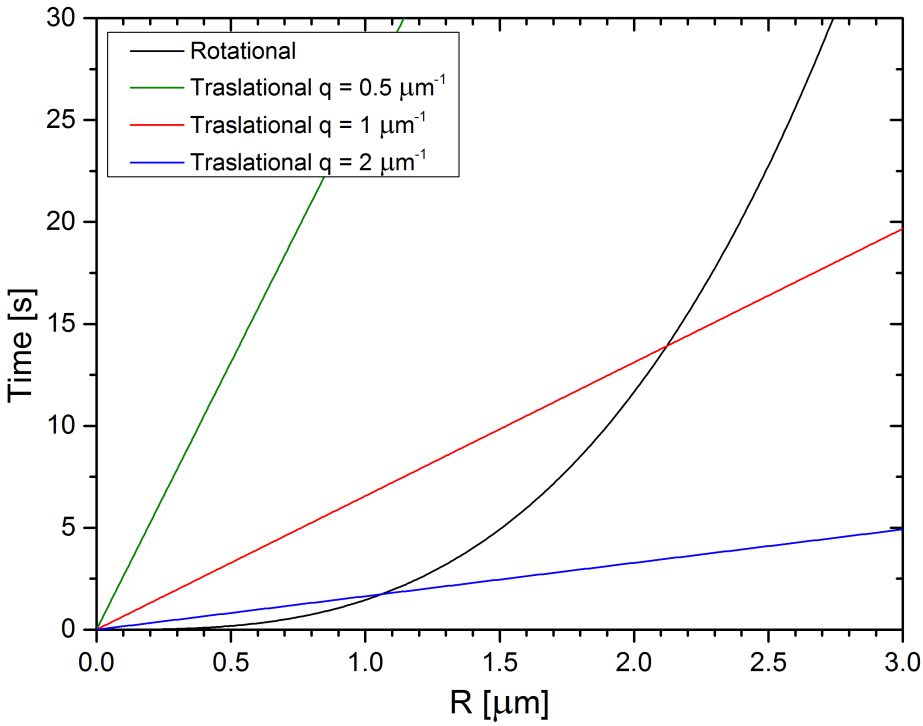

Figure 3.8: Characteristic diffusive rotational and translational time. The rotational time is independent on q and depends solely on the radius. Instead the translational one depends on both the radius and q. Here is represented just for three different values of scattering vector q.

grees, the two correlation times are quite different, and the measured one is the shortest one. Obviously to have signal from rotational diffusion the particles must have some optical anisotropy or some particular structure depending on orientation, for example they could be rod-like particles.

3.4.1 Master Curves

The peculiar structure of fractal aggregates is such that also the rotational diffusion is important [24, 25]. In the dimensional range of interest for COLLOID experiment the correlation times are very similar, so we have to keep account also for the rotational diffusion. To do it we define an effective diffusion coefficient D_{eff} that keep account both for rotation and translation [26]. This new coefficient is related to the diffusive one via the relation

$$\frac{D_{\text{eff}}}{D} = 1 + \frac{1}{2\beta^2}\left(1 + \frac{3\partial \ln S(qR_g)}{\partial (qR_g)^2}\right) \tag{3.9}$$

where β is the ratio R_H/R_g and $S(qR_g)$ is the form factor. Using for it the Fisher-Burford expression 3.7, the previous equation becomes

$$\frac{D_{\text{eff}}}{D} = 1 + \frac{1}{2\beta^2}\frac{2(qR_g)^2}{3d + 2(qR_g)^2}. \tag{3.10}$$

A very interesting thing is that, as for the static form factor, the dependence on the radius and on the scattering wavevector are mixed together by their product: it is possible to create a master curve depending solely on the product qR_g.

Using this effective coefficient the procedure of data analysis remains the same as before. The correlation function is still fitted with an exponential decaying function but the diffusion coefficient is substituted with D_{eff}. By the correlation time, given by $\tau = 1/D_{\text{eff}}q^2$, we are able to find the dependence of D_{eff} on q. By a fit of the data with the exponential decaying function combined with eq. 3.10 and with the information obtained from the static analysis, we obtain the only free parameter R_H.

3.4.2 Polydispersity

The aggregation process leads to the formation of aggregates that are not all of the same sizes. They have a distribution in size or mass that has to be considered. The main problem when the polydispersity must be considered is which shape of the distribution has to be used. For a DLCA process this shape $N(M)$ is given by numerical simulation of aggregation and is expressed by the exponential form

$$N(M) = \frac{N_T}{\overline{M}}\left(1 - \frac{1}{\overline{M}}\right)^{M-1} \tag{3.11}$$

where M represents the numerical mass of the aggregates, N_T the total number of clusters and $\overline{M}$ the average cluster numerical mass that is defined by $\overline{M} = \sum MN(M)/N_T$. From this point on, the mass M does not refer to the real mass, but the numerical mass that represents the number of monomers that compose the aggregates. It is related to the radius of the cluster via the relation $M = (R/a)^d$ where a is the radius of the monomer.

To keep account for polydispersity in our analysis we define a mean effective diffusion coefficient. The equation for $\overline{D}_{\text{eff}}$ is

$$\overline{D}_{\text{eff}} = \frac{\sum_M N(M)M^2 S(qR_g)D_{\text{eff}}}{\sum_M N(M)M^2 S(qR_g)} \tag{3.12}$$

Even if not written explicitly $\overline{D}_{\text{eff}}$ depends on the average mass (or radius) and on the scattering wavevector. Again it depends only on their product allowing us to create a master curve describing all the aggregation process.

3.5 Experimental results

The procedure of data analysis is already explained in section 3.1.3. Images in the same sets are considered, i.e. 100 images acquired at 1fps, to calculate the difference as in eq. 3.1. The power spectra are calculated and averaged for every couples of images with the same lag time. To have a good number of spectra to average, the time lags used go from 1s up to 50s. The final result of this procedure is a set of 50 power spectrum $I(q;\tau)$, or intermediate scattering function, as shown in fig. 3.9. For every value of q, the

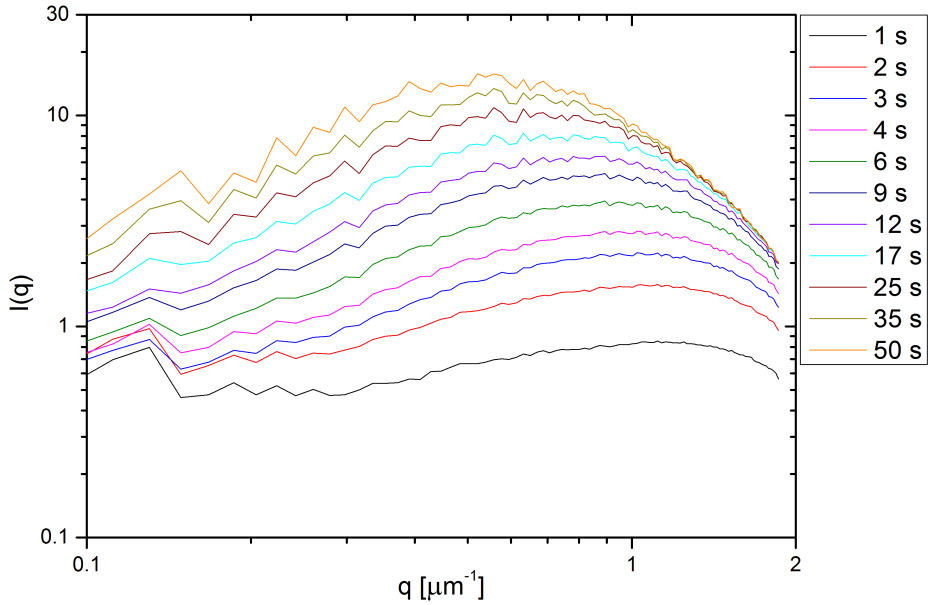

Figure 3.9: Power spectra computed to perform dynamic analysis. The time lag goes up to 50 s, but here in the figure there are only some of them to make the image more clear.

data are fitted with a decaying exponential function as a function of time. Because the measured power spectrum is the one in eq. 2.14 it is necessary to know the static form factor to measure the correlation function. But if we use the measured static form factor we add noise to the data. The best solution is to not consider the static form factor and to fit directly the temporal evolution of the spectra. The fitting function will not be the decaying exponential in eq. 2.15, but it will be the scattering function

$$S(q^*,\tau) = A - B\exp(-D_{\text{eff}}{q^*}^2\tau)) \tag{3.13}$$

where A and B are free parameters depending on the normalization of the data. The third parameter of the fit is D_{eff}. The superscript * is to remember that the values of q in the fitting is a known fixed parameter. By fitting with this function the data for all different q-values the D_{eff} as function of q is found.

Those data can now be compared with eq. 3.10 [18]. The knowledge of R_g and d from static analysis leave to the fit only one free parameter, that is R_H or β. The dependence on R_H is also in the diffusion coefficient that divides the data. So changing this parameter means that not only the fitting function changes but also the data. To simplify the procedure of data analysis we rewrite equation 3.10 in the following form:

$$2\beta^2 \left(\frac{D_{\text{eff}}}{D} - 1 \right) = \frac{2(qR_g)^2}{3d + 2(qR_g)^2}. \tag{3.14}$$

The right side of equation depends all on known parameters, while the unknown parameters (R_H) is on the left side. This procedure differs from a standard fitting procedure: in fact usually the data are fixed and the parameters change the position of the fitting function. Here instead the fitting curve (right side of equation) is fixed while the fitting parameter changes the data (left side of equation). As already mentioned the polydispersity has to be considered. The equation 3.12 can be rewritten using eq. 3.14 because β and obviously also 1 are constant in the sum. The fitting function becomes

$$2\beta^2 \left(\frac{D_{\text{eff}}}{D} - 1 \right) = \frac{\sum_M N(M) M^2 S(qR_g) \frac{2(qR_g)^2}{3d+2(qR_g)^2}}{\sum_M N(M) M^2 S(qR_g)}. \tag{3.15}$$

Even if is not written explicitly, R_g depends on the mass via the relation $R_g = a \sqrt[d]{M}$.

The fit with this function is performed on the data acquired for the three different cells at the different temperatures. Examples of the fitting procedure are shown in the figure 3.10. The fits are accurate on the entire range of qR_g in all different runs of acquisitions. In particular in the later stages of the aggregation the data can be fitted with a value of β that is almost constant, while in the first part it slightly changes. This different behavior can also be connected with the behavior of the kurtosis, as already mentioned in section 3.2. In the early stages of aggregation the aggregates have already a fractal structure, but they are still rearranging themselves to have a defined internal structure that can be seen in the later stages. For the data reported in the figure 3.10a the region in which the aggregates are still rearranging and β is changing is found for values of reduced time $0 < t_r < 8$. Instead for $t_r > 8$ the aggregates are well formed and the value of β is constant. The values of β allow also to know the hydrodynamic radii and compare them with the gyration radii. Also the hydrodynamic radii show that the growth in time of the aggregates has a power law dependence $t^{1/d}$, as expected for a DLCA process.

To have a better understanding on the internal structure the values of β, i.e. the ratio R_H/R_g, as a function of the fractal dimension are considered. The advantage of being in microgravity is that the fractal dimension assumes different values in the range from 1.8 to 2.5 for pure DLA aggregations. It allows a systematic study of β as function of d. The data of the studied cells are reported in figure 3.11. The different colors codes different values of temperature; in detail *black* points are for $\Delta T = T - T_{agg} = 0$, *red* for $\Delta T = 0.1$, *blue* for $\Delta T = 0.2$, *green* for $\Delta T = 0.3$ and *violet* for $\Delta T = 0.4$. The different symbols indicate different Debye screening lengths corresponding to different salt concentrations: *squares* are for $\lambda_D = 14nm$ (0.31 mmol/L), *circles* for $\lambda_D = 6.4nm$ (1.5 mmol/L) and *triangles* for $\lambda_D = 4.8nm$ (2.7 mmol/L). A simple idea on how of the Debye screening length may influence the aggregation process is the following: without considering the Van der Waals interactions, the shape of the potential depends only on the electrostatic and Casimir interactions. In particular the depth of the potential well is a function of the ratio of the correlation length ξ and the Debye screening length λ_D. At T_{agg} they are almost equal. Remembering that the correlation length obeys to $\xi = \xi_0 (T_c - T)^{-\varepsilon}$ (eq.

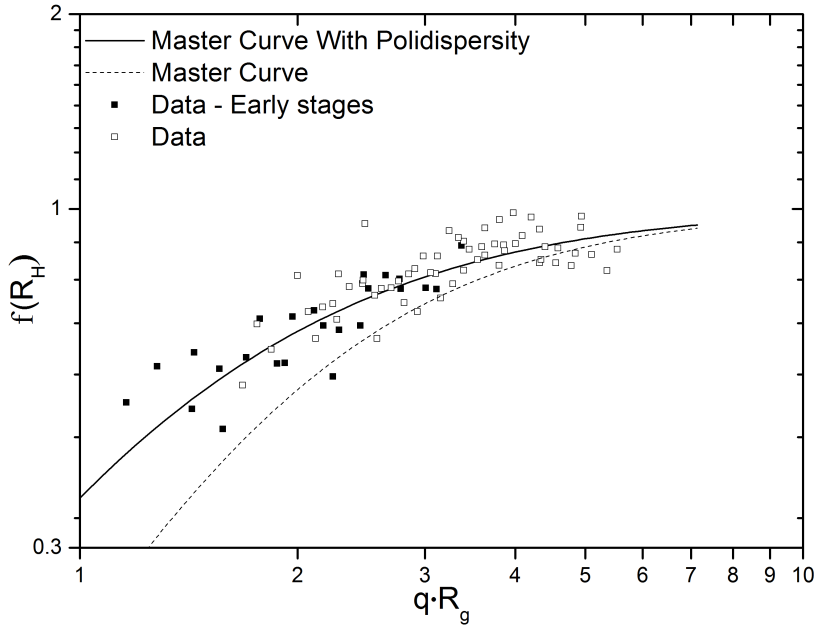

(a) Fit of the data of Cell 1 at T_{agg}. The black point represent the data for early stages, i.e. $t_r < 8$.

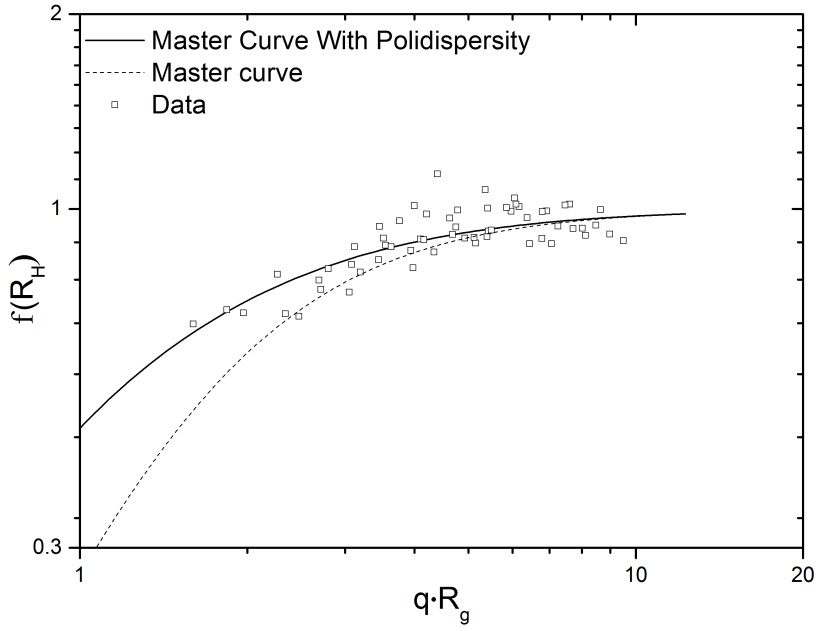

(b) Fit of the data of Cell 1 at $T_{\text{agg}} + 0.4$.

Figure 3.10: Example of the fit of the data with the master curve. The function f(R_H) represent the left (data) or the right (fit) side of eq. 3.15. The line represent the polydisperse master curve used for the fit, the dashed one is the master curve obtained without consider the effect of polydispersity.

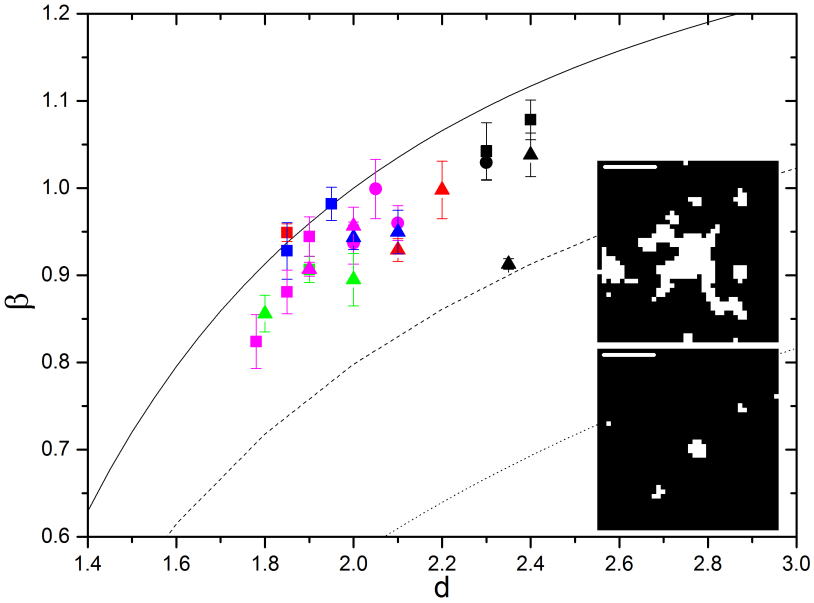

Figure 3.11: Values of β as function of the fractal dimension d. Different colors encodes the temperature at which aggregation occur: *black* stays for $\Delta T = 0.0$, *red* for 0.1, *blue* 0.2, *green* 0.3 and *violet* 0.4. Different symbols correspond to different salt concentration, *squares* for $\lambda_D = 14nm$, *circles* for $\lambda_D = 6.4nm$ and *triangles* $\lambda_D = 4.8nm$. The curves represent different cutoff function in the correlation function of the aggregates: the *line* is the unit-step cutoff, *dashed line* the gaussian and the *dotted* the exponential. Finally the two inset figure represent an holographic reconstruction of the aggregates, the lower at T_{agg} and the upper at $T_{\text{agg}} + 0.4$.

1.31) and supposing that λ_D doesn't change with temperature, their ratio can be written as

$$\begin{aligned} \xi/\lambda_D &= [(T_c - T)/(T_c - T_{agg})]^{-\varepsilon} \\ &= \left[1 - \frac{\Delta T}{T_c - T_{agg}}\right]^{-\varepsilon} \end{aligned} \tag{3.16}$$

The difference $T_c - T_{agg}$ defines a scale for the temperature step and depends on the Debye screening length. If λ_D increases also the this difference increases. For a fixed temperature the sample that should have the deepest potential, i.e. the strongest interaction, is the one with the shortest screening length. Instead for a fixed λ_D, if the temperature increase the interaction becomes stronger. We observe that deeper is the potential, lower is the fractal dimension.

In fig. 3.11 are also plotted the different curves calculated for the different cutoff function in the definition of the correlation function for the aggregates (see section 3.3.1) [22]. The calculation for the expression of β are in app. B. The three lines represent from bottom to top the exponential, the gaussian and the unit step cutoff. Even if the interaction strengths are different and also the fractal dimension changes, the aggregates exhibit a compact internal structure. This independence on the interacting potential indicates a certain degree of universality in the mass distribution. To have an idea of the density distribution two holographic reconstruction of the aggregates both in the final stages are shown as inset in the fig. 3.11. The upper one shows an aggregates formed at $T = T_{agg} + 0.4$, that means highest attraction. The lower one instead shows an aggregates formed at $T = T_{agg}$, lower attraction. The irregular but compact structure of the aggregates formed at higher attractive interaction strength is clearly observable, as well as the larger size due to the higher growth rate.

3.6 Conclusions

With the COLLOID experiment the aggregation induced by the critical Casimir effect was studied. The different samples and the different temperatures at which the aggregation was performed allow a sistematic study of this effect and the universality in colloidal aggregation is again underlined. A first example of it is the collapsing of the power spectra of the samples, i.e. the form factor of the aggregates [23]. Also the study of first order statistic like normalized variance and kurtosis show some general features that reply in all aggregation processes. The microgravity condition allows also to perform dynamic analysis and find some known features that are usually observed with aggregates of smaller monomers [27]. The possibility of creating a master curve for the dynamic data represents once more the universality in colloidal aggregations [26]. Thanks to the peculiar condition of this experiment also different values of fractal dimension in DLA condition have been studied. The fractal dimension changes in dependence of some samples parameters during different run of acquisition. It assumes values from 1.8 to 2.5 depending on the temperature, i.e. on the interaction strength. The possibility of study data with different fractal dimensions allows to have a deeper insight in the internal structure of the aggregates. In fact by studying the behavior of β as a function of fractal dimension I find that the aggregates are more compact than what is usually assumed. The usual assumption for fractal aggregates is that the cutoff function in the density of the single aggregate is represented by an exponential decaying function. However the COLLOID results show that for all the fractal dimensions

the data show an internal structure not described by an exponential cutoff function but something between a gaussian and a unit-step cutoff function [18].

There are still some things that are under investigation. For example, the different behavior in early and later stages of aggregation is shown in different parameters that are studied, i.e. the kurtosis and the radii. We are currently trying to understand why there is this different behavior and if it has some general features in the different sets of data. There are also some data relative to a second run of experiment that are performed at lower temperature than the aggregation temperature (T_{agg} minus 0.1 or 0.2 degrees). Also measurements at the phase separation temperature were performed. Both these data have not been studied yet. The study of those data may give very interesting information, especially for the one at phase separation, in which is monitored a non equilibrium system approaching the phase separation in microgravity condition.

Chapter 4

Salt Induced Aggregations

In order to compare the COLLOID results to ground based processes, I performed aggregation measurements on ground. In parallel with the space experiment specific ground measurements were realized with samples identical to those sent to the ISS. However, those measurements allowed to recover static properties only. Dynamics was prevented because of convective motions inside the cells. The temperature control of the samples, required for critical Casimir effect, naturally generates thermal gradients that combined with gravity cause convective motions. In order to avoid this drawback in the measurement described below the aggregation was induced by adding salt to the colloidal solution instead of using critical Casimir effect. The working temperature was just the room temperature. The peculiarity of the system required a different way to analyze data with respect to the COLLOID experiment. In addition to NFS, these samples were also characterized through a different technique, named single particle extinction and scattering (SPES), which provides the single particles properties. In this section I will show the results obtained with this two different methods. In particular, the first part reports the results obtained from the SPES measurements; the second part shows the results obtained with NFS, explaining a different way to analyze the data.

4.1 Samples

I have studied the same samples with the two methods. They are suspensions of polystyrene particles diluted in water. The aggregation process starts when salt is added to the solution [28]. In detail, the sample was composed by polystyrene calibrated sphere $100nm$ in diameter suspended in distilled and filtered water. This kind of samples were prepared with a concentration of $5 \cdot 10^{10}$ particles/mL. In another beaker the solution with the salt is prepared. The salt was $MgCl_2$ diluted in water to reach the concentration of $60mM$. The final sample was obtained with a combination of this two different solutions mixed with some more water. In this way both the concentration of salt and particles can be easily controlled just by changing the mixed quantity. The receipt we used to prepare the samples for the measurement is: 3 parts of water and particles, 2 of $60mM$ salt and 1 of water. With these dilutions the final sample has a concentration of particles that is half of the starting one, i.e. $2.5 \cdot 10^{10}$ particles/mL and a salt concentration of $18mM$. The sequence of mixing is the following: first the solution with particles and water; the salt is added making it flow along the wall of the beaker to avoid turbulence that may generate sudden strong aggregation. The sample is gently mixed to make the sample as uniform as possible and then is ready to be measured. All these procedures

are done directly in the container where the aggregation has to occur. For NFS measurement is in the cuvette, typically $2mm$ in optical path. For SPES measurements the situation is a little bit different. This kind of measurements is based on a single particles analysis; it requires a very diluted sample that is out of the conditions of aggregation. So the aggregation process was performed in a beaker, while for NFS measurements were performed directly in the cuvette. After the desired time a small portion of the aggregating sample was extracted and diluted. In this way the concentration decreases and the aggregation is stopped. Therefore even if the measurement takes some time, the sample doesn't change its properties.

4.2 Single Particle Extinction and Scattering: SPES

The single particle extinction and scattering (SPES) is a novel technique that allows to study a sample by characterizing single particles [29, 30]. SPES measures the forward scattered fields $S(0)$ generated by single particles flowing through a focused laser beam. The advantages of this technique in respect the other traditional techniques is to access at two independent optical parameters, the extinction cross section σ_{ext} and the optical thickness [31]. The former is measured just from the attenuation of the laser beam, the latter from the interference between the transmitted beam and the scattered field. Ultimately, SPES measures the real and the imaginary parts of S(0). Their combined knowledge brings informations on some features of the particles, as dimension, shape and refractive index. Even if these parameters are analytically known only for spherical homogeneous not-absorbing particles, some information can be found for any particle.

4.2.1 Modeling single aggregates

At variance with traditional light scattering methods, to interpret the measurements of aggregating samples obtained with SPES a model for the interpretation of the fields scattered by single aggregates is needed [32]. This model is obtained by using some simple relations for fractal aggregates and the average refractive index n_{av}. Let's consider a system with permittivity ϵ_m with some inclusions composed by a different material with permittivity ϵ. If both medium and material are not absorbing, as in our condition, the refractive indexes are $n_0^2 = \epsilon_m$ for the medium and $n^2 = \epsilon$ for the material. The average refractive index is obtained through the modified Maxwell-Garnett model [33]

$$n_{av}^2 = n_0^2 \left(1 + \frac{3f\frac{m^2-1}{m^2+2}}{1 - f\frac{m^2-1}{m^2+2}} \right) \tag{4.1}$$

where $m = n/n_0$ and f is the volume fraction of the inclusions. Since we can assume $m \sim 1$ (for polystyrene in water is 1.12) the previous relation is simplified to

$$m_{av} - 1 \sim f(m-1) \tag{4.2}$$

where $m_{av} = n_{av}/n_0$.

Basing on the fundamental properties of fractal aggregates, the volume fraction of the inclusions f can be simply calculated as follows. Let's consider an aggregate with gyration radius R_g; the volume occupied by the aggregates is the volume of a sphere V with radius R_g. But the aggregate is not a fully compact object, and only a part of this volume is occupied by the monomers. If the aggregate is composed by particles of

radius a, the volume of material is

$$V_A = \frac{4}{3}\pi a^3 \left(\frac{R_g}{a}\right)^d \tag{4.3}$$

where d is the fractal dimension. It represents the volume of a monomer particle multiplied by the number of monomers that compose the aggregate. The volume fraction of the inclusions is given by

$$f = \frac{V_A}{V} = \left(\frac{R_g}{a}\right)^{d-3} \tag{4.4}$$

that can also be considered as the numerical mass of the aggregates. Combining this result with eq. 4.2, the m_{av} is given by

$$m_{av} - 1 = \left(\frac{R_g}{a}\right)^{d-3} (m-1) \tag{4.5}$$

that is the refractive index of the monomers multiplied by the density of the aggregate. If the monomers satisfy the assumption $m \sim 1$ (that implies also $m-1 \sim 0$), these relations still hold for fractal aggregates because the multiplying coefficient is smaller than 1.

The optical thickness of a spherical particle of radius R is defined as $\rho = 2kR(m-1)$, where $k = 2\pi/\lambda$ is the wavenumber of the incident radiation with wavelength λ. The same thickness can now be defined for fractal aggregates as

$$\rho = 2kR_g(m_{av} - 1) = 2ka \left(\frac{R_g}{a}\right)^{d-2} (m-1). \tag{4.6}$$

It is very interesting to notice that this expression can be directly related to the expression of the optical thickness of the monomers that compose the aggregates. If this is called ρ_0, the optical thickness of the aggregates is simply given by

$$\rho = \rho_0 \left(\frac{R_g}{a}\right)^{d-2}. \tag{4.7}$$

In the limiting case of $d = 2$ the optical thickness 4.7 is the same both for monomers and for aggregates. Conversely it may increase or decrease with respect to the monomer value depending on the value of fractal dimension. We notice that the results 4.5 and 4.7, which have been obtained through the Maxwell-Garnett approach, can also be derived by assuming a uniform mixing of materials with volume fraction f, as described in . This is the result of the small refractive index gap, or $\epsilon_m - \epsilon \ll \epsilon_m$, as provided in [33].

The expression for the optical thickness is relevant because it can be directly related to the forward scattered field $S(0)$. The expression for the forward scattered field can be reduced to the simple form [12, 31]

$$S(0) = x^2 K(i\rho) \tag{4.8}$$

where ρ is the optical thickness, $x = kR_g$ and the function $K(x)$

$$K(w) = \frac{1}{2} + \frac{e^{-w}}{w} + \frac{e^{-w} - 1}{w^2} \tag{4.9}$$

results from the integration across the sphere. By a power series expansion of this function, the real and imaginary parts of the scattered field $S(0)$ can be approximated as

$$\mathrm{Re}[S(0)] = x^2 \frac{\rho^2}{8} \tag{4.10a}$$

$$\mathrm{Im}[S(0)] = x^2 \frac{\rho}{3}. \tag{4.10b}$$

SPES measures the extinction cross section that is related with $S(0)$ via the optical theorem :

$$C_{ext} = \frac{4\pi}{k^2}\mathrm{Re}[S(0)] \tag{4.11}$$

and Im$S(0)$ from the interference between the transmitted and the scattered beam. Thanks to this combined measurement the two parameter x and ρ can be obtained. Their knowledge permits to get the fractal dimension and the size of the aggregates.

4.2.2 SPES Measurements

The experimental setup for SPES measurements is composed by a laser beam ($\lambda = 635nm$) focused inside a flow cell which in our case is 1.5 or 0.2 mm thick. The sensor is placed in line with the laser and the cell to collect the light, in a configuration similar to a in-line holography apparatus. The signal collected is sent to a analog to digital converter (PicoScope: Pico Technology) and therefore to a processor unit that processes the data which are finally analyzed in terms of the real and imaginary part. The sample flows through the cell and must be very diluted in order to measure single particles. The sample previously described is studied at different time, referring at the moment in which the salt is added to the solution ad zero time. The acquisition is performed up to four hours, one every 30 min.

In figure 4.1 a typical results of a SPES measurement is reported. Each point in the plane Re[S(0)]-Im[S(0)] represents the measurement for one particle. Data can be analyzed with the model previously described to obtain the parameters of interest, i.e. size and fractal dimension. By the measurement of the dimension on single particles, an histogram for the size is obtained. In fig. 4.2 two histograms for two different data sets are reported. I compare this distribution with the theoretical one, eq. 3.11, for the DLA limiting condition [26]. The fit with the data is not a very good one. I also tried to find a different function to fit the data, and a lognormal curve seems to be in good agreement with the data. However to be model independent I do not consider the fitting function but directly the data.

At the same time the measured fractal dimension is 2.2 and remains almost constant (within ± 0.1) all over the measurement. If this value is compared to what is usually obtained with scattering experiments it appears higher than the expected ~ 1.8. A more complete description on the interpretation of the data will be explained later on in this chapter.

Another kind of analysis that can be performed is a dynamic scaling on mass distribution [34]. When the size distribution exhibits dynamic scaling it can be defined in dependence of a scaling function that is independent in time. The time dependence is inserted with the scaling parameter. Considering the size distribution depending on time, it can be defined as

$$N(M,t) = P_n^{-2}\psi(M/P_n) \tag{4.12}$$

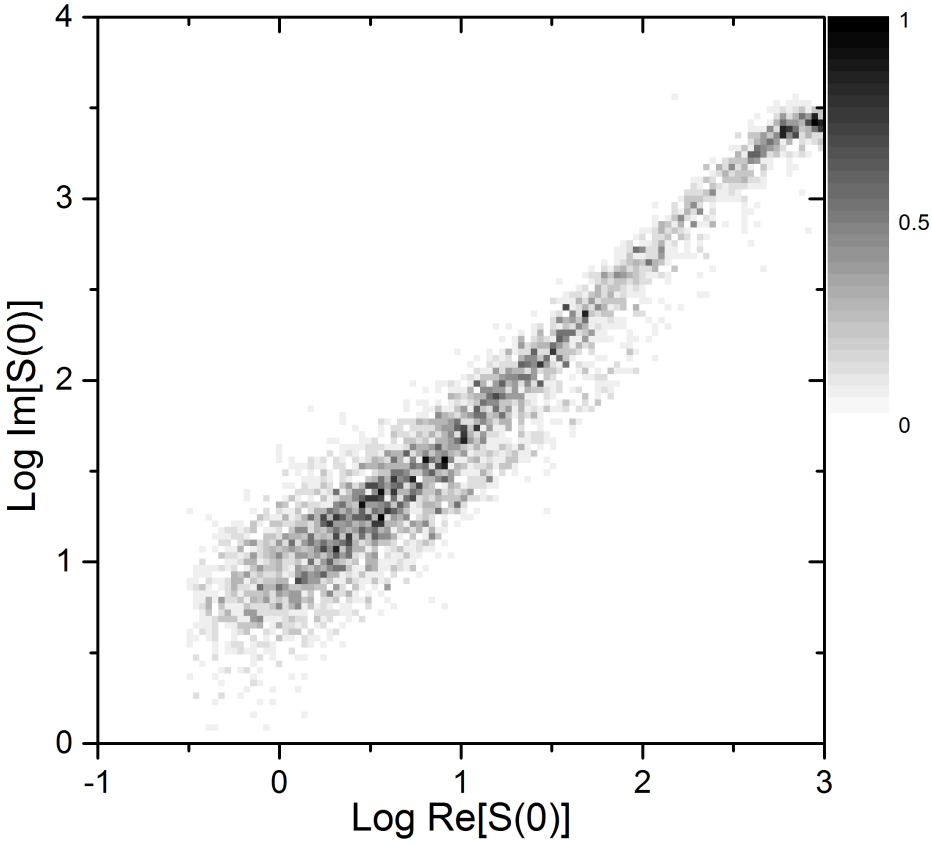

Figure 4.1: Example of the results of the SPES measurements. This 2D histogram represent the data collected with the aggregating sample after 150 minutes from starting the aggregation process.

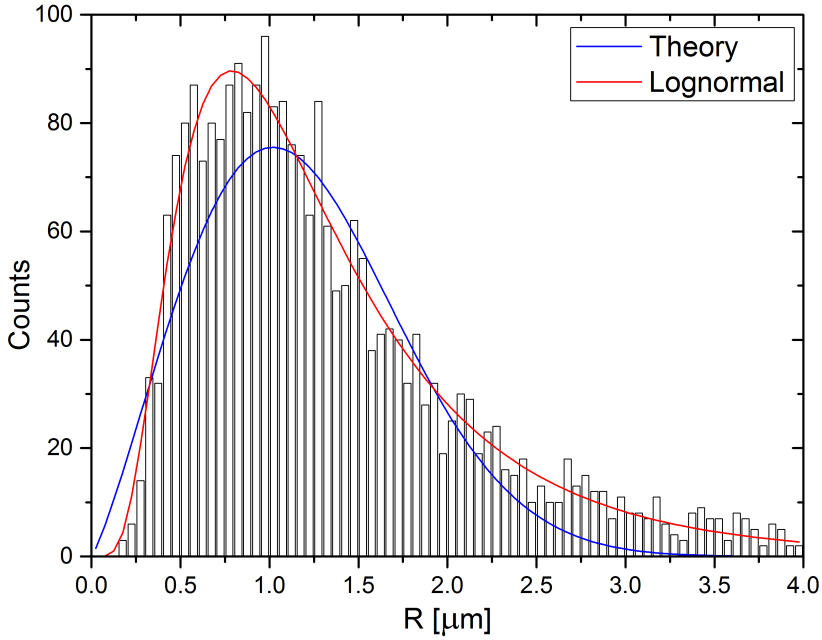

(a) Aggregation after 60 minutes.

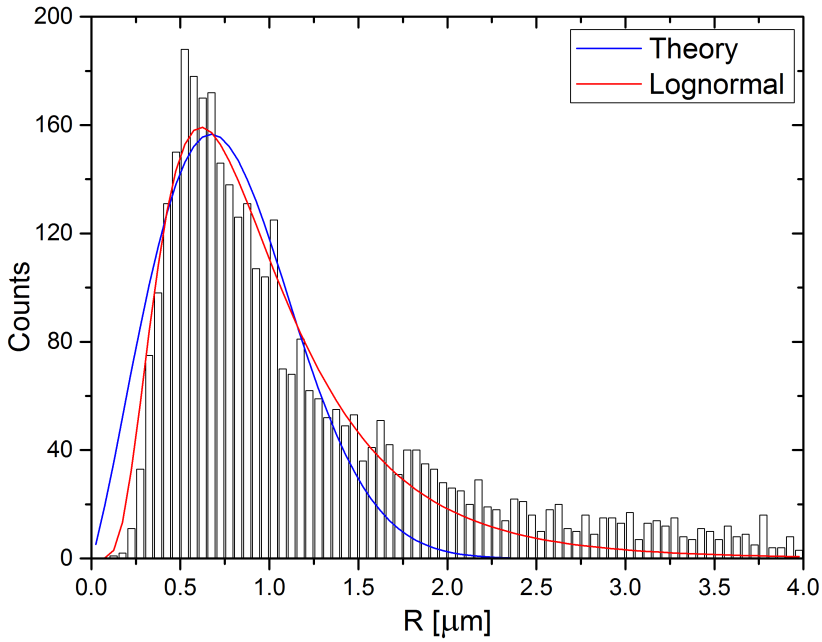

(b) Aggregation after 150 minutes.

Figure 4.2: Examples of the histogram representing the size distribution of the aggregating sample. The blue and the red line represent the fit of the data with two different function: the blue one is the eq. 3.11 converted from mass to radius, the red one is a lognormal function.

where P_n is the n-th moment of the distribution. To simplify the notation, we can also define $S_n = \sum_M M^n N(M)$ such that $P_n = S_n/S_{n-1}$. If N=1, S_1 represent the total number of particles and P_1 the first moment, i.e. the average mass.

All the different measured distributions can be easily converted from radius to mass and then normalized over the total number of particles and finally rescaled inverting eq. 4.12 with $n = 1$. In figure 4.3 the result of this procedure is shown. Colors and symbols

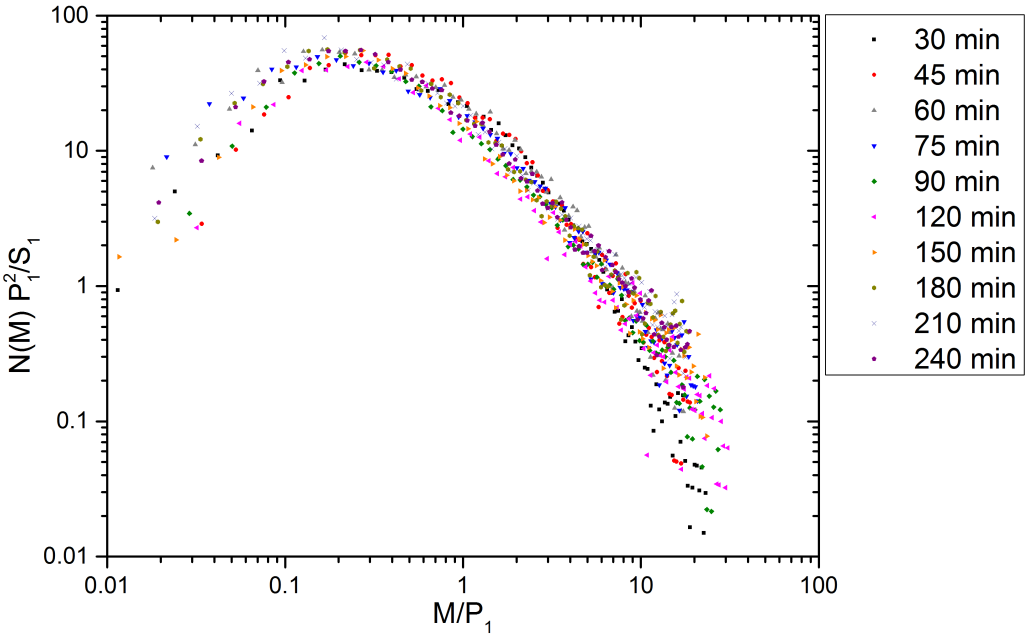

Figure 4.3: Results of the rescaling of the measured mass distribution functions.

code different times of aggregation. The collapsing of the curves is good as expected; for higher reduced mass the noise of the data is due to the small counts in the starting distribution.

4.3 NFS Measurements

Here I report the results obtained on these samples with the NFS technique. With these measurements I obtain informations on the aggregate structures. Moreover, since this is the first time that the SPES technique is applied to fractal aggregates, it is important to have an independent validation of SPES data.

4.3.1 Setup

The experimental setup is composed by a laser, $633nm$ of wavelength, spatially filtered and collimated, the sample in a couvette thermally insulated, a microscope objective and a CCD. The sample was in a couvette with a optical path of $2mm$ and then in a thermally insulated container. The working temperature was the room one but the insulation was necessary to reduce as much as possible any temperature gradient that may

give rise to convective motions. Two apertures on opposite sides of the container allow the laser beam to reach the cell and the microscope objective to collect the scattered light in the near field. The nominal magnification of the objective was 20x with numerical aperture of 0.4 and it was coupled with a CCD with sensor sizes 1024x1024 pixels and single pixel of $5.3\mu m$. The detailed procedure of calibration is reported in appendix A.

4.3.2 Technique of data analysis

As already explained in previous sections, the usual techniques applied in the NFS data analysis use couples of images to compute the power spectrum. If the two images are not correlated, i.e. $G_E(\mathbf{q}, \tau) = 0$ in eq. 2.14, the static form factor is found. By contrast the study of the correlation function allows to find the characteristic time of diffusion at different q-vectors and then the dynamic properties of the studied samples. These two analyses can be simultaneously performed in COLLOID experiment. The absence of gravity allows to perform dynamic measurements with images with long lag times, up to some tens of second. On ground, because of the presence of gravity, this dynamic measurement is very hard to be done. In fact, on long time-scales the diffusive motion is hidden by the thermal convective motions, so that images have to be acquired faster.

To perform combined analysis of static and dynamic light scattering a different analysis has been used. With images acquired at 5 fps, the power spectra were calculated for couple of images at different lag times, as for the dynamic analysis in eq. 2.14. In the usual dynamic analysis this intermediate scattering function is studied at fixed angle as a function of time (see the eq. 2.15). This new analysis is based upon studying spectra at a fixed time τ_0 as a function of q. Now the intermediate scattering function that has to be used to fit the experimental spectra is

$$I(q, \tau_0) = 4I(q)(1 - \exp(-Dq^2\tau_0)) \tag{4.13}$$

obtained combining eq. 2.14 and 2.15. The main issue is now about $I(q)$. Even if it is written only in terms of the q-dependence, it may depend also on other variables, for example the dimensions of the studied object, and more in general the shape of the particles ($I(q)$ is the form factor of the particles). It represents a sort of limitation: it can be only applied on samples of which the expression of the form factor, i.e. $I(q)$, is known. If the form factor not only depends on q, but also on other parameters, these become free parameter in the fitting procedure. This kind of analysis allows to find at once the information about the static and dynamic features of the studied sample.

4.3.3 Calibrated samples

To test the method of data analysis I have studied a sample of calibrated particles. The images are acquired in group of 100 images at a frame rate of $5fps$, and the analysis is then performed on the difference of images, as typical for the NFS double frame technique. The particles are polystyrene spheres $2.1\mu m$ in diameter. In eq. 4.13, the form factor $I(q)$ of spherical particles is analytically predicted by Mie theory. However, to avoid the introduction of some properties conditioned not only on the size of the particles but also on other features such as polydispersity, I directly measure the form factor and use it in the fitting function. The only free parameter is then the diffusion coefficient D. The result of the fitting procedure is shown in fig. 4.4. The fit is good for high values of q (q>1) while for lower values the data and the fit are quite different. This can be due to the fact that for low q values the characteristic times of diffusion become too long in respect of the time of other spurious motions, as can be sedimentation or translation.

However, the values obtained by fitting of the last part, about 80 points, are in good agreement with the theoretical ones.

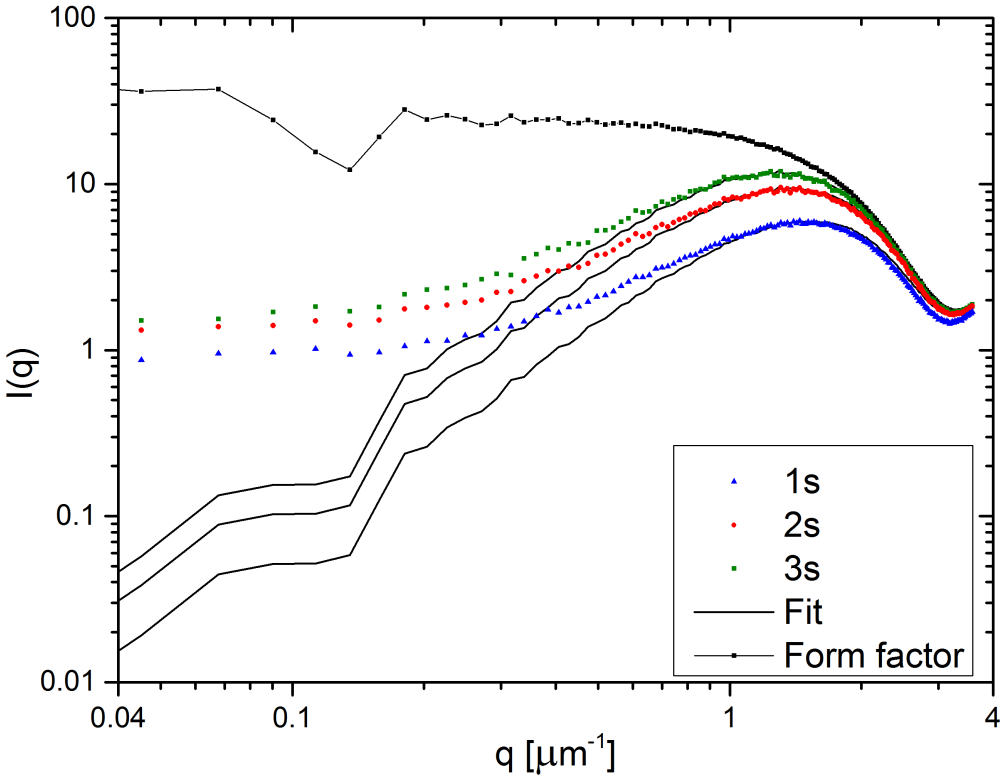

Figure 4.4: Example of the procedure of data analysis with the intermediate scattering function. The three different data sets represent the intermediate scattering function in step of 1 second. The black line represent the fitting function while the line with dot is the measured form factor.

4.3.4 Aggregating samples

Once the method is validated with calibrated particles I apply this analysis to the aggregating samples. Because also this kind of aggregates presents fractal structures, the procedure of data analysis is the one already described in the previous chapter: the diffusion coefficient D is replaced by an effective diffusion coefficient D_{eff} defined by eq. 3.10 to keep into account rotational diffusion [24, 25]. Because in this case the data are too noisy to build a master curve, the relation between D_{eff} and D of eq. 3.10 is approximated in the limit of $qR_g \gg 1$ to

$$\frac{D_{\text{eff}}}{D} = 1 + \frac{1}{2\beta^2} \tag{4.14}$$

where β is again the ratio between the hydrodynamic and gyration radii. Using Fisher-Burford form factor (eq. 3.7), the equation 4.13 for the intermediate scattering function

becomes

$$I(q,\tau_0) \propto \left[1+\frac{2}{3d}(qR_g)^2\right]^{-d/2}\left[1-\exp(-D_{\text{eff}}q^2\tau_0)\right] \tag{4.15}$$

The free parameters of this function are R_g, d, D_{eff} and a multiplying constant. The fitting procedure of the data with this function has four free parameters, which could bring some difficulty. To simplify, two parameters can be fixed in a different way: from the power spectra high-q range for couple of images almost uncorrelated the fractal dimension and the multiplying constant can be found. The fitting procedure is then reduced to have only two free parameters, R_g and D_{eff}.

Once that all the fitting parameters are found, the hydrodynamic radius can be calculated. If the dependence on the R_H is written explicitly from the equation 4.14, a third degree equation is obtained

$$2\frac{6\pi\eta}{k_BT}D_{\text{eff}}R_H^3 - 2R_H^2 - R_g^2 = 0 \tag{4.16}$$

with R_H as the unknown. Solving this equation the hydrodynamic radius and then the value of β can be obtained.

Images are acquired every 5 minutes for about one hours; each acquisition is composed by 100 images at a frame rate of $5fps$. Again the analysis is performed on the difference of images. A typical set of curves to analyze is shown in fig. 4.5. The different curves correspond to different lag-times of the subtracted images. On this graph I also plot the Fisher-Burford form factor. As already explained before the acquired data are not sufficiently decorrelated to compute directly the static form factor and the procedure with the intermediate scattering function is needed. An example of fitting with eq. 4.15 is shown in figure 4.6. Again the fit is good only for high values of q. To have a better reliability on the values of fitting parameters, for each acquisition fits on different lag-times are performed. Within the experimental errors the parameters used for the fits remain the same. The fractal dimension obtained by this kind of fit is around 1.7, as expected for a DLA process.

Once the fitting parameters are found, I calculate the hydrodynamic radii and then the values of β. In figure 4.7 the results of one measurement are reported. The values of β are not constant. This is maybe due to the fact that the aggregates haven't still a fractal internal structure, but they are still rearranging. However, by an extrapolation of their behavior, the asymptotic value for $M \longrightarrow \infty$ (or $t \longrightarrow \infty$) appears to be around 0.7-0.8. It is obtained by a fitting procedure of the data with two different decaying functions: a power law 1/x and an exponential e^{-x}. These values are still higher respect to what expected for an exponential cutoff function in the density distribution; in fact for a fractal dimension of 1.7 it should be 0.46. However as shown in fig. 4.8 this value is in agreement with the values obtained in literature (see table 4.1) and also with the COLLOID experiment.

4.4 Comparison of SPES and NFS results

The analysis performed in the previous section with NFS technique are realized considering that the sample is monodisperse. However it is reasonable to think that there is a distribution in size as obtained with the SPES measurements. However the fractal dimensions obtained with the two techniques are quite different; in fact with the SPES measurements the fractal dimension is around 2.2, while with NFS is 1.8. Also performing the NFS analysis using the theoretical distribution of eq. 3.11 change the fractal

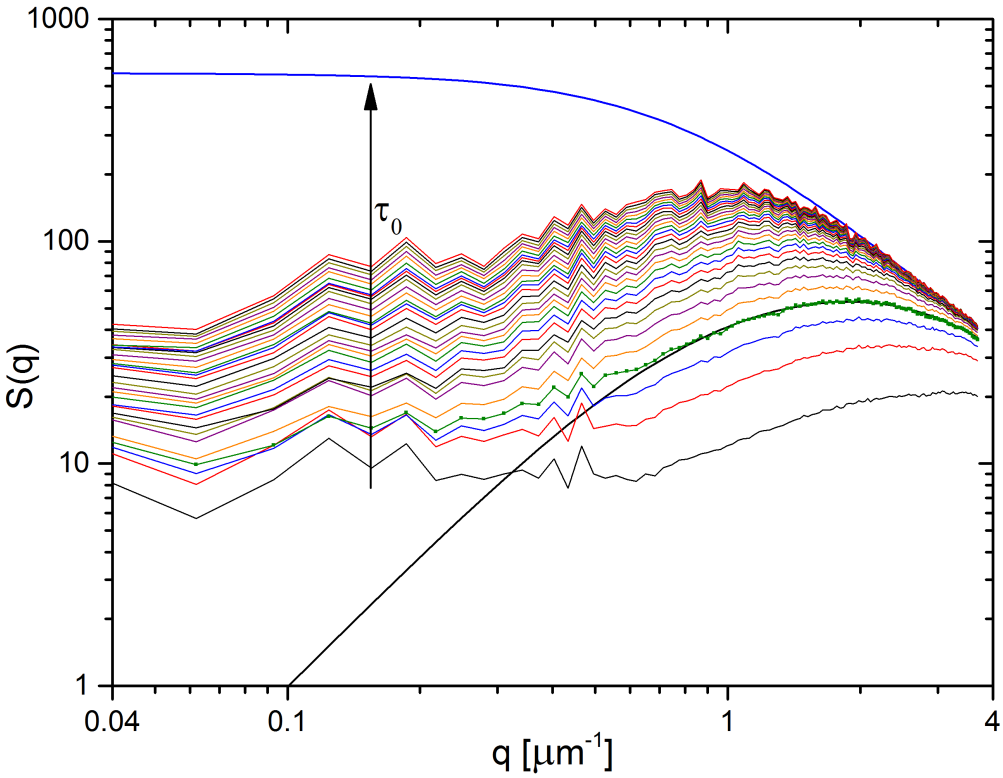

Figure 4.5: Evolution of power spectra in time. The colored curves represent the data obtained with different lag-times. The time step from each curve to the next one is of 0.2 second, corresponding to 5fps. The black line represents the intermediate scattering function for 1 second of lag-time that fits the relative data (green line+dot curve).

Author	Fractal dimension	β
Lin *et al* [35]	1.85	0.93
Wang *et al* [36]	1.75	0.71
	2.15	0.97
Kaetzel *et al* [37]	1.5-1.85	0.79
Wiltzius *et al* [21]	2.1	0.72
Lin *et al* [38]	2.1	1

Table 4.1: Summary of some experimental values of fractal dimension and β [27].

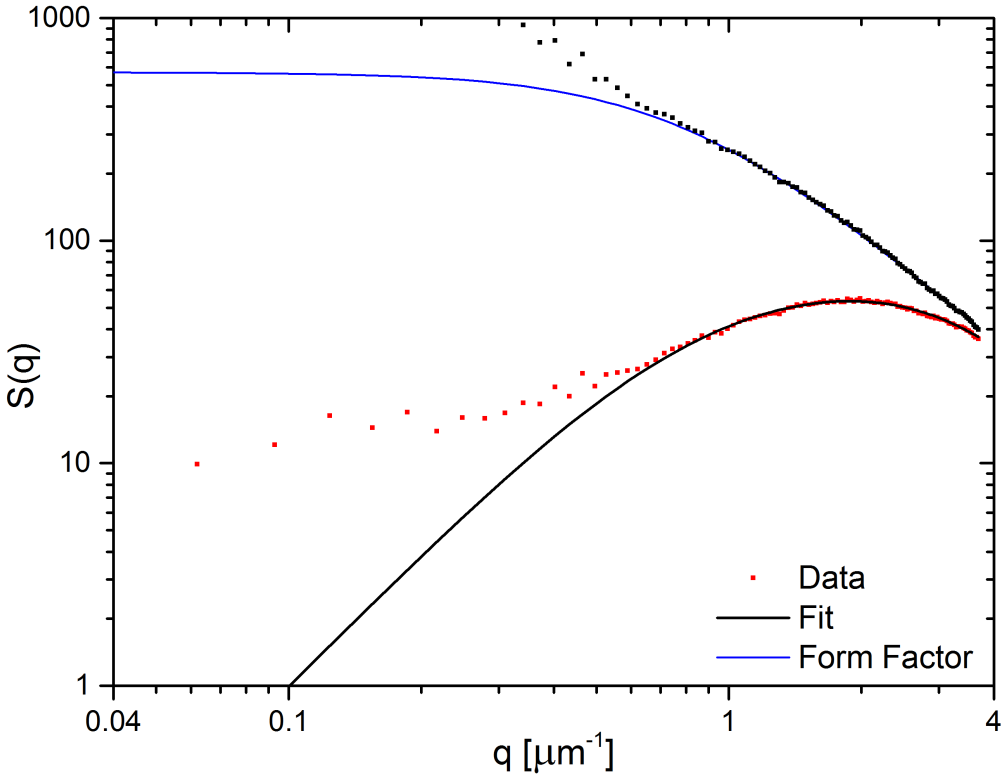

Figure 4.6: Example of the fitting procedure. The red line (the green data in fig. 4.5) are the data at lag-time of 1s. The black one is the intermediate scattering function that fit the data. The blue line represent the form factor obtained by the fitting procedure and the black point are the reconstructed form factor and the black dots are the reconstructed form factor from dynamic data. Their agreement is good until the black line fit well the red data.

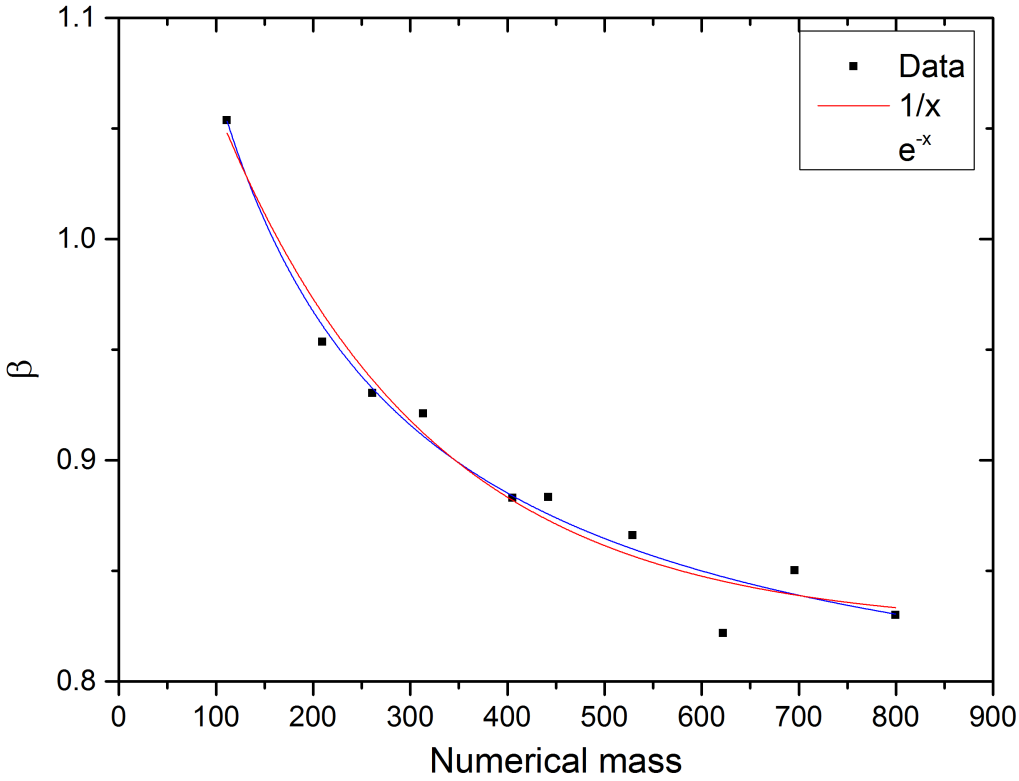

Figure 4.7: Values of β as a function of the numerical mass, i.e. number of monomers, of the aggregates. The blue and the red curves represent two fitting function, respectively a power law and an exponential decaying function.

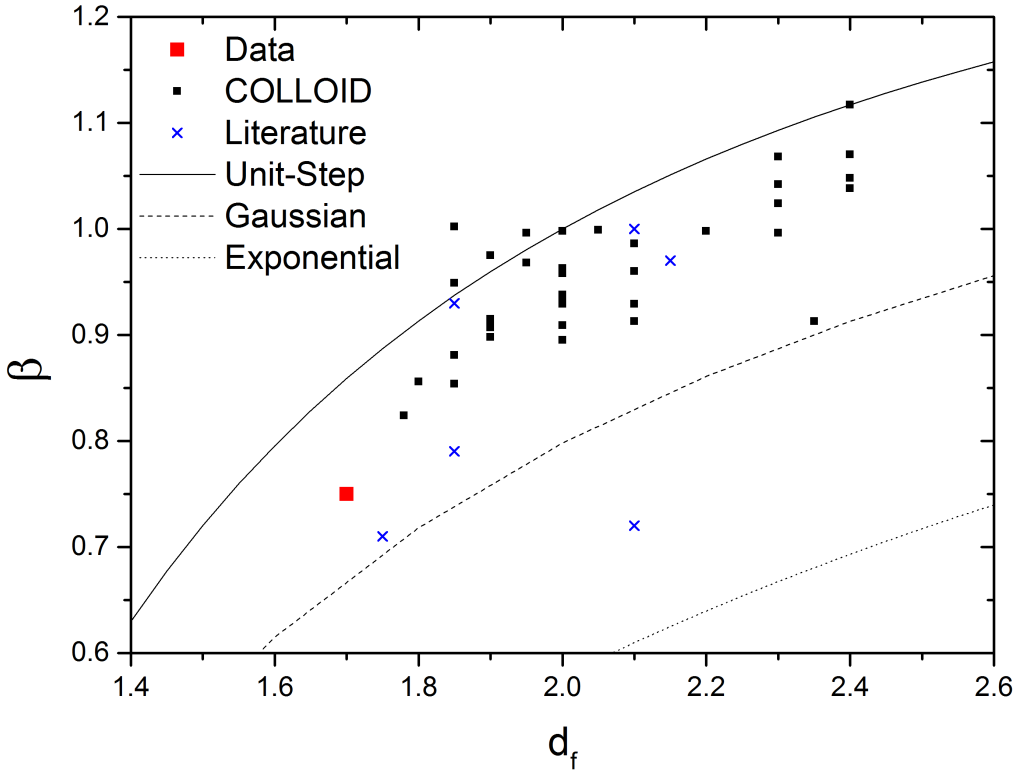

Figure 4.8: Values of β as a function of the fractal dimensions. The red point is obtained with the measurements explained in this section. The black point represent the results obtained with the COLLOID experiment while the blue ones are some literature results (table 4.1). The line represent the different expression for β as a function of d for the three different cutoff function.

dimension to 1.9, higher in respect to the monodispersed one but still different to the SPES measurements.

4.4.1 Static analysis

I want to verify the reliability of the SPES data. Because the measurements with NFS and with SPES doesn't have simultaneous data, I generate power spectra reflecting the behavior of the data obtained with NFS. These power spectra assume the role of data and SPES measurement will be compared to them. These 'data' are represented by a simple Fisher-Burford curve with the fractal dimension 1.7, obtained by NFS measurements.

With the SPES size distribution, I generate the polydispersed power spectra using the relation

$$S^{poly}(q) = \frac{\sum_M N(M)M^2 S(q,M)}{\sum_M N(M)M^2} \tag{4.17}$$

where N(M) is the distribution measured with SPES and S(q) is the spectrum of the single aggregates with the dimension relative to the mass M. The fractal dimension is imposed to be 2.2. Even if the measured distribution was well fitted with a lognormal function as already shown in fig. 4.2, I decided to use the real data as distribution function to not add any additional parameter. The resulting constructed spectra are shown in figure 4.9. Even if there are some small differences in shape, the reconstructed power spectra are very similar to the monodispersed case. The procedure for the comparison of the data is the following: with the SPES distributions all the monodisperse form factors are weighted by their squared relative masses and their size distribution values. The parameters of the form factor are the radius relative to the mass M and the fractal dimension is the measured value of 2.2. Notice that this reconstructed form factor doesn't have any free parameter. The only assumption is the shape of the form factor for every single aggregates while the number mass distribution is measured. The resulting form factor $S^{poly}(q)$ is then fitted with the monodisperse one, with fractal dimension of 1.7 as measured with NFS technique. The radius in this last form factor is the only free parameter. The best superposition shows something interesting: the resulting fractal dimension of the traditional scattering experiment is different from the fractal dimension that can be obtained measuring the single aggregates. In fact a superposition of form factor of fractal aggregates with higher fractal dimension, i.e. 2.2, brings to a lower fractal dimension if measured with NFS.

4.4.2 Dynamic analysis

In a similar way also the dynamic behavior can be reconstructed. In particular I want to reconstruct the intermediate scattering function for the polydispersed sample and compare it again with the monodisperse function obtained with NFS parameters. The NFS intermediate scattering function is computed using the form factor that is obtained as described in the previous section. It is then multiplied for the exponential decaying function with characteristic time $\tau_c = 1/D_{\text{eff}}q^2$, where D_{eff} is defined with the formula 3.10. The only free parameters are the value of β or R_H and the lag-time τ. The first is the parameter that I want to find while the second is just an arbitrary parameter. The gyration radius and the fractal dimension are already known by previous measurements. This function acts again as simulated data to which the SPES measurements will be compared.

Working with NFS in heterodyne condition the field correlation function is measured and the additivity of the field correlation function can be used to compute the polydis-

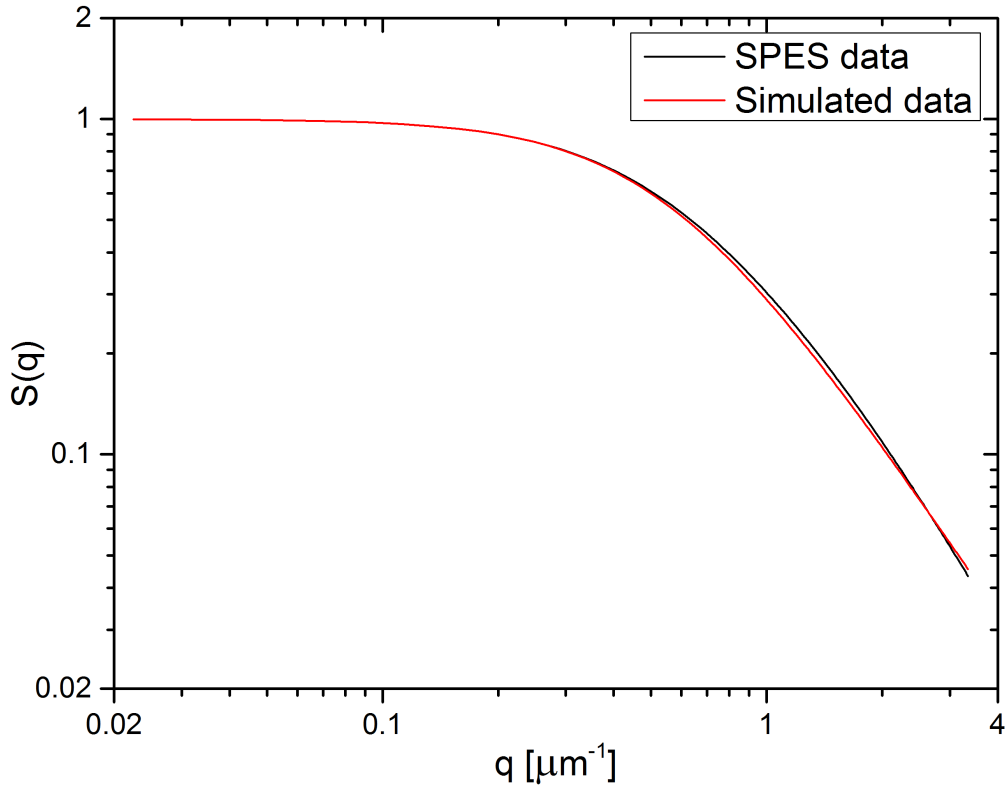

Figure 4.9: Comparison of the reconstructed form factor. The black line represent the polydisperse form factor obtained with SPES data. The red line represent the form factor of a monodisperse sample with NFS parameter.

perse intermediate scattering function. In way similar to the S^{poly}, the intermediate scattering function can be calculated as

$$I(q,\tau) = \frac{\sum_M N(M)M^2 S(q,M) \mathrm{e}^{-D_{\mathrm{eff}}(q,M)q^2\tau}}{\sum_M N(M)M^2} \tag{4.18}$$

where the sum is performed on the experimental points. The D_{eff} is calculated with the formula 3.10 and $S(q,M)$ is the Fisher Burford expression. In this formula the only free parameter is the lag-time τ. Once that the lag-time is fixed, the same for the monodisperse scattering function, the result of this computation is compared to the simulated data. An example of the results of this procedure is shown in figure 4.10.

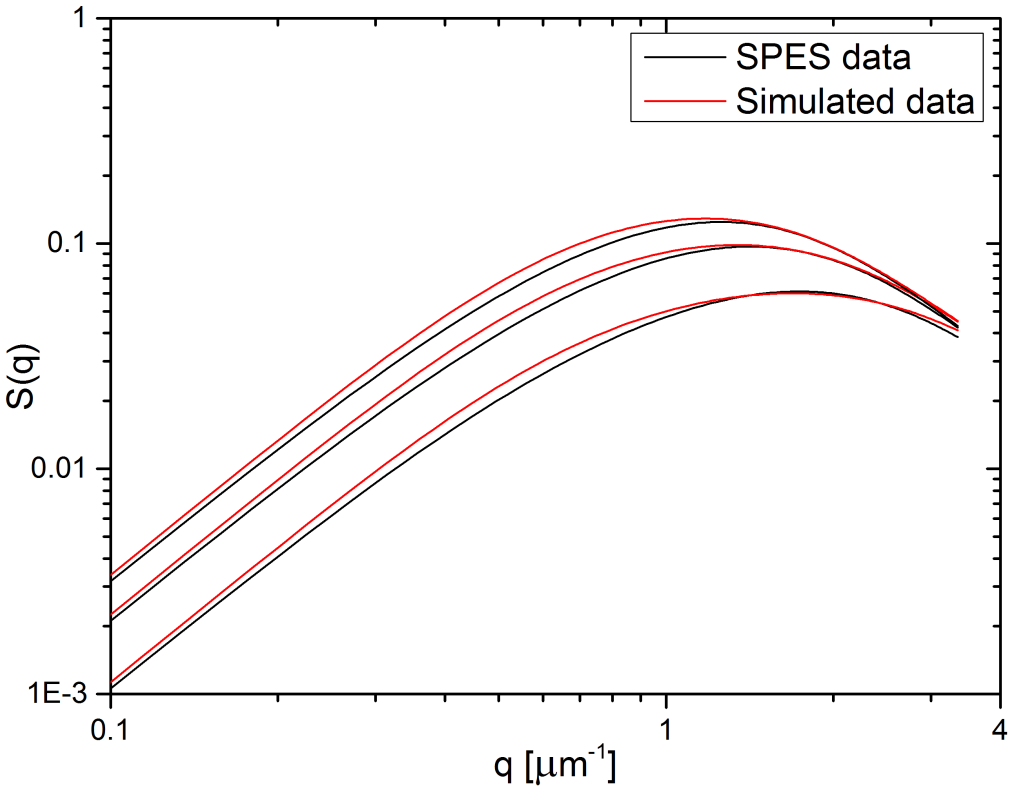

Figure 4.10: Comparison of the reconstructed intermediate scattering function. The black lines represent the polydisperse form factor obtained with SPES data. The red lines represent the form factor of a monodisperse sample with NFS parameters. The different couples of curves are relative to different value of τ, respectively 1, 2 and 3 second from bottom to top.

The two curves do not superimpose precisely, especially at low q values. Also in higher q range the shape is not really the same. This difference can be caused by the small difference in the form factor shown before and also by the difference in summation. Even in this not perfect condition I try to fit in the best way the last part (q>1) of this curve, for different lag-time. By this fit I obtain values of β that remain constant for all the

aggregation process of SPES measurements. Its value is higher than the one obtained before. However also the new fractal dimension increases. Again this new couple of parameter is still higher than the one obtained with exponential cutoff function for the density of the aggregates. It indicates aggregates with a compact structure, between the gaussian and the unit-step cutoff function.

4.5 Conclusions

With the SPES technique we measure the size distribution of aggregating samples in DLA regime. The measured distribution is different in respect the theoretical one. A good fit to the measurement is provided by a lognormal function. In the procedure of data analysis however only the measured data have been used, without any needs of theoretical model. Samples prepared in the same way are also studied with NFS technique, obtaining results similar to the ones usually obtained in literature. The SPES data are then compared with the results obtained with NFS experiment. Because there wasn't simultaneous data with the two different techniques I simulated the scattering data as the monodispersed power spectrum (Fisher-Burford expression) with the parameters obtained by NFS measurements. The compatibility in the form factor is good. The resulting fractal dimension with SPES is 2.2, while with NFS is 1.7. This two different values show that the single aggregate exhibits fractal structure with higher fractal dimension with respect to what measured with scattering that averages on many aggregates. The combination of the form factor of each single aggregate with high fractal dimensions weighted with the measured size distribution, with the only assumption of a Fisher-Burford form factor for each single aggregate, build a polidisperse form factor that exhibit a lower fractal dimension compatible with the one measured with scattering experiments.

Looking at the dynamic properties the two different measurements show some difference in the intermediate scattering functions. To reach a better understanding on the compatibility of the two different sets of data other kind of analysis should be performed. Thanks to dynamic scaling of the size distribution, a general function describing this distribution can be found. Starting from this function the size distribution can be reconstructed for each fixed average dimension with rescaling laws. With this new kind of function both the form factor and the intermediate scattering function can be computed and directly compared to sets of measured data with scattering technique, and not to simulated data. It may also lead to the definition of a new general function describing the size distribution that can be applied to other different cases.

Chapter 5

Anisotropic Interactions

The work shown in this section is realized in collaboration with Peter Schall group at UVA, (Amsterdam university). They realized and provided us some samples that perform critical Casimir aggregation. The main difference of this sample respect the ones used in the COLLOID experiment is that the particles are not spherically symmetric. This particular feature of the particles combined with a different treatment of the surface make the interaction potential asymmetric. To have a better understanding of the sample itself we provide a characterization of the particles with different optical techniques that give us an overview on some of the properties of those samples. We measure the concentration of the particles in the solution, the size distribution and the scattering form factor.

5.1 Samples

The studied samples are composed by a binary mixtures of 3MP and D_2O and particles of PMMA (poly-methyl methacrylate). The phase diagram of this binary mixture is represented in fig. 5.1. It is the same of the one for the COLLOID sample, the only thing that changes is the presence of pure heavy water and not a mixture with normal water. However it does not change the shape of the phase diagram, it just moves down of some degrees the line of phase separation. The binary mixtures were prepared at two different concentrations: one is at a concentration of 25% in weight of 3MP and the other one is at 33%. At those values the mixtures exhibit phase separation respectively on the left or on the right side of the critical point.

In the binary mixtures were then suspended micron-sized anisotropic particles of PMMA. The particles are dumbbells and are sketched in fig. 5.2a. They are composed by two spherical particles touching on the surface and kept together by a middle polymeric part forming capsular-like particles. The central and the spherical parts had different surface properties such that the former is hydrophilic while the latter is hydrophobic and prefer the 3MP component of the mixtures. Those different properties give to the suspension a peculiar behavior: on the left side of the critical point the interaction between two different particles is attractive for the spherical parts while is repulsive for the central one (fig. 5.2b). Instead on the right side is the opposite behavior, the central part is attractive and the spherical is repulsive (fig. 5.2c).

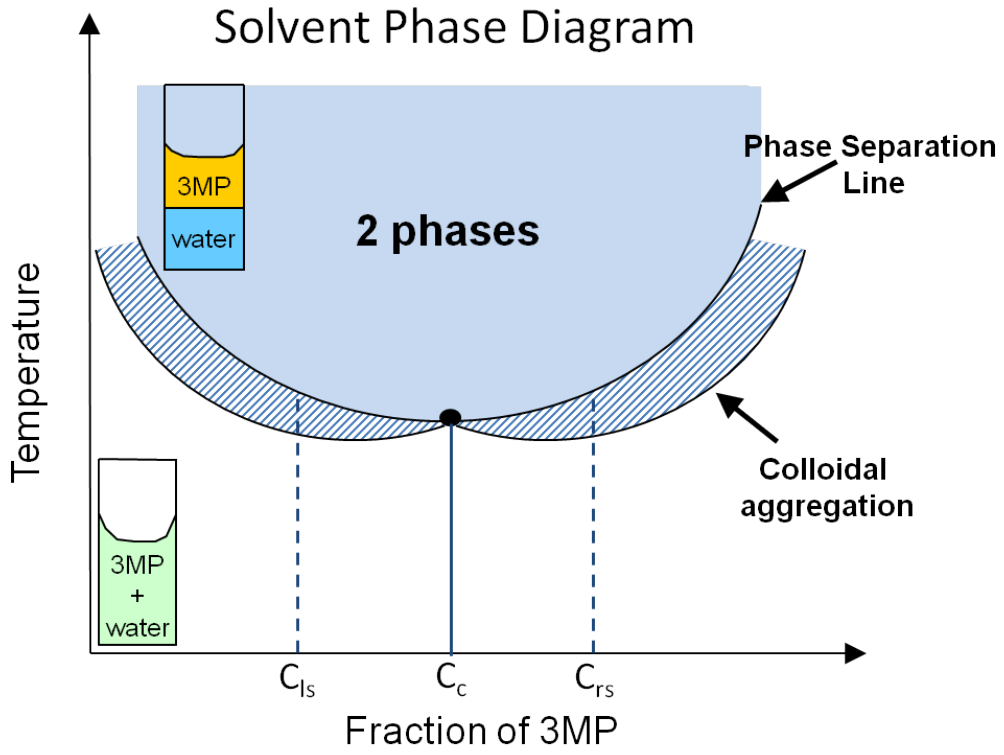

Figure 5.1: Phase diagram of the binary solution of heavy water and 3MP. C_{ls} and C_{rs} represent the two values of concentration of 25% and 31% of 3MP respectively on the left and right side of critical point

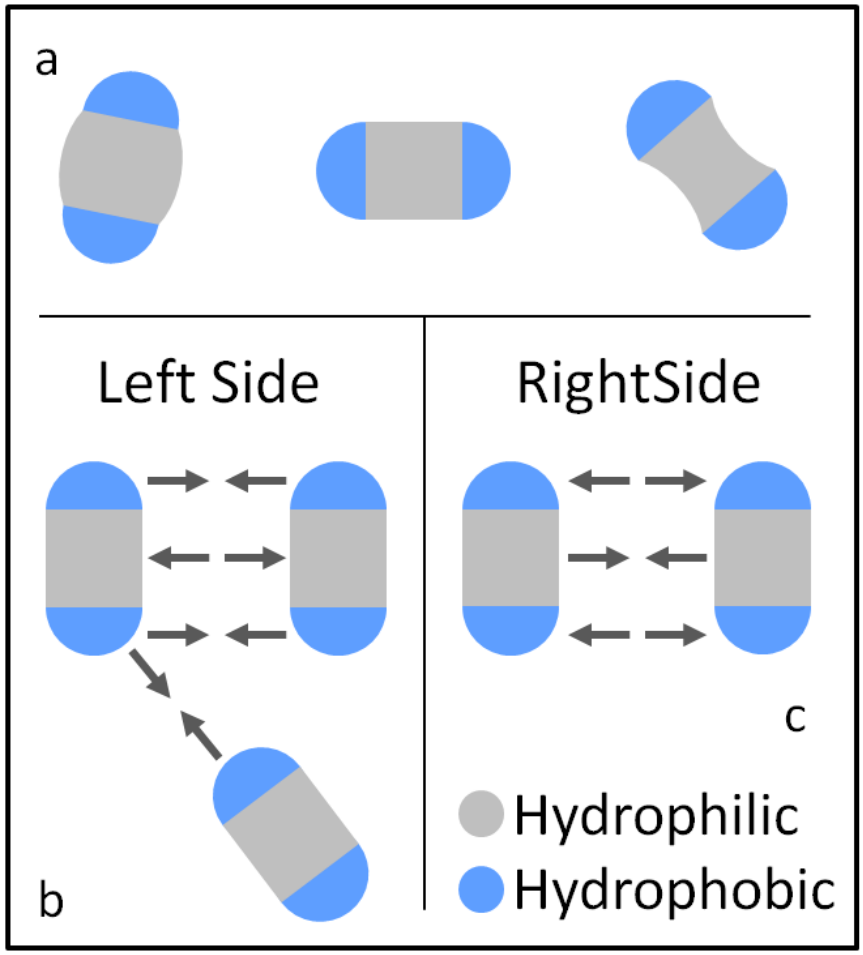

Figure 5.2: Sketch of the dumbbells particles. In *a* is represented the three different shape that the particles may have. In *b* and *c* are represented the different kind of interaction depending on the concentration of the mixtures in which they are suspended respect the critical point composition.

5.2 Turbidimetry measurements

The first technique used to study the sample is the turbidimetry [12]. It measures the turbidity of the sample comparing the incoming and the transmitted light. More in detail, the incoming light has a certain intensity, namely I_0. After passing through the sample it may decrease depending on some features of the sample. Let I be the intensity coming out from the sample. The value of I is related to I_0 via the Lambert-Beer law

$$I = I_0 e^{-Ln\sigma} \tag{5.1}$$

where L is the thickness of the sample, n the numerical concentration and σ the extinction cross section. The reciprocal of $n\sigma$ is called extinction length L_{ext}. The turbidity of a sample depends on two different effect: the diffusion and the absorption. For the sample of interest at the wavelength used (633nm) the absorption is negligible and only scattering is considered. The extinction cross section that is usually the sum of absorption and scattering cross section reduces to the scattering cross section.

The apparatus for turbidimetry measurement is composed by a laser diode 650 nm in wavelength spatially filtered and collimated, a cell holder for couvettes of thickness 2mm, and the collecting device. Because the collected light must be only the transmitted beam and not the scattered light, before collecting the light with a photodiode a spatial filtered is mounted. It is composed by a focusing lens and a pinhole (aperture 50 μm) in the focal plane of the lens, such that the scattered radiation is obscured and only the 0-angle radiation is collected. Because of the filtering procedure the alignment is a very important requirement. Even the slightly different positioning of the cell may induce some deviation to the beam such that the alignment is lost. To overcome this trouble the pinhole and the photodiode were mounted on a transversal moving support. To simplify the procedure and make it faster the centering of the pinhole was realized in automatic way. Two step-motor were used, one for each axis, to control the motion of the support. Thanks to a gearing down of the step-motor the precision in the position of the pinhole was of just some micron, smaller than the dimension of the pinhole (50 μm).

The measurement has to be performed in two steps. The first is the measurement of I_0 with only the binary mixtures of 3MP and D_2O. The value of I_0 is not considered the intensity of the laser diode because I am interested not in the extinction length of the particles and the mixtures, but just the particles. So the measurement of the mixtures gives the reference needed for the particles. The second step is to measure the mixtures with the particles. With the cell $2mm$ thick, the ratio I/I_0 is around 37%. By numerical simulation the scattering cross section of the particles can be computed using approximate shape and dimensions for the particles. The simulations are realized with ADDA. The resulting scattering cross section for dumbbells particles of dimensions of about $1\mu m$x$2\mu m$ is $6.0\mu m^2$. With this value is possible to have an approximate value of the concentration useful to prepare the sample used later on. The concentration is 8.3 10^4 $\frac{particles}{mm^3}$, a value that is compatible with what expected.

5.3 SPES measurements

A second measurement on the dumbbells particles is realized with the SPES technique, already described in section 4.2. If for spherical particles and for colloidal aggregates a model can be realized to explain the data, for anisotropic particles it is not possible. However some information can be found by looking at the data distribution in the plane Re[S(0)]-Im[S(0)].

The samples measured with this technique are two: the first is composed of spherical particles while the second is a solution of dumbbells particles. The results of the measurement are shown in the figure 5.3a for the spherical particles and in the figure 5.3b for the dumbbells.

In both the histogram of spheres and dumbbells there is also a small second peak at the corresponding values of dumbbells and spheres respectively. It depends on the same preparation of the particles. In fact the dumbbells are prepared by joining two different spheres with a polymeric material that keeps them attached. Then the spheres and the dumbbells are separated with a centrifuge, or just by settling, so the separation may not be perfect.

5.4 NFS measurements

The third technique used on which I focus my attention is the near field scattering. With this technique I study the form factors of the dumbbells and of the early stages of aggregation. Because I study the samples with a scattering technique, the samples had to be diluted to a concentration such that the scattered intensity is much smaller (some percent) of the transmitted beam. It allows to avoid multiple scattering but at the same time it increases a lot the time scale of the interaction, from minutes to several hours. I focus my attention on the sample on the left side of the critical point because the interaction is much stronger than on the right side.

5.4.1 Setup and experimental procedure

The experimental apparatus is the same of the one previously described in sec. 4.3.1, except for the cell. Because this sample exhibit Casimir interaction it was thermally controlled with a water thermal bath. The water at the desired temperature circulates in the cell holder and controls the temperature of a second small thermal bath in which the couvette with the sample was immersed. The temperature inside the small thermal bath was monitored with a digital thermometer.

After the sample was prepared, a first measurement of the temperature of phase separation was performed. The heating of the couvette form the room temperature to the values expected for phase separation was performed in different arbitrary steps. For each step I set the desired value on the thermal bath, I wait that the temperature in the small thermal bath reach the equilibrium value and then wait for some minutes, usually 15 or 30 minutes. During this procedure the CCD camera acquires some NFS images: when the phase separation occurs the speckle field changes its properties, so I understand which is the temperature of phase separation. Then the sample is brought back to room temperature and mixed to have again an homogeneous sample. When the sample is at the initial condition the heating procedure is repeated to reach a final temperature a little bit lower than the phase separation temperature. At this final temperature the sample exhibit Casimir interactions and perform colloidal aggregation. During the heating and the aggregation processes I acquire NFS images with the CCD. This camera was controlled via LabVIEW software that allows to acquire a certain number of images when desired. I usually acquire 100 images at 1 fps every hour or every couple of hours. The images are then analyzed in the same typical way of near field scattering images, as described in previous chapter.

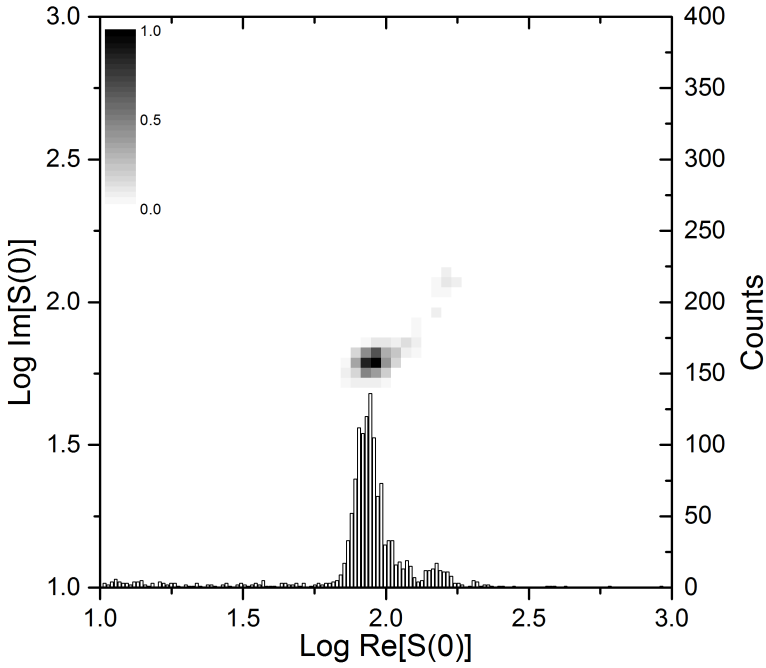

(a) SPES data for sphere.

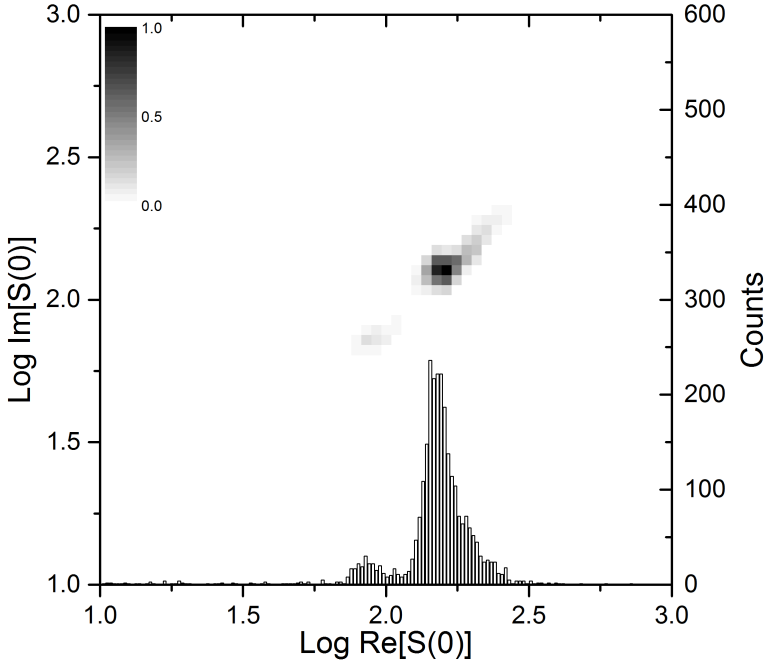

(b) SPES data for dumbbells.

Figure 5.3: Results of the measurements performed with SPES technique. The histograms are the projection of the 2D data on the x-axis.

5.4.2 Results

The first measurement was performed on the spherical particles. With these particles I do not study the aggregation process but just the form factor of the monomers to characterize their size. The result of this measurement is shown in fig. 5.4. The data

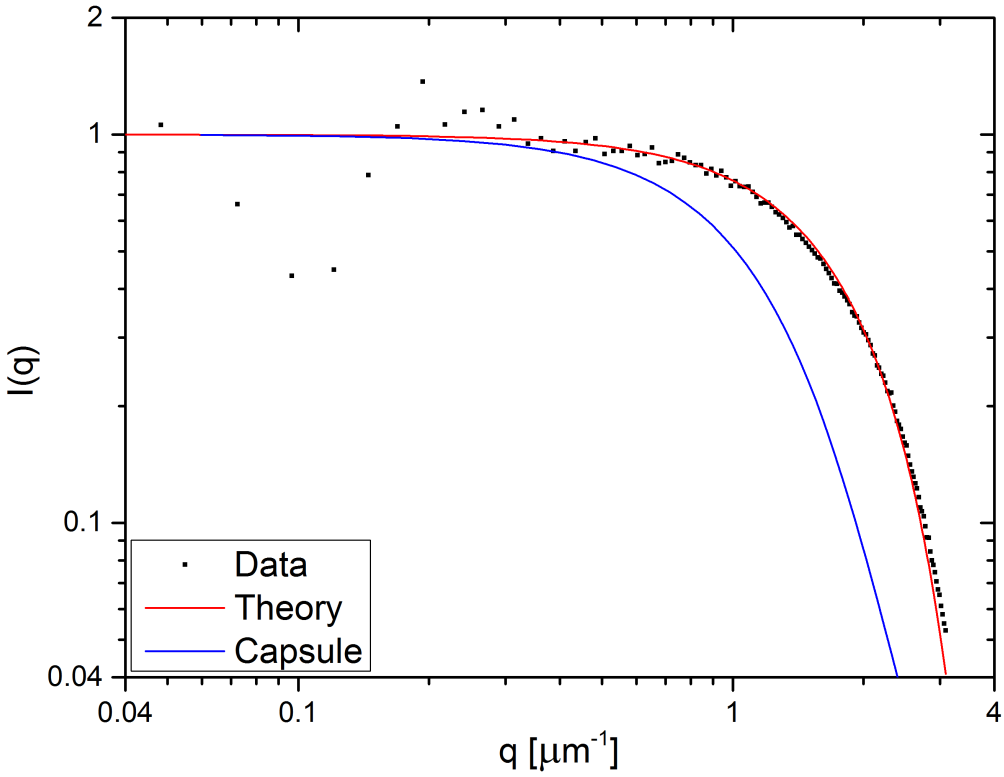

Figure 5.4: Form factor, or power spectrum, of the spherical particles that are used to build the dumbbells. The data are the black dot, while the red curve correspond to the curve for spherical particles of $2.2\mu m$ in diameter. The blue line instead represent the simulated curve for capsular particles.

are in good agreement with the theoretical curve calculated for spherical particle of 2.2 μm in diameter. The small differences at high q values are maybe due to polydispersity, which in the theoretical curve is not considered. At the same time it may also be caused by the presence of some dumbbells inside the sample, as observed with the SPES measurement (see fig. 5.3a). However the experimental curve is very different from the capsular-shape curve; it means that the presence of a little part of the other species doesn't affect the measurement and the shape of spheres (or dumbbells, depending on the studied sample) can be distinguished well.

After this measurement I start to study the anisotropic particles. As already mentioned before, this sample is composed by dumbbells on the left side of critical point. At first I characterize the dumbbells, so I study just the monomers without aggregation. In figure 5.5 there is a result of the measurement, represented by black points. To compare it with some known shape, I generate with the program ADDA the form factor of two

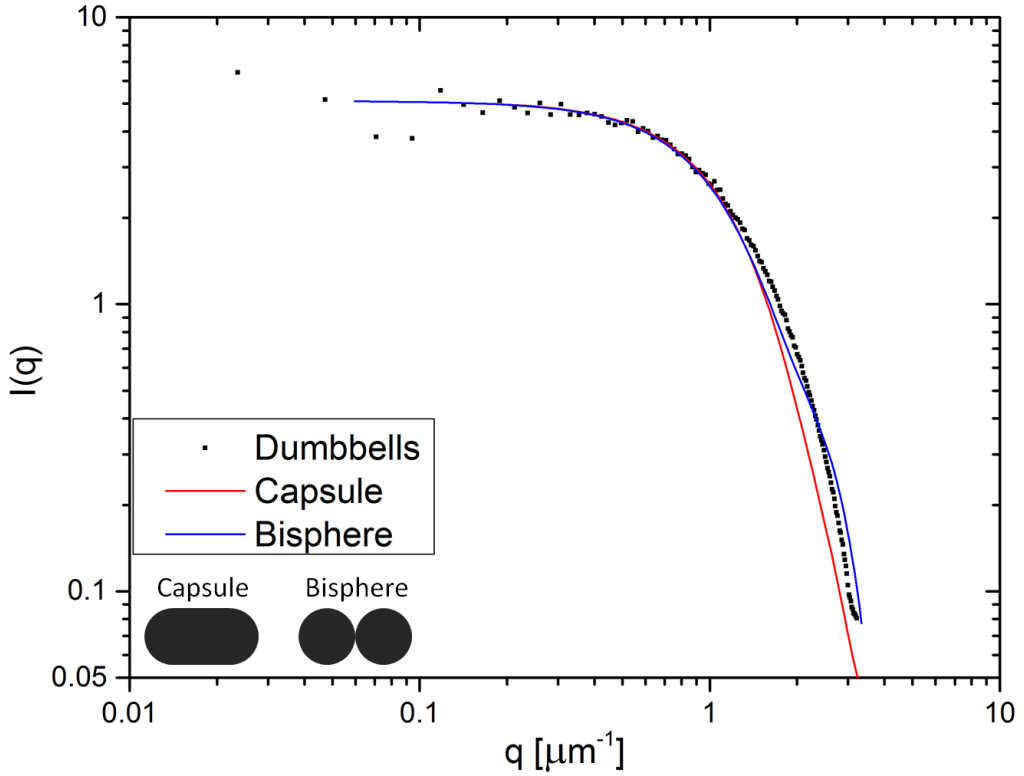

Figure 5.5: Power spectrum of the dumbbell particles. The data are the black dot. The red and the blue curve correspond to simulated curves for shape of capsule and bisphere. A simple sketch of the simulated particles is shown.

different kinds of particles. A capsular shape particle and a bisphere particles; a trivial picture of those particles is reported as inset in fig. 5.5. Both those particles are built starting from the dimension of the spheres measured before. Because of their anisotropic feature, their power spectra are calculated as an average of different particles (usually 500 particles) that are random oriented. The power spectrum of the capsule is the red line, while the blue line is for bisphere. Both these curves are not so far from the data. They represent correctly the behavior until $q \sim 1$, but they differ a little bit more at higher q. However this difference can be due to the fact that the simulated particles does not represent the real shape of the dumbbells; at the same time in simulation the polydispersity is not considered, instead it probably affects the measurements. As already shown in fig. 5.3b the sample has a distribution in size, and also a little component of spherical particles that may slightly affect the shape of the spectrum.

Once that the characterization of the dumbbells is performed, I start to study the aggregation process. In figure 5.6 is represented a result of an aggregation process. It is a

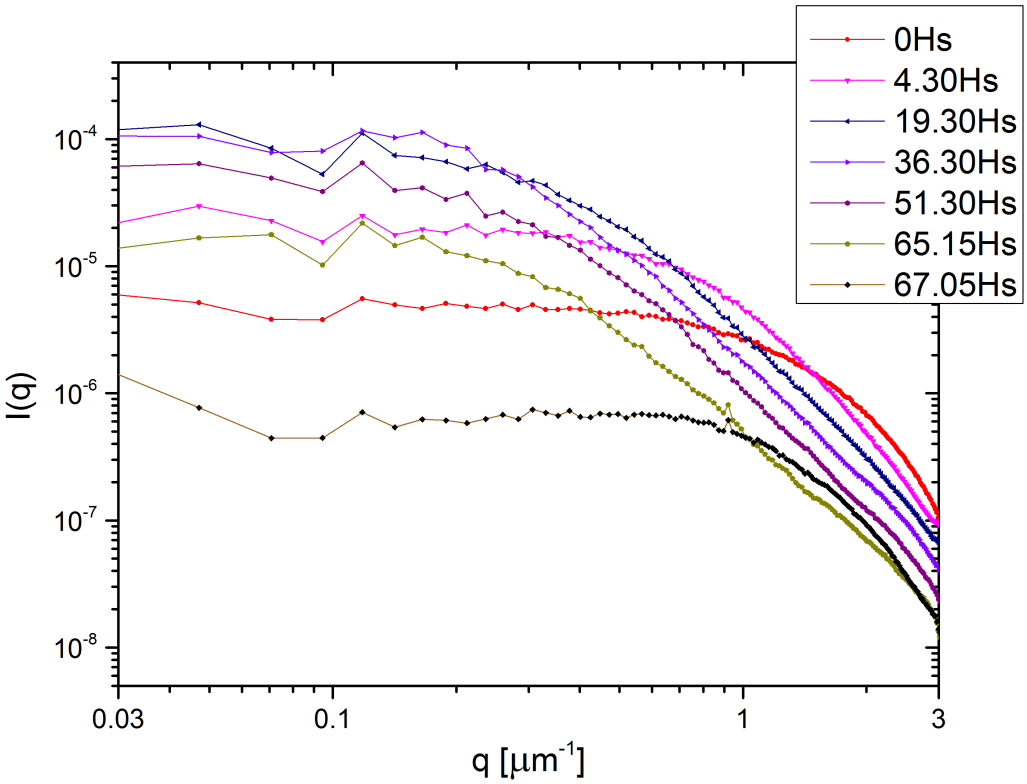

Figure 5.6: Power spectra related to the aggregation process. The different colors code the time passing as indicated in the legend.

similar results to the ones obtained in the COLLOID experiment. The different spectra increase in intensity and the position of the change in slope is at lower q-values. In addition to the growth of aggregates there is also a sedimentation effect. In fact the curves of aggregated samples should superpose for high q values; however even if they have a very similar shape in this region they are translated downward. This is a typical effect of

sedimentation, where the particles suspended decrease in number and so also the scattered intensity decrease. As final test of sedimentation effect, I exploit the reversibility of critical Casimir aggregation. If the sample is cooled down from temperature of aggregation to a temperature of some degrees lower, the critical fluctuations vanish and the particles no more attract each other. The aggregates dissolve and the starting condition is found. Comparing the first curve (red one) with the last one (black one) the shape is the same, but the black is translated downward. This show that the concentration of the sample is decreasing of a factor ten during the measurement. Because the aggregation process is very slow, it is reasonable to think that the first power spectrum that change appreciably (pink data) represent the samples with dimer. It means that the aggregates are jut composed by two monomers, i.e. two dumbbells. To verify this hypothesis I simulate the power spectrum of two dumbbells-aggregates in the two limiting condition: the first is the linear disposition of the two particles, simulating the aggregate as a cylinder. The second is the condition of one particle next to the other, simulated as a box with squared base. Also in this situation because of asymmetry in particles shape, an average on 500 different oriented particles is computed. The comparison between the data and the simulated curves and a simple sketch of the two simulations condition is represented in fig. 5.7. The aggregated particles seem very similar to the square power spectrum, indicating a very compact structure. The shape is not perfectly described because the simulated particles don't represent the eventual real shape of the aggregates, and at the same time they are monodispersed, while the sample is polydispersed, both in size and shape. Even if is reasonable to think that at this time of aggregation the aggregates are composed by a couple of dumbbells, not all the dumbbells may be aggregated and also there can be some aggregates composed by more than two particles.

5.5 Conclusions

With different techniques I perform the characterization of anisotropic particles that should be used for an experiment aboard the International Space Station. The anisotropic particles are dumbbells particles realized with two spherical particles of PMMA joined with a polymeric matherial. I study both the spherical and the dumbbells particles with different techniques: turbidimetry, SPES and NFS. The turbidimetry is just a measurement of the concentration, useful for the next measurements. SPES measures the particles population in the samples and shows that the separation of the different species in the samples, i.e. spheres and dumbbells, is good but not perfect. The last is NFS measurements; in particular I focus my attention on dumbbells particles. A good characterization of the not aggregated sample is performed, also with the help of the scattering simulation code ADDA, necessary for anisotropic particles. Also measurements of the aggregating sample on the right side of the critical point where there are strongest interactions were performed. Because of the long characteristic time in aggregation process I focus on the study of early stages of aggregations when the aggregates are composed by just two dumbbells. By a comparison of this kind of aggregates with ADDA simulations, I notice that the aggregates exhibit a compact structure.

Unfortunately I had different troubles on performing aggregation processes so a detailed study of the samples was not possible. To have a reasonable concentration for a scattering measurements I had to dilute the samples. The dilution of the samples decreases the concentration increasing the time of aggregation. In fact to reach the early stages of aggregation a lot of time occurs (several hours). The measures shown are performed only on the left side of the critical point, where the critical Casimir strength is stronger. Working on the right side with weaker interactions the timescale would in-

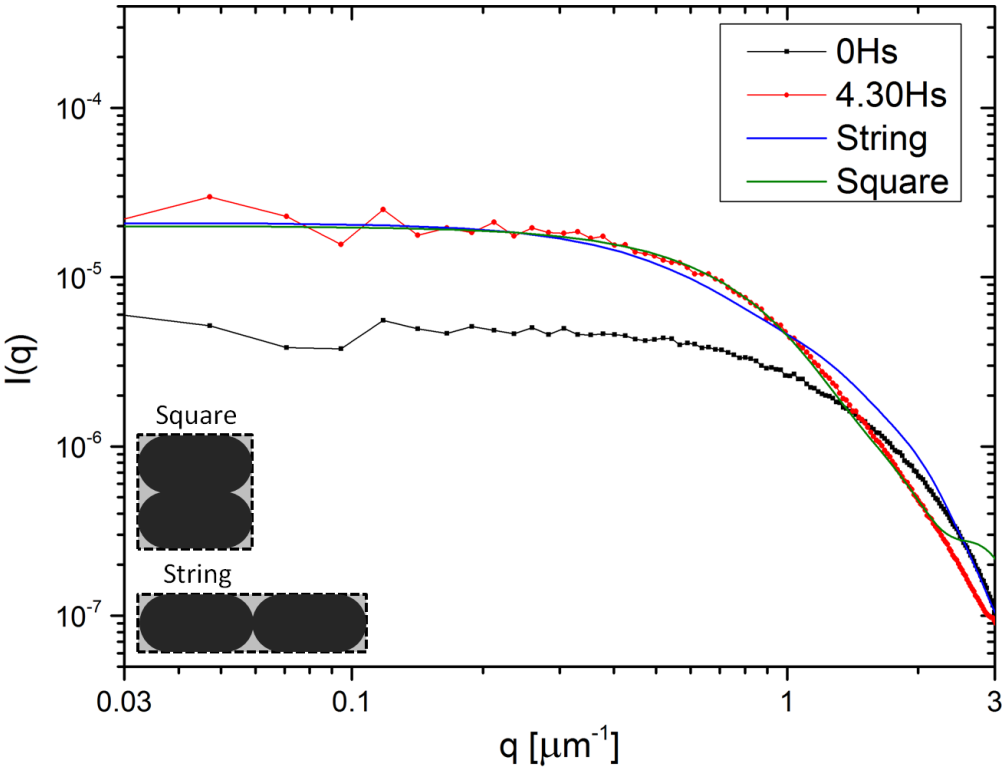

Figure 5.7: Power spectra of the early stages of aggregation. The black line+dot represents the dumbbells not aggregated, while the red one the aggregation of a couple of dumbbells. The blue and the green curves are the simulated power spectra of the two limiting disposition of dumbbells, as sketched in the inset. The gray shapes with the dashed line represent the simulated particles.

creases. Long timescale may also becomes a problem in this kind of samples because the particles are not density matched and so they settle down, decreasing once more the concentration of suspended particles.

At the same time I had troubles also on the heating setup. A more accurate thermal control was developed and realized. It was composed by an aluminum block that was heated by a peltier on one side. This block was then thermally insulated, bringing to a more accurate temperature monitoring and controlling. However the sample was not perfectly homogeneously heated causing a strange behavior that again not allow to Casimir effect to occur.

Once those issues are solved, especially the one relative to the timescales, some different measurements can be performed. At first a more accurate and systematic study of what happen changing the temperature, i.e. the critical Casimir strength. In my measurements I always try to be in condition of strongest interaction. However changing the temperature may give informations on the temperature of aggregation, i.e. the lowest temperature at which aggregation occurs. At the same time different interaction strength may give rise to different structures for the aggregates. Also interesting would be the study of the different behaviors between the sample on the left side and on the right side of critical point. The different surface properties of the particles brings to different behavior on the different side of the phase diagram and the aggregates that are formed may have different structures.

Because of the anisotropy of particles it may also be interesting to study those samples not only with standard near field scattering but also with depolarized NFS. It will be very interesting especially if the aggregates that form are similar to string, so they present a strong anisotropy. It could be a useful tool to understand the anisotropic features in the structure of the aggregates.

Also the study of particles more complex than the dumbbells may be very interesting. In fact, in addition to spheres and dumbbells, also other particles were synthesized by the UVA group. In particular they already realized some snowmen particles, two spheres with different dimensions joined together, or trimers and tetramers that are particles composed respectively by three or four spheres joined together by polymeric material. The study of all those different kinds of particles may give a better insight on how the particles interact and especially on how the structure formed with colloidal particles can be controlled and conditioned.

Conclusions

I studied colloidal aggregations with the near field scattering technique. The possibility to perform both static and dynamic measurements allows to obtain information on the internal structure of the aggregates. Other techniques as turbidimetry and single particles extinction and scattering (SPES) are used to achieve independent information on the samples.

The data analysis of the COLLOID experiment is extensively described. The aggregation was induced via critical Casimir interaction forces; a binary mixture close to phase separation brings colloidal particles to stick. The possibility of studying different samples at different temperatures allows a systematic study of this effect and on the aggregates that are formed. As widely studied in literature, universality in fractal aggregation is found. The possibility of building master curves both for static and dynamic data is an evidence of this universality, and at the same time gives a better consistency to data. The microgravity conditions combined to the critical Casimir effect bring to the formation of aggregates with fractal dimensions spanning a range of values from 1.8 to 2.5 in diffusion limited aggregation (DLA) conditions. The DLA condition is also confirmed by the growth of the gyration radii as function of time. A master curve for the form factors of the aggregates is built for each sample. Also for dynamic data a master curve describing the aggregation process is found. The possibility of studying a wide range of fractal dimensions allows to have a deeper insight in the structure of fractal aggregates. Studying the values of $\beta = R_H/R_g$ as a function of the fractal dimensions, we found that the aggregates exhibit a more compact structures than usually assumed. In fact the usual assumption is that the cutoff function in the density correlation function is represented by an exponential decaying function. The COLLOID results show that the correlation function best fitting the data is something between a gaussian and a unit-step cutoff function.

To have a ground comparison for the COLLOID experiment we also performed measurements on salt induced aggregating samples in DLA regime. Thanks to the recently developed SPES technique we are able to measure single aggregates obtaining the size distribution of the aggregating samples. The measured size distribution differs from the theoretical one, the best being provided by a lognormal function. However, to be model independent, in the analysis we use just the data without any fitting function. Also the fractal dimension for each aggregate is measured to be 2.2. The data collected with SPES technique are compared to the form factors obtained with NFS measurements on the same samples. To compute the form factor from the size distribution the only assumption is the Fisher-Burford expression for the form factor of single aggregates with the measured fractal dimension of 2.2. The combination of the form factor for each particle weighted with the measured size distribution leads to a form factor that is in good agreement with the one obtained with monodispersed form factor calculated with NFS

parameter (fractal dimension 1.7). The effect of polydispersity in the form factor is then to decrease the fractal dimension to an lower apparent value.

I also performed the characterization of samples that will be used for a new experiment in space aboard the International Space Station. The samples were composed by anisotropic particles dispersed in a binary mixture to perform aggregation with critical Casimir forces. The particles are dumbbells realized by joining two PMMA spheres with a polymeric material. I first studied the concentration of the samples with a turbidimetry measurement. With SPES technique I measured the populations of the sample finding that a small amount of spherical particles in the dumbbells sample is present. Finally with NFS technique I studied the dumbbells and their aggregation processes. At first I characterized the dumbbells comparing their form factors with numerical simulations. Then I studied the aggregation processes on the left side of the critical point, where Casimir attraction is stronger. Because of long timescales in aggregation I focused on the early stages of the aggregation when the aggregates are composed by only two dumbbells. Again comparing the size of aggregates with simulated form factors, I found that the aggregates exhibit a very compact structure, maybe caused by high interaction strength.

Appendix A

Calibration

Before performing measurements with the NFS setup it is very important to know the details of the system. The interest in the power spectrum and on the static form factor needs an accurate definition of the scattering angle of the radiation collected and studied. The calibration procedure is devoted to a good measurement of the magnification of the microscope objective that collects the light and of the spectral response of the camera. In this section I want to describe the procedure for calibrating a typical NFS apparatus.

A.1 Magnification

After the laser beam is spatially filtered and collimated it goes on the sample. The diffused light is collected by a microscope objective with nominal magnification 20x. This value is not so precise, also because it depends on the relative distance between the collecting sensor and the objective. The reciprocal positions used are very similar to the ideal one that is $160mm$. The magnification depends on the coupled plane and is not exactly 20x. A simple way to find the exact value of magnification is to use a speckle field and some properties of the correlation function.

A.1.1 Correlation function

The correlation function of a signal $s(x)$ of a certain variable x is defined as

$$G_s(\delta) = \frac{\langle s(x)s(x+\delta)\rangle_x}{\langle s^2(x)\rangle_x}. \tag{A.1.1}$$

The correlation function tells if there are some features that are repeated in the range of definition of the signal. This procedure for correlating the signal can be done also with two different signal $s(x)$, $t(x)$, and is usually called cross-correlation function. Its expression is

$$G_{s,t}(\delta) = \frac{\langle s(x)t(x+\delta)\rangle_x}{\langle s(x)\rangle_x \langle t(x)\rangle_x}. \tag{A.1.2}$$

An interesting thing to study is the cross-correlation function of a signal $s(x)$ and the same signal translated of a Δ factor, $s(x+\Delta)$. As showed in the figure A.1 the cross-correlation function will be around 0 everywhere except for the value of the translation Δ. A very similar thing happens when instead of cross-correlating the two signal, the

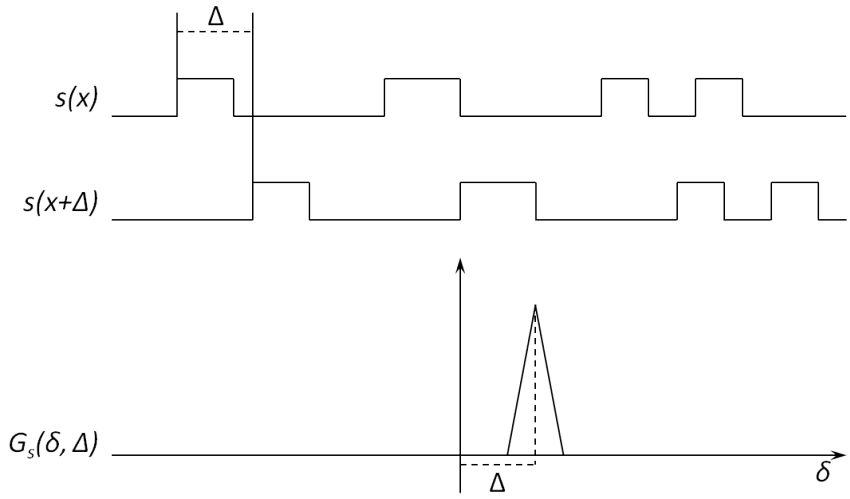

Figure A.1: Cross-correlation of a signal and the same signal translated of a quantity Δ.

auto-correlation of the two subtracted signal $d(x, \Delta) = s(x) - s(x + \Delta)$ is computed, i.e.

$$G_d(\delta, \Delta) = \frac{\langle d(x, \Delta) d(x + \delta, \Delta) \rangle_x}{\langle s^2(x, \Delta) \rangle_x} \tag{A.1.3}$$

This expression has a maximum for $\delta = 0$ and two symmetrical minima corresponding to the position $\pm\Delta$, as sketched in figure A.2.

Both these methods bring informations about the translation of the signal. But if this second method just gives the value of the translation Δ, the first one also shows in which direction the signal was moved.

A.1.2 Experimental procedure

After the microscope objective and the CCD are placed at the desired distance, that must remain the same for all measurements, a speckle field in homodyne condition is generated, for example with a frosted glass. After the acquisition of a first image the frosted glass is translated of a known quantity. A second image is acquired. The procedure described in the previous section can be applied to the different images. Obviously because the images are discrete, the value of Δ is in pixels. With the ratio between the real translation and the one in pixel, the effective dimension of the single pixel is found. By the ratio of the real size and the effective dimension of the pixel the real magnification of the microscope objective is measured. To have a reliable result this procedure can be repeated with different images all at the same distance, or also at different distances obtaining different correlation functions as in figure A.3.

In the previous section the signal was an ideal signal and the correlation function was performed on two signals that were exactly the same except for the translation. In the experimental condition it doesn't happen. The region of the frosted glass that diffuses light is limited to the region where there is the laser beam. When it is moved the region changes. However if the value of the translation is chosen accurately, small

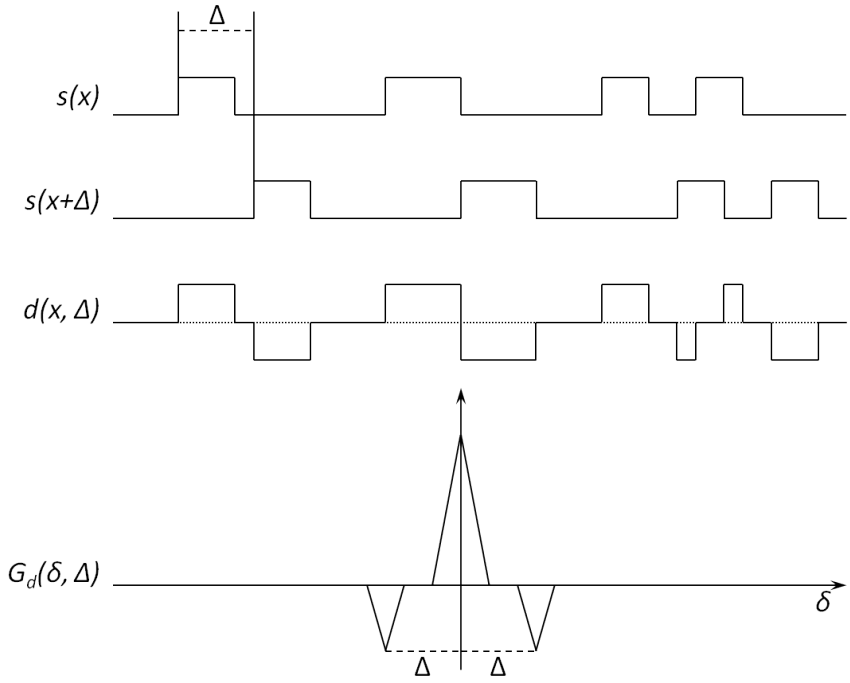

Figure A.2: Auto-correlation of the difference between a signal and the same signal translated of a quantity Δ.

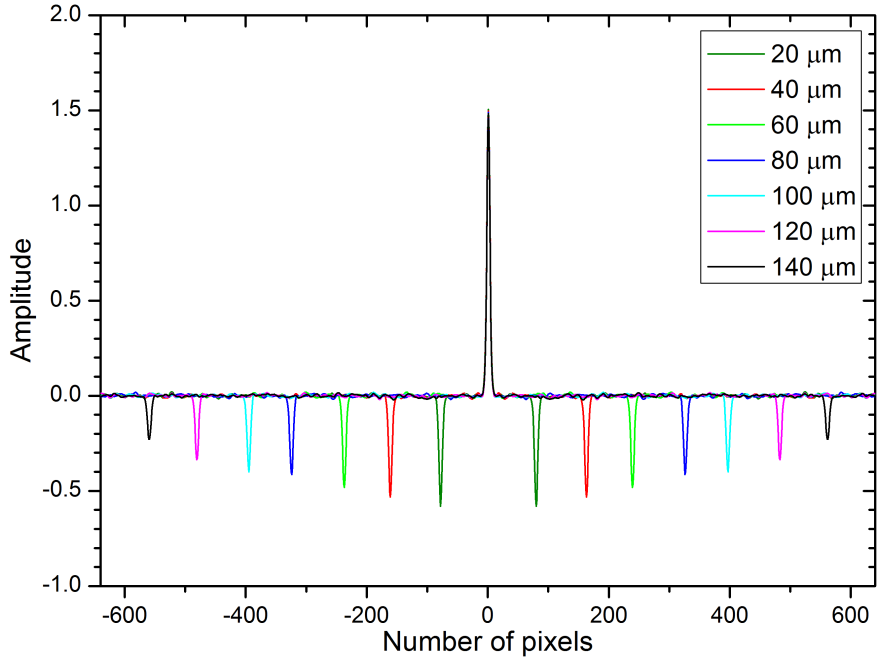

Figure A.3: Examples of the correlation function obtained for images at various distances. Each minimum corresponds to different distances as reported in plot legend.

compared the beam size, the speckle field doesn't change in an appreciable way and as a first approximation it can be considered exactly the same as before.

A.2 CCD spectral response

After the calibration of the magnification of the objective, the range of scattering vector can be calculated. Consider a square image of L pixels per side. The q=0 scattering vector correspond to the average of the image, a sinusoidal pattern of infinite wavelength. The smallest non zero q-vector is given by

$$q_{min} = \frac{2\pi}{Ld_{pix}} \tag{A.2.1}$$

where d_{pix} is the dimension of the effective pixel. All other scattering vectors can be calculated as $q_i = i \cdot q_{min}$, where i is an integer index counting the pixels of the Fourier-transformed image. The highest q-vectors that can be written on the image is given by the Nyquist-Shannon sampling theorem and is

$$q_{max} = \frac{\pi}{d_{pix}} \tag{A.2.2}$$

It represents a sinusoidal pattern corresponding to alternation of one pixel on, one off, and so on. However if a microscope objective is used it usually have an acceptance angle θ given by the numerical aperture. It can be related with a q-vector using the relation

$$q_{NA} = 2k\sin(\theta/2) \tag{A.2.3}$$

where k is the wavevector of the illuminating radiation. So the maximum spatial frequency is given by $min\{q_{max}, q_{NA}\}$.

When the range of the scattering vector is known, the calibration is dedicated to the spectral response of the CCD. Obviously the spectral response is not related to the wavelength also because the CCD is monochromatic and the laser is at a fixed wavelength. The spectral response is related to the different q-vectors and depends on how the CCD sensor is sensible to the different spatial frequencies.

A typical NFS measurement with a known sample si performed. It is important to know the sample because we need to know which is the power spectrum. In fact, the ratio of the measured and the theoretical power spectra represents the spectral response of the CCD. The sample usually used to do this measurement (with magnification of $\sim$ 20x) is a colloidal solution of polystyrene calibrated particles $1\mu m$ in diameter. The power spectrum of this kind of particles is analytically known by the Mie theory. The images are acquired to perform static light scattering, and once that the power spectrum is computed, also the ratio of the theoretical and measured spectra can be calculated. By this ratio the calibration function is found. For simplicity the calibration function is normalized to 1 and in the low-q region is manually kept constant. An example of this procedure is reported if figure A.4

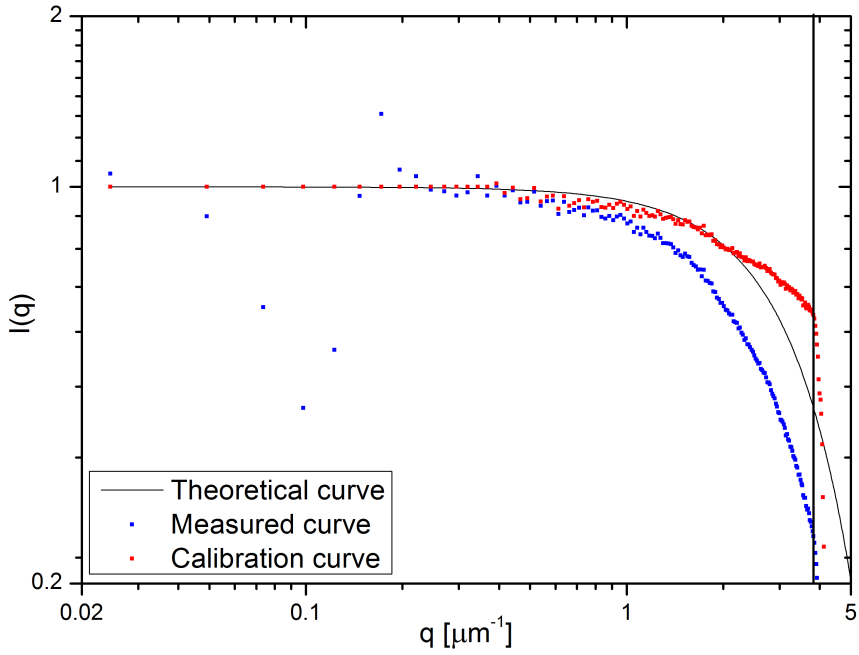

Figure A.4: Example of calibration function. The black line represent the calculated form factor with Mie theory for 1 μm sized particles. The blue dot represent the measured curve and the red ones the calibration function. The black vertical line stay for the maximum q-value.

Appendix B

Expressions for parameter β

The values of $\beta = R_H/R_g$ is directly related to the model used in the density correlation function. Usually in literature it is found as a constant value at the fixed fractal dimension. It is mainly due to the fact that in the two kind of aggregation process, DLA and RLA, the fractal dimension assumes standard values. However the dependence of β on the fractal dimension can be calculated. Here I show the calculation for three different kinds of cutoff functions for the correlation function [22].

The correlation function for fractal aggregates is defined as

$$C(r) = r^{d-3} f(r/R_0) \tag{B.0.1}$$

where $f(x)$ is the cutoff function that keeps account for the finite size R_0 of the aggregates. The gyration and hydrodynamic radii are defined in dependence of this function as

$$R_g^2 = \frac{1}{2} \frac{\int_0^\infty r^2 C(r) r^2 dr}{\int_0^\infty C(r) r^2 dr} \tag{B.0.2a}$$

$$R_H^{-1} = \frac{\int_0^\infty r^{-1} C(r) r^2 dr}{\int_0^\infty C(r) r^2 dr}. \tag{B.0.2b}$$

I will now show the calculation of the radii and of their ratio using three different cutoff functions: exponential (fluffier aggregates), Gaussian and unit-step (compact aggregates) function.

B.1 Exponential Cutoff

Consider an exponential decaying function defined as $f(r/R_0) = e^{-r/R_0}$; the correlation function is

$$C(r) = r^{d-3} e^{-r/R_0}. \tag{B.1.1}$$

To simplify the computational procedure I first find the expression of the integral

$$\int_0^\infty r^\alpha e^{-r/R_0} dr \tag{B.1.2}$$

where α is a generical exponent of the radius. This integral can be easily related to the $\Gamma(x)$ function.

Gamma Function

The gamma function $\Gamma(x)$ is a generalization of the factorial function and is defined both for real and complex numbers. In fact if n is a positive integer, $\Gamma(n+1) = n!$. The complete definition of the Gamma function is

$$\Gamma(z) = \int_0^\infty t^{z-1} e^{-t} dt.$$

Notice that the Gamma function is not defined for negative integers, where the function has simple poles. An integration by parts yields to the functional equation

$$\Gamma(z+1) = z\Gamma(z).$$

Combining it with $\Gamma(1) = 1$, it is easy to show that for a positive integer the function Gamma reduces to the factorial function with the argument subtracted by 1, $\Gamma(n) = (n-1)!$.

Getting back to the integral B.1.2, with the Gamma function and the substitution $r' = r/R_0$, it becomes:

$$\begin{aligned}\int_0^\infty r^\alpha e^{-r/R_0} dr &= R_0^{\alpha+1} \int_0^\infty r'^{(\alpha+1)-1} e^{-r'} dr' \\ &= R_0^{\alpha+1}\Gamma(\alpha+1) = R_0^{\alpha+1}\alpha\Gamma(\alpha). \end{aligned} \tag{B.1.3}$$

Using this simple expression I can now compute the normalization coefficient

$$N_0 = \int_0^\infty r^2 C(r) dr = \int_0^\infty r^{d-1} e^{-r/R_0} dr = R_0^d \Gamma(d) \tag{B.1.4}$$

and the gyration and hydrodynamic radii

$$\begin{aligned} R_g^2 &= \frac{1}{2N_0}\int_0^\infty r^4 C(r) dr = \frac{1}{2N_0}\int_0^\infty r^{d+1} e^{-r/R_0} dr = \\ &= \frac{1}{2N_0} R_0^{d+2}(d+1)\Gamma(d+1) \\ &\Rightarrow R_g = \sqrt{\frac{(d+1)d}{2}} R_0. \end{aligned} \tag{B.1.5}$$

$$\begin{aligned} R_H &= N_0 \left(\int_0^\infty r C(r) dr\right)^{-1} = N_0 \left(\int_0^\infty r^{d-2} e^{-r/R_0}\right)^{-1} = \\ &= N_0 \left(R_0^{d-1}\Gamma(d-1)\right)^{-1} \\ &\Rightarrow R_H = (d-1)R_0. \end{aligned} \tag{B.1.6}$$

The ratio between hydrodynamic and gyration radii becomes

$$\beta = \frac{R_H}{R_g} = \frac{\sqrt{2}(d-1)}{\sqrt{d(d+1)}}. \tag{B.1.7}$$

It is interesting to notice that it depends only on the fractal dimension.

B.2 Gaussian Cutoff

Consider a Gaussian cutoff function $f(r/R_0) = e^{-r^2/R_0^2}$. The correlation function is now given by

$$C(r) = r^{d-3}e^{-r^2/R_0^2}. \tag{B.2.1}$$

Again to simplify the computational procedure I first compute the integral of a generic power and then apply it for the normalization factor, the gyration and the hydrodynamic radii. Again this kind of integral can be related to the Gamma function with the substitution $t = r^2/R_0^2$

$$\int_0^\infty r^\alpha e^{-r^2/R_0^2}dr = \frac{R_0^{\alpha+1}}{2}\int_0^\infty t^{\frac{\alpha+1}{2}-1}e^{-t}dt = \frac{R_0^{\alpha+1}}{2}\Gamma\left(\frac{\alpha+1}{2}\right). \tag{B.2.2}$$

Using this expression, the normalization coefficient can be computed:

$$N_0 = \int_0^\infty r^2 C(r)dr = \int_0^\infty r^{d-1}e^{-r^2/R_0^2}dr = \frac{R_0^d}{2}\Gamma\left(\frac{d}{2}\right) \tag{B.2.3}$$

and the gyration and hydrodynamic radii

$$\begin{aligned} R_g^2 &= \frac{1}{2N_0}\int_0^\infty r^4 C(r)dr = \frac{1}{2N_0}\int_0^\infty r^{d+1}e^{-r^2/R_0^2}dr = \\ &= \frac{1}{2N_0}R_0^{d+2}\Gamma(d+1) \\ &\Rightarrow R_g = \frac{\sqrt{d}}{2}R_0. \end{aligned} \tag{B.2.4}$$

$$\begin{aligned} R_H &= N_0\left(\int_0^\infty rC(r)dr\right)^{-1} = N_0\left(\int_0^\infty r^{d-2}e^{-r^2/R_0^2}\right)^{-1} = \\ &= N_0\left(R_0^{d-1}\Gamma\left(\frac{d-1}{2}\right)\right)^{-1} \\ &\Rightarrow R_H = \frac{\Gamma(d/2)}{\Gamma(d/2-1/2)}R_0. \end{aligned} \tag{B.2.5}$$

The value of beta is now given by

$$\beta = \frac{R_H}{R_g} = \frac{\Gamma(d/2)}{\Gamma(d/2-1/2)}\frac{2}{\sqrt{d}}. \tag{B.2.6}$$

Notice again that the only dependence of β is on the fractal dimension.

B.3 Unit-Step Cutoff

Consider now as cutoff function $f(r/R_0) = \Theta(1-r/R_0)$, where $\Theta(x)$ is the Heaviside function, that is 0 if $x < 0$ and 1 if $x > 0$. The correlation function becomes

$$C(r) = r^{d-3}\Theta(1-r/R_0). \tag{B.3.1}$$

Computing the integral of the generic power α of the radius I find

$$\int_0^\infty r^\alpha C(r)dr = \int_0^\infty r^{\alpha+d-3}\Theta(1-r/R_0)dr = \\ = \left[\frac{r^{\alpha+d-2}}{\alpha+d-2}\right]_0^{R_0} = \frac{R_0^{\alpha+d-2}}{\alpha+d-2}. \tag{B.3.2}$$

By means of this expression, the normalization term is given by

$$N_0 = \int_0^\infty r^2 C(r)dr = \frac{R_0^d}{d}. \tag{B.3.3}$$

and the gyration and hydrodynamic radii are given by

$$R_g^2 = \frac{1}{2N_0}\int_0^\infty r^4 C(r)dr = \frac{d}{2R_0^d}\frac{R_0^{d+2}}{d+2} \\ \Rightarrow R_g = \sqrt{\frac{d}{2(d+2)}}R_0. \tag{B.3.4}$$

$$R_H = N_0\left(\int_0^\infty rC(r)dr\right)^{-1} = \frac{R_0^d}{d}\frac{d-1}{R_0^{d-1}} \\ \Rightarrow R_H = \frac{d-1}{d}R_0. \tag{B.3.5}$$

By their ratio we find the expression for β as

$$\beta = \frac{R_H}{R_g} = \frac{d-1}{d}\sqrt{\frac{2(d+2)}{d}}. \tag{B.3.6}$$

Also with this last cutoff function the expression of β depends only on the fractal dimension.

In figure B.1 is represented the dependence of β as a function of d for the three different cutoff expressions considered for the correlation function.

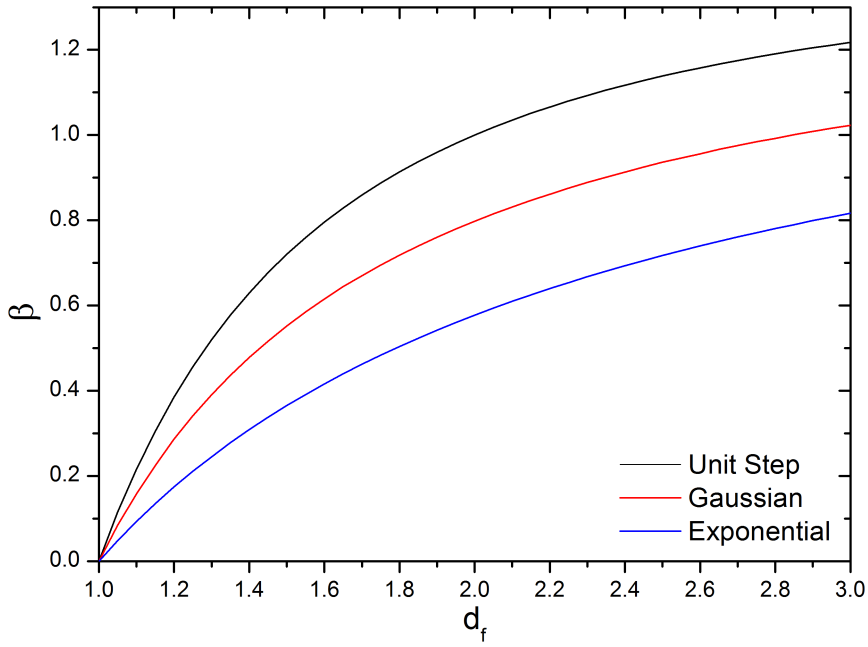

Figure B.1: Plot of the different expressions of β as a function of d with the three different cutoff functions.

Bibliography

[1] D. Beysens and D. Extève. Adsorption phenomena at hte surface of silica spheres in a binary liquid mixtures. *Phys. Rev. Lett.* , 54(19), 1985.

[2] N. L. Broide, Y. Garrabos, and D. Beysens. Nonfractal colloidal aggregation. *Phys. Rev. E* , 47(5), 1993.

[3] D. Beysens and T. Narayanan. Wetting-induced aggregation of colloids. *J. Stat. Phys.*, 95(5), 1999.

[4] H. B. G. Casimir. On the attraction between two perfectly conducting plates. *Proc. Koninklijke Nederlandse Akad. Wetenschappen*, B51:793–795, 1948.

[5] S. K. Lamoreaux. Demonstration of the Casimir Force in the 0.6 to 6 μm range. *Phys. Rev. Lett.* , 78(1):5–8, 1997.

[6] M. E. Fisher and P. G. de Gennes. Phenomena at the walls in a critical binary mixture. *C. R. Acad. Sci. Paris*, B(287):207–209, 1978.

[7] C. Hertlein et al. Direct Measurement of critical Casimir forces. *Nature* , 451:172–175, 2008.

[8] A. Hanke et al. Critical Casimir forces between spherical particles in fluids. *Phys. Rev. Lett.* , 81(9):1885–1888, 1998.

[9] D. Bonn et al. Direct Observation of colloidal aggregation by critical Casimir forces. *Phys. Rev. Lett.* , 81(9):1885–1888, 1998.

[10] U. Nellen, L. Helden, and C. Bechinger. Tunability of critical Casimir interactions by boundary conditions. *Europhys. Lett.* , 88(2):26001, 2009.

[11] R. J. Hunter. *Fundation of Colloid Science*. Oxford University Press, New York, 1987.

[12] H. C. Van de Hulst. *Light Scattering by Small Particles*. Dover, 1981.

[13] J. W. Goodman. *Introduction to Fourier Optics*. McGraw-Hill, 1996.

[14] B. J. Berne and R. Pecora. *Dynamic Light Scattering: With Applications to Chemistry, Biology, and Physics*. Plenum Press, 1976.

[15] F. Ferri et al. Heterodyne near-field scattering: a technique for complex fluids. *Phys. Rev. Lett.* , 70(041405), 2004.

[16] D. Magatti et al. Dynamic heterodyne near-field scattering. *Appl. Phys. Lett.* , 92 (241101), 2008.

[17] S. Mazzoni et al. SODI-COLLOID: A combination of static and dynamic light scattering on board the International Space Station. *Rev. Sci. Instrum.*, 92(241101), 2013.

[18] M. A. C. Potenza et al. Dynamics of colloidal aggregation in microgravity by critical Casimir forces. *Europhys. Lett.* , 106(68005), 2014.

[19] B. M. Tande et al. Viscosimetric, hydrodynamic, and conformational properties of dendrimers and dendrons. *Macromolecules*, 34(8580), 2001.

[20] B. Hirzinger, M. Helmstedt, and J. Stejskal. Light scattering studies on core-shell systems: determination of size parameters of sterically stabilized poly(methylmethacrylate) dispersions. *Polymer*, 41(2883), 2000.

[21] P Wiltzius. Hydrodynamic behavior of fractal aggregates. *Phys. Rev. Lett.* , 58(7), 1987.

[22] C. M. Sorensen, J. Cai, and N. Lu. Test of static structure factors for describing light scattering from fractal soot aggregates. *Langmuir*, 8(2064), 1992.

[23] S. J. Veen et al. Colloidal aggregation in microgravity by critical Casimir forces. *Phys. Rev. Lett.* , 109(248302), 2012.

[24] H. M. Lindsay et al. The effect of rotational diffusion on quasielastic light scattering from fractal colloidal aggregates. *Phys. Rev. A* , 38(2614), 1988.

[25] H. M. Lindsay et al. Properties of fractal colloid aggregates. *Faraday Discuss. chem. Soc.*, 83(153), 1987.

[26] M. Y. Lin et al. Universality of fractal aggregates as probed by light scattering. *Proc. Royal Soc. London*, 423(1864), 1989.

[27] G. Pranami, M. H. Lamm, and R. D. Vigil. Molecular dynamics simulation of fractal aggregate dffusion. *Phys. Rev. E* , 82(051402), 2010.

[28] M. Carpineti et al. Salt-induced fast aggregation of polystirene latex. *Phys. Rev. A* , 42(12), 1990.

[29] M. A. C. Potenza, T. Sanvito, and A. Pullia. Accurate sizing of ceria oxide nanoparticles in slurries by the analysis of the optical forward-scattered field. *J. Nanopart. Res.*, 17(110), 2014.

[30] M. A. C. Potenza, T. Sanvito, and G. Fazio. Optical characterization of industrial slurries. *KONA particle and particle journal review, in press*, 2015.

[31] M. A. C. Potenza et al. How to measure the optical thickness of scattering particles from the phase delay of scattered waves: application to turbid samples. *Phys. Rev. Lett.* , 105(193901), 2010.

[32] M. A. C. Potenza and P. Milani. Free nanoparticle characterization by optical scattering field analysis: opportunities and perspectives. *J. Nanopart. Res.*, 16(2680), 2014.

[33] C. F. Bohren and D. R. Huffman. *Absorption and Scattering of Light by Small Particles*. John Wiley & Sons, 1983.

[34] D. A. Weitz and M. Y. Lin. Dynamic scaling of cluster-mass distribution in kinetic colloid aggregation. *Phys. Rev. Lett.* , 57(16), 1986.

[35] M. Y. Lin et al. Universal diffusion-limited colloid aggregation. *J. Phys.: Condens. Matter*, 2(3093), 1990.

[36] G. M. Wang and C. M. Sorensen. Diffusive mobility of fractal aggregates over the entire knudsen number range. *Phys. Rev. E* , 60(3036), 1999.

[37] U. Kaetzel et al. Dynamic Light Scattering for the Characterization of Polydisperse Fractal Systems: II. Relation between Structure and DLS Results. *Part. Part. Syst. Charact.*, 25(19), 2008.

[38] M. Y. Lin et al. Universal reaction-limited colloid aggregation. *Phys. Rev. A* , 41 (2005), 1990.

[39] J. C. Dainty. *Laser Speckles and Related Phenomena*. Springer-Verlag, 1984.

[40] M. D. Alaimo et al. Heterodyne speckle velocimetry. *Appl. Phys. Lett.* , 88(191101), 2006.